2025-08-20

Acoustic Characterization and Modeling of Heated Supersonic Tactical Jet Aircraft and Launched Rockets

Logan Troy Mathews
Brigham Young University

Acoustic Characterization and Modeling of Heated Supersonic Tactical Jet Aircraft and Launched Rockets

Logan Troy Mathews

A dissertation submitted to the faculty of
Brigham Young University
in partial fulfillment of the requirements for the degree of

Doctor of Philosophy

Kent L. Gee, Chair
Micah R. Shepherd
Tracianne B. Neilsen
Brian E. Anderson
Steven E. Gorrell

Department of Physics and Astronomy

Brigham Young University

ABSTRACT

Acoustic Characterization and Modeling of Heated Supersonic Tactical Jet Aircraft and Launched Rockets

Logan Troy Mathews
Department of Physics and Astronomy, BYU
Doctor of Philosophy

Understanding and accurately modeling the acoustic sources and propagation of high-intensity tactical jet aircraft and rocket noise is essential for vehicle design, environmental impact assessment, and mitigation strategies. Despite progress in the understanding of these sources, significant challenges persist in both predictive modeling and noise mitigation. This dissertation advances both the characterization of full-scale supersonic tactical jet aircraft noise sources and the development of modern empirical prediction models for rocket launch noise. Across multiple measurement campaigns and modeling efforts, the work integrates advanced array signal processing, high-fidelity field measurements, and improved empirical methods to expand the physical understanding of source mechanisms and deliver accurate, practical prediction tools.

The first portion of this work focuses on acoustic source characterization for a full-scale, installed GE F404 engine operating at afterburner. Using coherence-based partial field decomposition methods, implemented via an equivalent source reconstruction with acoustical holography, apparent source distributions are resolved across frequency. A bandwidth extension technique employing array phase-unwrapping and interpolation enables detailed mapping of local maxima, distinct in frequency and space, along the nozzle lipline. Analysis reveals distinct subsources—ranging from possible large-scale turbulence in the convectively subsonic region to likely Mach wave radiation originating throughout the shear layer—along with regions of mixed source contributions producing spatiospectral lobes.

Subsequent analysis addresses broadband shock-associated noise (BSN), a dominant high-frequency component in imperfectly expanded supersonic jets. Full-scale measurements from the installed F404 engine on the T-7A trainer aircraft identify BSN sources along the nozzle lipline, corroborated by in-situ imaging. Measured shock spacing deviates from current analytical predictions, impacting the performance of established BSN frequency models; however, accuracy is restored when models are corrected using measured shock cell spacing. Coherence analysis demonstrates coupling between upstream-directed BSN and downstream Mach wave radiation, as well as elevated coherence between shock cells, indicating a partially coherent, spatially distributed BSN source.

Building on these source characterization efforts, a field measurement campaign measured the acoustic environment surrounding the Atlas V JPSS-2 launch from Vandenberg Space Force Base. Eleven measurement stations, ranging from 200 m to 7.7 km at multiple azimuthal angles, captured several details of the launch acoustics. These include both a 30 dB variation in ignition overpressure peak levels due to flame trench directionality and potential azimuthal asymmetry in the radiated noise field. These data form the foundation for subsequent empirical model development.

A new set of simplified predictive relationships is presented for estimating overall acoustic power levels and maximum overall sound pressure levels from heated supersonic aircraft jet

engines and rockets. Based on fundamental flow properties, these models demonstrate strong predictive performance for Atlas V and Vulcan Centaur launches, as well as for the installed GE F404 engine across several operating conditions, achieving root mean square errors of less than 2 dB for maximum unweighted sound levels.

The final contribution is SATURN (Scientific Acoustic Tool for Understanding Rocket Noise), a modular, open research model that modernizes the legacy NASA SP-8072 framework. SATURN incorporates high-fidelity acoustic parameters derived from the Atlas V 401 dataset and an empirically derived propagation loss model for spectral levels. Validation against Firefly Alpha and SpaceX Starship launches yields 34 independent validation points over a broad range of distances. SATURN predicts the unweighted levels near peak radiation with a root-mean-square error of ~1 dB within 20 km, representing a factor of two or more improvement in acoustic pressure accuracy over SP-8072.

Collectively, this work provides new physical insights into the source mechanisms of full-scale supersonic jets, delivers improved empirical tools for rocket noise prediction, and establishes a validated, modular modeling framework for future launch noise prediction applications. The combination of high-fidelity measurements, advanced source decomposition, and modernized prediction models offers a pathway toward more accurate and flexible acoustic assessment capabilities for aerospace applications.

Keywords: rocket noise, jet noise, broadband shock-associated noise, acoustical holography, coherence, signal processing, acoustics

ACKNOWLEDGMENTS

A PhD is just one example of a life accomplishment that—while formally awarded to a single individual—reflects the collective contributions of many others who supported, instructed, and encouraged along the way. This accomplishment would not have been possible without them, and I am deeply grateful to all who have supported me over the last four years.

I owe particular thanks to my advisor, Kent Gee, whose guidance shaped every part of this journey. He provided world-class research opportunities, set high expectations, offered a helpfully critical eye, and brought a healthy dose of humor to our work—all while balancing the immense responsibilities of grant writing, student mentoring, teaching, family life, and department leadership. His mentorship has been instrumental in both my technical growth and professional development.

I am also grateful to Alan Wall and Reese Rasband for their exceptional mentorship and support during my ORISE fellowship. Thank you for your guidance and for the opportunity to learn from your experience.

To my labmates—thank you for letting me learn from each of you. Each of you contributed to my growth in ways I will always value. To Mark Anderson and Tyce Olaveson, my fellow PhD students during this time—thank you for sharing your incredible talents. Because of you, I am a slightly less mediocre theoretician and computationalist.

Outside the lab, I am especially grateful to my family and to friends who are family in all but name. Your encouragement and belief in me have meant more than I can say.

Finally, the greatest share of my gratitude goes to Bryn. Your support, patience, and love have been a force that has carried me through all the craziness that is graduate school. You have been everything a partner should be. I cannot begin to express all the ways you have made this possible.

TABLE OF CONTENTS

LIST OF FIGURES vii
LIST OF TABLES x
Chapter 1 Introduction 1
1.2 Jet and Rocket Noise Foundations 2
1.3 Jet Noise Theory 3
1.4 Noise Modeling 7
1.5 Objectives and Scope 7
Chapter 2 Acoustical Holography and Coherence-Based Noise Source Characterization of an Installed F404 Engine 10
Chapter 3 On Broadband Shock-Associated Noise Source and Radiation Characteristics from an Installed, Afterburning GE F404 Engine 25
Chapter 4 An overview of acoustical measurements made of the Atlas V JPSS-2 rocket launch 44
Chapter 5 Methods for predicting overall sound power and maximum overall sound pressure levels from heated supersonic jets, including rockets 57
Chapter 6 SATURN: A Modern Empirical Model for Predicting Rocket Launch Noise 68
Abstract 68
6.1 Introduction 69
6.2 Model Data Sources 71
6.3 Methodology 73
6.3.1 Layout and Geometry 73
6.3.2 Sound Power 74
6.3.3 Sound Pressure Levels 78
6.3.4 Metrics 88
6.4 Validation 89
6.4.1 Validation Datasets 89
6.4.2 Alpha Validation 90
6.4.3 Starship Validation 94
6.5 Conclusion 98
6.6 Chapter Acknowledgments 99
Chapter 7 Conclusions 101
7.1 Primary Contributions 101
7.1.1 Full-Scale Jet Noise Source Decomposition (Chapter 2) 101
7.1.2 Broadband Shock-Associated Noise Characterization (Chapter 3) 102
7.1.3 Rocket Launch Acoustics and Source Modeling (Chapter 4) 102
7.1.4 Predictive Models for Supersonic Jet and Rocket Noise (Chapter 5) 103
7.1.5 The SATURN Rocket Noise Prediction Model (Chapter 6) 103
7.2 Recommendations for Future Work 104

Appendix A Summary of Other Notable Contributions 106
A.1 Saturn V Acoustics 106
A.2 Convective Mach Number Study 107
A.3 Afterburning Lab-Scale Jet Rig Measurements 107
A.4 Starship-Super Heavy Acoustics 108
Appendix B SATURN Appendices 109
B.1 SATURN Model Archive 109
B.2 Computing $\boldsymbol{\theta}$ and r 109
B.3 Source Location Angular Errors 110
Bibliography 113

LIST OF FIGURES

Figure 1.1. Historical orbital launch trends globally and for the United States, to the present year. Data from McDowell (2025). 2

Figure 1.2. Schematic illustrating the anatomy of a supersonic jet and the various radiative noise sources. 4

Figure 1.3. Schematic of an overexpanded jet's potential core region showing the anatomy of the shock cells in the jet. 6

Figure 6.1. Map showing measurement locations and launch pad for the Atlas V JPSS-2 launch. 72

Figure 6.2. Normalized relative sound power spectrum model derived from Atlas V launches compared with SP-8072 model. 77

Figure 6.3. Schematic of a rocket plume showing the definition of the angle θ for a given frequency-dependent source location $\mathrm{s(Sr)}$. 78

Figure 6.4. Apparent axial source locations from different rocket measurements and models as a function of Strouhal number. 80

Figure 6.5. Frequency-dependent directivity indices derived from the Atlas V data inside of 1 km radially from the launch site. 82

Figure 6.6. Apparent decay as a function of distance from the Atlas V JPSS-2 measurement for the spectra during the period of maximum directivity, defined as the region 3 dB down from the maximum recorded level. 85

Figure 6.7. (a) Apparent sound pressure level spectral decay from measurements of the Atlas V JPSS-2 mission relative to the closest measurement station as a function of distance to the source and dimensional frequency. (b) Modeled sound pressure level spectral decay using the double-filter model based on Eq. (6.9). 88

Figure 6.8. Maximum sound pressure levels from Alpha Flight 5 across various distances from measurements compared with predictions from SP-8072 and SATURN for (a) unweighted levels and (c) A-weighted levels. Deviations between measured and modeled levels for (b) unweighted and (d) A-weighted levels; ±2 dB shaded region and logarithmic fits of deviations shown. 91

Figure 6.9. Site-specific validation showing unweighted levels as a function of observer time (left column), as well maximum spectra (right column) for Alpha Flight 5 from measurements compared with predictions from SP-8072 and SATURN across three representative distances. 93

Figure 6.10. Maximum sound pressure levels from Starship Flight 6 across various distances from measurements reported by Gee *et al.* (2025b) compared with predictions from SP-8072 and SATURN for (a) unweighted levels and (c) A-weighted levels. Deviations between measured and modeled levels for (b) unweighted and (d) A-weighted levels; ±2 dB shaded region and logarithmic fits of deviations shown. 95

Figure 6.11. Site-specific validation showing unweighted levels as a function of observer time (left column), as well maximum spectra (right column) for Starship Flight 6 from measurements compared with predictions from SP-8072 and SATURN across three representative distances..... 97

LIST OF TABLES

Table 6.1. Relevant information for the validation and model-construction rockets. 89

Chapter 1

Introduction

As technology has progressed, so too has humanity's capacity to generate noise. Among the loudest continuous anthropogenic sources are aircraft and rockets—icons of modern innovation that also produce some of its most intense sound fields. While the sharp crackle of a military jet flyover or the thunderous roar of a rocket launch may captivate onlookers, the same sounds can create impacts for launch structures, nearby communities, and environments. In an era where air and space travel are increasingly common, a deeper understanding of jet and rocket noise is critical for accurate modeling, prediction, impact assessment, mitigation, and reduction.

Military jet noise presents a substantial challenge for current and future operations of the United States Armed Forces. Community noise complaints and hearing-related injuries among service members remain major concerns for the Department of Defense (Wall *et al.*, 2021). Improved characterization of jet noise sources is essential for validating computational models and guiding the design of noise-reduction technologies and mitigation strategies.

Society's dependence on space access continues to grow—supporting climate monitoring, global communications, national defense, and space science. Rockets remain the primary gateway to orbit and beyond. As annual launch rates increase (see Fig. 1.1), so too do the acoustic impacts on communities and environments near launch sites. Meanwhile, new and more powerful rockets introduce greater vibroacoustic challenges for vehicles, infrastructure, and

payloads. Addressing these challenges requires robust models and physical insight into how rocket noise is generated, radiated, propagated through the atmosphere, and ultimately received by people, structures, and the environment.

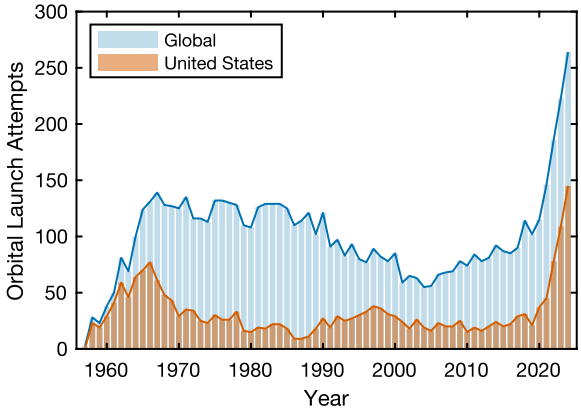

Figure 1.1. Historical orbital launch trends globally and for the United States, to the present year. Data from McDowell (2025).

1.2 Jet and Rocket Noise Foundations

Jets are most widely associated with aerospace propulsion. The introduction of jet-powered aircraft in the late 1940s marked the dawn of the "jet age," a technological leap that brought with it a powerful new source of noise. High-speed exhaust from turbine engines generated substantial aeroacoustic emissions, and as jet aircraft grew in number and size, so did concerns over their noise.

This motivated the foundational theoretical work of Sir Michael James Lighthill in the early 1950s (Lighthill, 1952; 1954). His pioneering aeroacoustic analogy reformulated the Navier–Stokes equations into a form analogous to the acoustic wave equation, reducing the complex turbulent flow of a jet to analytically tractable acoustic source terms. Lighthill's analogy remains

a cornerstone of jet noise theory—extended to supersonic jets and still widely used in analytical and numerical studies.

Simultaneously, experimentalists were characterizing the source and radiation properties of jet noise (e.g., Hubbard and Lassiter, 1953; Ribner, 1954; Howes, 1957; Franken, 1958; Nagamatsu *et al.*, 1969; Harper-Bourne and Fisher, 1974). These studies laid much of the groundwork for the field, enabling early noise reduction technologies and shaping subsequent theoretical developments. Important advances in theory followed, including the work of Ffowcs-Williams and Hawkings (1969), Lilley (1974), and Tam (1975), which helped solidify the physical understanding of jet noise generation and propagation.

In parallel, rocket noise emerged as a new area of focus. The onset of the space race in the late 1950s brought jet-based propulsion to a new regime: the rocket engine. While rudimentary rockets had existed for centuries, it was only with the push for orbital access that acoustically significant rocket engines came into widespread use at a scale that produced significant noise. Early experimental investigations (e.g., Cole *et al.*, 1957; Tedrick, 1964; Manhart *et al.*, 1966) sought to characterize rocket motors across various fuel types and scales. These efforts were followed by key predictive studies (e.g., Chobotov and Powell, 1957; Wilhold and Guest, 1963; Potter and Crocker, 1966), culminating in NASA SP-8072 (Eldred, 1971)—a comprehensive empirical model built from more than a decade of accumulated research, and still frequently cited in modern rocket noise analysis.

1.3 Jet Noise Theory

At its core, a jet is a stream of fluid ejected from a nozzle or orifice into a surrounding medium. Jets are ubiquitous in nature and technology—spanning applications from microfluidics

to showerheads to astrophysical jets from black holes. This dissertation focuses specifically on supersonic jets from propulsion systems, where exhaust exits the nozzle at speeds exceeding the speed of sound. As this high-velocity jet interacts with the quiescent ambient air, velocity shear develops at the interface, generating oscillations and turbulence along the flow boundary. By way of nomenclature, this dissertation generally uses the term *jet* in its elementary fluid dynamic definition; differentiation is made between *jet aircraft* and *rockets* in places due to the different regimes of temperature and speed in which they operate.

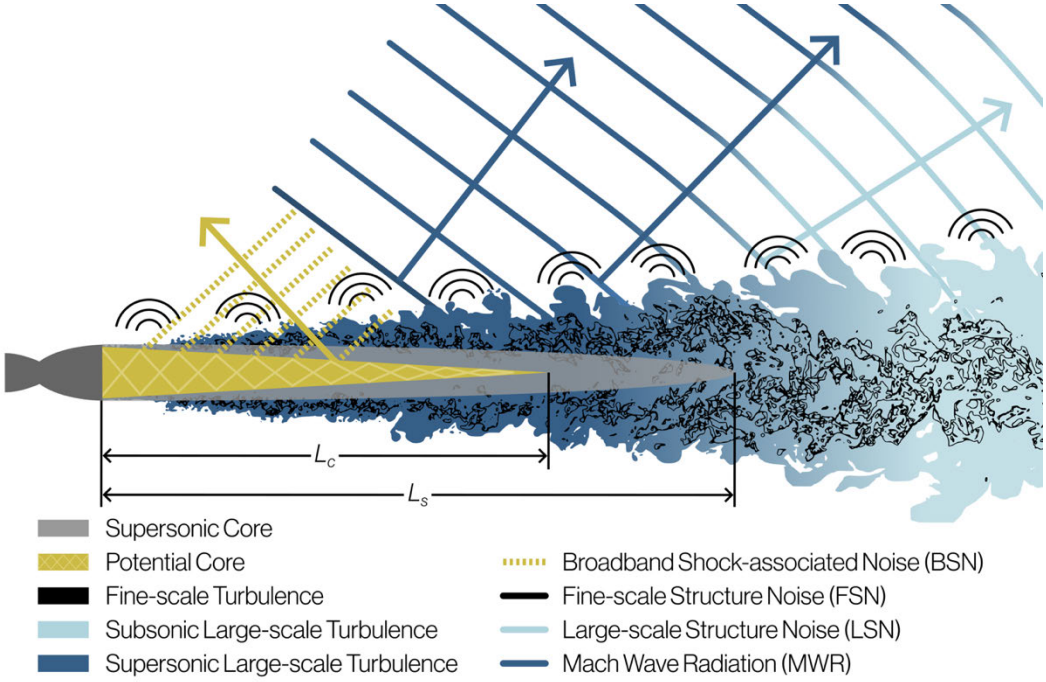

Figure 1.2. Schematic illustrating the anatomy of a supersonic jet and the various radiative noise sources.

The two-source model for jet noise, described by Tam and Chen (1994), Tam (1995), and Tam *et al.* (1996), attributes the dominant aft-radiating noise from supersonic jets to two distinct mechanisms: radiation from large-scale disturbances (also called turbulence or instability waves or wavepackets), and radiation from fine-scale turbulence, depicted in Fig. 2. The development of large-scale structures is driven by Kelvin–Helmholtz instabilities in the shear layer. These

structures are advected downstream, growing in size and decreasing in convective velocity. As they interact with the ambient fluid, they perturb the ambient air. When these perturbing structures travel faster than the ambient speed of sound, acoustic energy is efficiently radiated as the energy in the flow couples to the ambient air. This constitutes the efficient, coherent, and highly directional Mach wave radiation (MWR), which dominates the acoustic output of the jet plume.

The angular directivity of MWR depends on the convective Mach number, which describes the ratio of the wavepacket's convective speed to the local speed of sound. Numerous analytical and empirical models for estimating this quantity exist in the literature. As part of this dissertation's outcomes, the author worked on a collaborative effort to understand and clarify definitions of the convective Mach number, compare their applicability, and link them to the observed directivity of both jet and rocket noise (Gee *et al.* 2025a).

As these radiating disturbances move beyond the supersonic core of the jet, they decelerate and become convectively subsonic. Their radiation angle shifts further aft, and their radiative efficiency decreases, as much of it stays in the hydrodynamic near field and rapidly evanesces. This transition leads to noise behavior more typical of subsonic jets.

The second source in the two-source model—fine-scale turbulence—produces higher-frequency, omnidirectional noise that tends to dominate in the sideline direction. Due to the smaller spatial scale of these turbulent structures, their acoustic signature is less coherent but has higher characteristic frequencies than that of MWR.

A separate and important noise source emerges when a supersonic jet operates off-design. In a convergent-divergent nozzle, the flow first accelerates through a converging section, reaching Mach 1 at the throat (the narrowest point), before expanding and accelerating further through the

diverging portion. If the jet's exit pressure does not match the ambient pressure—as is typically the case—shock structures form downstream. These include alternating oblique shocks and expansion fans that create a periodic pattern of shock cells, often colloquialized as “Mach diamonds.” This is depicted in Fig. 1.3.

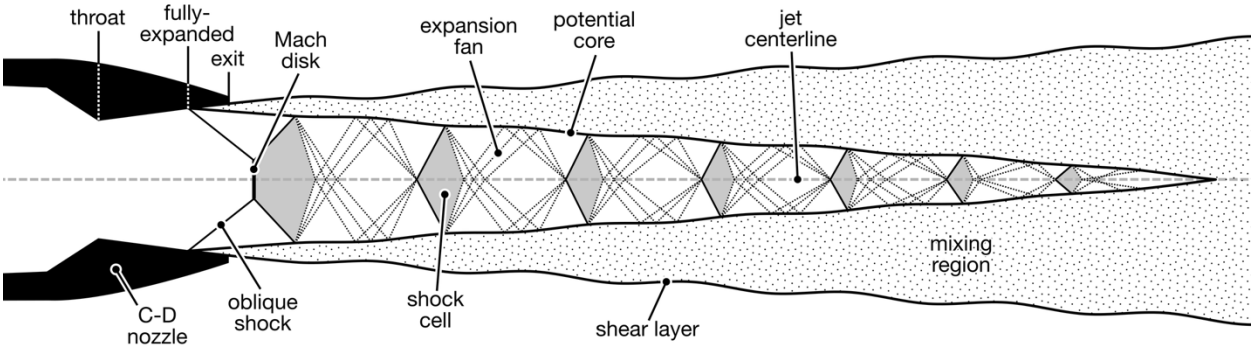

Figure 1.3. Schematic of an overexpanded jet’s potential core region showing the anatomy of the shock cells in the jet.

As turbulent perturbations in the shear layer propagate downstream, they interact with these shock cell boundaries, giving rise to two types of shock-related noise. The first is screech, a resonance phenomenon producing discrete tonal harmonics (Powell, 1953). While common in laboratory-scale jets, screech is generally absent in full-scale, afterburning-capable engines. The second type is broadband shock-associated noise (BBSAN or BSN), first characterized by Harper-Bourne and Fisher (1974). BSN is a directional noise source that primarily radiates forward, at inlet angles less than 90 degrees. It is a significant contributor to the forward noise field of full-scale aviation jet engines, though its acoustic relevance in rocket plumes has yet to be definitively demonstrated.

1.4 Noise Modeling

One of the primary goals in the field of jet noise is that of modeling and prediction. This can be for several reasons: producing environmental assessments, determining payload and structural vibroacoustic loads, predicting acoustical characteristics of new engine designs, etc. Early empirical models for jet aircraft and rocket noise (Franken, 1957; Eldred 1971) have continued to prove useful for far-field noise prediction, with their methodologies driving more recent predictive models.

Even as models have improved, there still remains significant progress to be made in this space. Particularly for rockets, measurements continue to identify areas in which current models are deficient in predictions (Gee, 2023; Gee *et al.*, 2024; Gee *et al.*, 2025b). While computational fluid dynamics and computational aeroacoustics tools continue to improve, they are primarily useful for characterizing near-field acoustic and flow-acoustic domain coupling characteristics. Due to both computational expense and a lack of far-field acoustic validations for these simulations, empirical models still retain merit for noise prediction. Further discussion on this topic is provided in the introduction of Chapter 6.

1.5 Objectives and Scope

While the mechanistic understanding of jet noise has made vast strides, there remain significant areas of research. While not present in most laboratory-scale and simulations of jets, full-scale tactical jet aircraft engines exhibit multiple radiation lobes at different frequencies, with distinct properties and directivities. This so-called spatiospectral lobing behavior has been observed at full-scale, but significant questions remain as to what the cause of this phenomenon

is. The absence of this phenomenon at lab-scale and in simulations suggests some sort of inherent flow physics difference between scales. Chapter 2 of this dissertation examines the source characteristics leading to spatiospectral lobing behavior from an afterburning GE F404 jet aircraft engine installed in a T-7A trainer aircraft using acoustical holography and coherence-based source decomposition techniques.

Additionally, sources of BSN remain largely uncharacterized at full-scale in aircraft jet engines, largely due to the impracticality of extracting meaningful near-field flow and acoustic measurements in this application. Hence, most of the body of research on BSN source characteristics have been examined for laboratory-scale and simulated jets. Chapter 3 of this dissertation leverages acoustical holography from a near-field microphone array to characterize BSN source characteristics in an installed, afterburning GE F404 engine.

With regards to rocket noise, most modern launch vehicles use an arrangement of multiple engine nozzles on their first stage. This introduces the possibility of complicating and/or altering the noise radiation relative to that of a single-nozzle configuration due to clustering effects and merging exhaust plumes. One possible effect is that of azimuthal noise asymmetry from a nonsymmetric nozzle arrangement on a rocket. Chapter 4 examines this thesis, leveraging acoustical measurements of an asymmetric, dual-nozzle Atlas V launch vehicle to examine this hypothesis. In particular, evidence for azimuthal asymmetry with regard to noise spectral peak frequency is presented.

Entering the modeling space, Chapter 5 concerns fundamental predictive methods for estimating the overall sound power and maximum overall sound pressure levels from supersonic jets. The development of models for these parameters is discussed, and the models are validated against both launched rockets, as well as a full-scale GE F404 jet aircraft engine operating at

several engine conditions. Additionally, evidence for different apparent acoustic efficiencies for two different rockets is presented.

Finally, Chapter 5 introduces SATURN: a scientific acoustic tool for understanding rocket noise. This model builds on the methodology of SP-8072 (Eldred, 1971) by updating model inputs with modern empirical data, including empirical propagation modeling, and packages the methodology in a modular, research-grade code for rocket noise prediction. SATURN is validated against two different rockets at a variety of distances, and compared to the legacy SP-8072 predictions.

In addition to the work contained in this document, the reader is also directed to other published research that the author made significant contributions to during the course of this dissertation in both the characterization of jet aircraft noise (Kumar *et al.*, 2025; Gee *et al.* 2025a) as well as rocket noise (Gee *et al.* 2022; Gee *et al.*, 2024, Gee *et al.*, 2025b). A summary of these contributions is given in Appendix A.

Chapter 2

Acoustical Holography and Coherence-Based Noise Source Characterization of an Installed F404 Engine

Understanding the acoustic source characteristics of supersonic jets is vital to accurate noise field modeling and jet aircraft noise reduction strategies. This chapter uses advanced, coherence-based partial field decomposition methods to characterize the acoustic sources in an installed, supersonic GE F404 engine. This chapter is an article published as L. T. Mathews and K. L. Gee, "Acoustical Holography and Coherence-Based Noise Source Characterization of an Installed F404 Engine," *AIAA J.* **62**(6), pp. 2186-2199 (2024). https://doi.org/10.2514/1.J063543. It is reprinted in this dissertation under the terms of AIAA's Rights and Permissions with the permission of the copyright holders, L. T. Mathews and K. L. Gee. I hereby confirm that the use of this article is compliant with all publishing agreements.

Acoustical Holography and Coherence-Based Noise Source Characterization of an Installed F404 Engine

Logan T. Mathews* and Kent L. Gee†
Brigham Young University, Provo, Utah 84602

https://doi.org/10.2514/1.J063543

Understanding the acoustic source characteristics of supersonic jets is vital to accurate noise field modeling and jet noise reduction strategies. This paper uses advanced, coherence-based partial field decomposition methods to characterize the acoustic sources in an installed, supersonic GE F404 engine. Partial field decomposition is accomplished using an equivalent source reconstruction via acoustical holography. Bandwidth is extended through the application of an array phase-unwrapping and interpolation scheme. The optimized-location virtual reference method is used. Apparent source distributions and source-related partial fields are shown as a function of frequency. Local maxima are observed in holography reconstructions at the nozzle lipline, distinct in frequency and space. The lowest-frequency local maximum may relate to noise generated by large-scale turbulence structures in the convectively subsonic region of the flow. Other local maxima are correlated primarily with Mach wave radiation originating from throughout the shear layer and into the fully mixed region downstream of the potential core tip. Source-elucidating decompositions show that the order and behavior of the decomposition lend to the local maxima being related to distinct subsources. Between the local maxima, however, there may be a combination of sources active, which is likely the cause of the spatiospectral lobes observed in other full-scale, supersonic jets.

Nomenclature

D_j	=	fully expanded jet nozzle exit diameter
$\boldsymbol{H}_{\mathrm{YP}}$	=	transfer matrix
h	=	height of jet centerline
K	=	number of selected virtual references
$\boldsymbol{L}$	=	lower-triangular matrix from Cholesky decomposition
L_c	=	potential core length
$\tilde{L}_c$	=	estimated potential core length
L_s	=	supersonic core length
$\tilde{L}_s$	=	estimated supersonic core length
M	=	number of partial fields in sum
M_j	=	fully expanded Mach number
N	=	number of candidate virtual reference locations
$\boldsymbol{P}$	=	matrix of complex pressures
P_{MUSIC}	=	multiple signal classification power
$\boldsymbol{R}_{\mathrm{noise}}$	=	noise subspace matrix
$\boldsymbol{S}_{\boldsymbol{xx}}$	=	cross-spectral matrix
$\boldsymbol{u}$	=	trial vector
$\boldsymbol{w}$	=	singular vector
$\boldsymbol{W}$	=	matrix of singular vectors
x	=	distance downstream of jet nozzle axis
$\boldsymbol{X}$	=	virtual-reference-selected complex pressures
y	=	horizontal distance from jet centerline
$\boldsymbol{Y}$	=	near-field acoustical holography-reconstructed complex pressures
z	=	vertical distance from the ground plane
γ_{ij}^2	=	coherence
$\boldsymbol{\Sigma}$	=	diagonal matrix of singular values

Presented as Paper 2023-3212 at the AIAA Aviation 2023 Forum, San Diego, CA, June 12–16, 2023; received 6 September 2023; revision received 27 December 2023; accepted for publication 26 February 2024; published online 23 April 2024.

*Graduate Student, Department of Physics and Astronomy; loganmathews@byu.net. Student Member AIAA.

†Professor of Physics, Department of Physics and Astronomy; kentgee@byu.edu. Associate Fellow AIAA.

I. Introduction

NOISE from high-performance military aircraft remains a significant concern for both communities adjacent to military installations and for those who work near the aircraft. Significant progress in the characterization and understanding of supersonic jet noise has been made; however, there remains much to be discovered about the noise sources. Particularly, the observation of multiple-lobed behavior in these supersonic jets [1–9] and a study of lobe properties suggest the existence of several active, quasi-independent, acoustic sources in the plume [5,8]. While hypotheses have been proposed for this multilobe phenomenon [10,11], none have yet proved conclusive.

Decomposition of acoustic fields can be a powerful tool for characterizing and localizing sources [12–14]. The ability to isolate independent sources into separable fields can provide significant insight into the location, extent, and behavior of such acoustic sources. While a variety of decomposition methods are available, the most useful source-elucidating decompositions separate independent acoustic sources accurately and with physical relevance, providing a basis for the jet noise field in terms of individual source contributions [15]. However, achieving such decomposition is challenging. If a sound field is created by multiple incoherent sources, the separability of the field is ensured, and the result is obtained straightforwardly. However, given the partial coherence of jet noise, the subsources can be considered neither completely coherent nor incoherent. The existence of multiple sources of noise with finite mutual coherence makes performing source decomposition difficult. Many traditional decomposition techniques, such as singular value decomposition (SVD), can produce nonunique results that depend on reference locations, and thus the resulting partial fields (PFs) are not guaranteed to be tied to physical sources [16]. Therefore, the development of methods to elucidate such sources is vital for producing physically meaningful results.

One such method, the optimized-location virtual reference (OLVR) algorithm, was developed by Wall et al. [17] for use in the analysis of supersonic jet noise. This method works in conjunction with near-field acoustical holography (NAH) to provide a physically meaningful PF decomposition (PFD) based on virtual references (VRs) that are placed near the presumed acoustic source using a NAH reconstruction. Candidate VRs are assigned a likelihood of being near an acoustic source, and VRs are selected to be separated by a coherence criterion, thus increasing the probability of targeting

independent (or poorly correlated) sources. The PF decomposition is then performed using these VRs as a guide for separating the field.

To achieve meaningful decompositions, however, a mesh of sufficient resolution must be available to separate acoustic fields near the source. For this task, acoustical holography is used to provide a reconstruction of the acoustic field at the nozzle lipline, where the OLVR decomposition can then be performed. In this paper, statistically optimized near-field acoustical holography (SONAH) is employed. Acoustical holography in some form has been applied to jet noise analyses previously by Wall et al. [3] and Leete et al. [5] for full-scale installed tactical engines, by Lee and Bolton [39], Long [18], Vold et al. [19], and Shah et al. [38] for laboratory-scale jets, and by Leete et al. [58] for a large-eddy-simulated supersonic jet.

Jet mixing noise is produced by the interaction of convected turbulence structures with the surrounding atmosphere. In supersonic, shock-containing jets, turbulence structures can interact with the shock cells to create a secondary source of noise, of which there are two divisions (broadband shock-associated noise and screech). While shock-associated noise is an important noise component of shock-containing jets, this paper focuses on mixing noise in supersonic jets, which is the dominant sound source in most full-scale tactical aircraft [20,21]. Within the realm of mixing noise, it has been suggested that there are two primary scales of turbulence that have differing radiative characteristics [22]. Smaller turbulence structures have been associated with omnidirectional noise radiation, while larger turbulence structures tend to radiate preferentially at angles of 110–160° relative to the jet inlet, depending on their convective speeds. Based on this understanding of jet noise, Tam et al. [23,24] have developed a two-source model for jet noise that uses these two categories to explain the spectral components of jet noise. In this framework, mixing noise is composed of large-scale structure noise (LSN) and fine-scale structure noise (FSN). Tam [25] suggested that LSN is primarily associated with Mach wave radiation (MWR) from supersonically convecting turbulence structures and that it is driven principally by the Kelvin-Helmholtz (K-H) mechanism. However, we note that throughout the literature, MWR and LSN have been used in a variety of contexts, and there are no universally agreed-upon uses of these or like terms. As such, we will adopt a particular definition of these terms for this paper and attempt to describe other findings accordingly.

This two-source model has been used widely in modeling the spectral characteristics of jet noise [19,20,26,27]. However, the two-source model has been found to not fully reproduce the spectral component of measured jet noise, specifically in full-scale tactical engines at high powers, including the T-7A aircraft used in this study [10,20,28]. Recent studies have suggested that noise from large-scale turbulence structures may not be associated with only one mechanism. Liu et al. [11] studied the effect of temperature ratio on radiated noise using large-eddy simulations. They found that with an increasing temperature ratio, directional mixing noise separated into two distinct noise components: one low-frequency component consistently radiating at 150° and one that radiated at higher frequencies and more upstream angles with an increasing temperature ratio. They associated the first component with what they termed LSN and the second with MWR. Likewise, Prasad and Morris [29] noted two noise components associated with large-scale turbulence structures: one related to the K-H instability that exhibited MWR, and another that exists as the flow decelerates beyond the potential core. In terms of wavepackets, Jordan and Colonius [30] described two different noise components associated with large-scale turbulence structures; one supersonic, generating noise through MWR, and another subsonic, which "leaked" noise through spatial modulation ("jitter"). Similarly, Schmidt et al. [14] identified two types of wavepackets present in supersonic jet turbulence. These were associated with the K-H and Orr-type instability waves. Their results suggested that the K-H instability existed primarily upstream of the potential core, while the Orr-type mechanism was active downstream of the potential core. While these studies were done in different paradigms and do not result in a complete, consistent framework for mixing noise radiation from supersonic jets, we simply note that they all suggest that there are at least two distinct noise radiation components. There is one higher-frequency noise component that originates farther upstream, generally radiates at >140°, and is associated with MWR from convectively supersonic turbulence structures. There is a second noise source that is localized further downstream, has a lower characteristic frequency, radiates at 140–160°, and may be associated with radiation from convectively subsonic turbulence. In this paper, we refer to the first component as MWR and the second as LSN.

The purpose of this paper is to investigate source-related characteristics and radiation phenomena of an installed, GE F404 engine using advanced PFD methods. Distinct local maxima are observed in acoustical holography reconstructions near the nozzle lipline. Multilobe radiation behavior in the field is observed at frequencies between local maxima. The OLVR method is used to produce source-elucidating PFs. OLVR decompositions show that, at frequencies where multilobed radiation in the field is observed, PFs containing distinct radiation lobes are present. From this, it is hypothesized that the local maxima likely correspond to distinct subsources involving phenomena such as MWR and LSN, and that multilobed radiation behavior is likely occurring due to the activity of distinct acoustic source regimes within the flow.

II. Methods

A. Measurement

The Boeing/Saab T-7A Red Hawk is an advanced jet trainer aircraft developed for the United States Air Force and is powered by the F404-GE-103 afterburning turbofan engine. This engine is a further development in the F404 family, which has been the subject of numerous acoustic studies [31–33]. Measurements were made in six runs of five different engine conditions: 75% N2, 82% N2, 88% N2, military power, and maximum afterburner (AB). The analyses in this paper will focus on the AB engine condition, with all six runs being concatenated for more averaging. At AB, the fully expanded Mach number (M_j) of the overexpanded jet is estimated to be 1.46, with TTR = 6.9 [34].

Acoustic data were obtained from an extensive measurement of the T-7A aircraft at Holloman Air Force Base in August 2019. Details of the measurement are provided by Leete et al. [6]. Numerous microphone arrays were deployed to measure the aircraft; however, this study focuses on a 120-element ground array placed near the aircraft, shown in Fig. 1a. A schematic of this array is shown in Fig. 1b and is referred to as the imaging array for its primary use in imaging-type

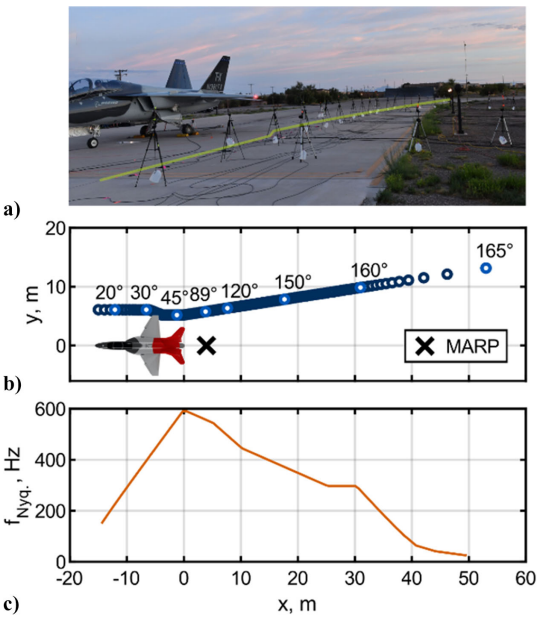

Fig. 1 a) Photograph of T-7A aircraft measurement with ground-based microphone array highlighted in yellow. b) Schematic of the array. c) Spatial Nyquist frequency of the array.

analyses such as acoustical holography and beamforming. The array spans a nearly 70 m aperture, from 15 m in front of the exit plane to ∼55 m downstream of the nozzle exit. To produce such an aperture with 120 microphones, element spacing was varied based on the expected frequency content as determined by studying prior full-scale jet noise studies, including those by Wall et al. [1], Tam and Powers [10], and Leete et al. [5], among others. The spatial Nyquist frequency for each microphone pair in the array is shown in Fig. 1c. The portion of the array near and ahead of the microphone array reference point (MARP; located at $x = 3.96$ m) was configured with relatively close microphone spacing, resulting in a higher spatial Nyquist frequency to accommodate broadband shock-associated noise (BSN) and other noise with significant high-frequency content. Notably, elements far downstream were given much greater spacing because of the anticipated dominance of lower-frequency MWR or LSN. This allowed for a greater aperture to be captured with a limited number of microphones while not sacrificing fidelity in areas where higher-frequency content is expected to dominate.

B. Bandwidth Extension

Conventional acoustic imaging techniques are bandwidth-limited by the spatial separation of transducers in the measurement. Such limitations ordinarily constrain results to frequencies below the design frequency/spatial Nyquist frequency of the array. Analyses at higher frequencies result in spatial aliasing that compromises the accuracy of the reconstructions. Given the limited number of transducers and large spatial aperture of this measurement, acoustical holography is limited to ∼400 Hz and below at the densest portion of the array. However, significant information about the jet noise source is contained above this frequency (such as the dominant energy from BSN). Thus, pursuing methods for bandwidth extension is needed to provide more information about the broadband jet noise source.

One method of extending the bandwidth of array-based measurements is the unwrapped phase array interpolation (UPAINT) method. This method, adapted from Goates et al. [35], spatially interpolates the magnitude and phase of the cross-spectral matrices (CSMs) produced by the measurement. It has been previously applied to jet noise for beamforming analyses by Harker et al. [36]. The key to this technique is unwrapping the aliased phase between each microphone pair in the CSMs. Conventional unwrapping techniques may be used; however, this paper applies a coherence-based pairwise phase unwrapping technique discussed by Cook et al. [37] that is well suited to partially coherent broadband signals such as those associated with jet noise. With the application of these methods, the results shown in this paper extend far above the array design frequency, presently validated up to a frequency of 1 kHz ($\sim Sr \leq 0.5$). A brief overview of the UPAINT procedure implemented for this study is given here for reference.

Phase unwrapping is accomplished in a microphone pair-by-pair sense across frequency. It should be noted that phase unwrapping spatially across the array, one frequency at a time (i.e., a 2D phase unwrapping of the CSM at a given frequency), can lead to significant errors. Spatial phase unwrapping, while producing visually acceptable results at each frequency, guarantees no meaningful phase relationship across frequencies. Thus, phase unwrapping must be undertaken across the frequency dimension for each microphone pair.

A CSM $\boldsymbol{C}$ may be defined from the computed complex pressures along the array as

$$\boldsymbol{C}(f) = \frac{1}{m}\boldsymbol{p_h}\boldsymbol{p_h}^H = \begin{bmatrix} G_{11}(f) & \cdots & G_{1m}(f) \\ \vdots & \ddots & \vdots \\ G_{m1}(f) & \cdots & G_{mm}(f) \end{bmatrix}$$

where $\boldsymbol{p_h} = \boldsymbol{p_h}(f)$ is the computed complex pressures along the array, m is the number of measurement points in the array, and $G_{ij}(f)$ is the cross-spectrum between the ith and the jth array elements.

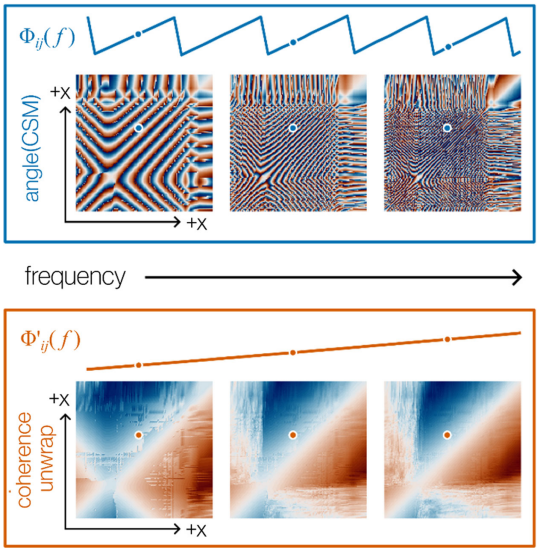

Fig. 2 Illustration of phase unwrapping on cross-spectral matrices. The unwrapped phase is shown above, and the coherence-unwrapped case is shown below.

The magnitude $|\boldsymbol{C}(f)|$ and phase $\boldsymbol{\Phi}(f) = \arg\{\boldsymbol{C}(f)\}$ may be computed directly from the CSM. Phase unwrapping is then accomplished for each given $\Phi_{ij}(f) \in \boldsymbol{\Phi}(f)$. While the methodology for standard phase unwrapping is discussed in Goates et al. [35], a coherence-based phase unwrapping technique for $\Phi_{ij}(f)$ is discussed here.

Signal coherence becomes an important factor in phase unwrapping when there is poor coherence between the two signals considered. Therefore, coherence is used as a criterion in the unwrapping process to reduce nonphysical phase unwrapping. First, for a given $\Phi_{ij}(f)$, points are classified based on whether they have sufficient coherence to allow for accurate phase unwrapping. This is done by selecting some coherence threshold value or scheme to classify points based on their relative coherence. Further discussion on the particular method used here is given by Cook et al. [37]. Then, a two-part scheme is used to unwrap the signal. First, those points above the coherence threshold are conventionally unwrapped. Then, a least-squares method is used to unwrap the remaining subthreshold points based on a selection of the closest neighboring unwrapped super-threshold points. This provides phase unwrapping for the entire signal while reducing the errors introduced by low coherence. An illustrative example of such an unwrapping scheme is shown in Fig. 2, where CSM phases are shown for three distinct frequencies. Axes have been added to show the spatial order of the CSM points in terms of x position. The direction of increasing frequency is indicated by an arrow. The phase relationship as a function of frequency for a given pair of microphones ($\Phi_{ij}(f)$) is shown above, where the microphone pair is indicated by the markers on the CSMs. The results of coherence-unwrapping each pair, $\Phi'_{ij}(f)$, is shown below. In this case, the signals are quite coherent, leading to a linear phase relationship.

C. Acoustical Holography

SONAH is an inverse method developed for a variety of acoustic problems and has been applied to jet noise sources [3,38–40]. An overview of the SONAH process is given here, but more detailed descriptions may be found in Refs. [41,42], with application to jet-noise-specific problems in Refs. [3,5]. The SONAH process is a method of leveraging a limited measurement array (often referred to as the hologram) to reconstruct acoustic properties at locations of interest. The SONAH process also involves certain techniques to address a limited-aperture measurement of a partially coherent jet noise source.

First, synchronously measured time-domain pressure signals across the array are Fourier-transformed to create frequency-dependent CSMs that contain both amplitude and phase information.

Multiple run-ups of the engine are used to increase the number of blocks to average over in determining CSMs. Second, the field is decomposed into partial, self-coherent fields using an SVD method. Third, various enhancements are made to mitigate finite aperture and discrete spatial sampling limitations, such as a numerical aperture extension using an analytic continuation method (see Ref. [43]), interpolation, etc. Then, it is assumed that the acoustical behavior at the hologram can be represented as a linear combination of wavefunctions (in a matrix $\boldsymbol{A}$) that satisfies the linear equation

$$\boldsymbol{Ac} = \boldsymbol{p_h} \tag{1}$$

where $\boldsymbol{c}$ is a vector of unknown coefficients and $\boldsymbol{p_h}$ is a vector of measured complex pressures at the hologram. The SONAH algorithm applied in this paper uses an equivalent wave model (EWM) based on a set of cylindrical wave functions defined relative to an axis along the jet centerline. These basis functions, composed of Hankel functions for the radial component and complex exponentials for the azimuthal and x dependence, are given by

$$\Psi_{l,k_x}(r,\phi,x) \equiv \frac{H_l^{(1)}(k_r r)}{H_l^{(1)}(k_r r_0)} e^{il\phi} e^{ik_x x}, r \geq r_0 \tag{2}$$

where r is defined as the radial distance from the jet centerline, r_0 is the radius of the reference surface where r_0 is chosen to be an appreciably small number (in this case $r_0 = 0.5$ mm), and the radial wavenumber k_r is determined by

$$k_r = \begin{cases} \sqrt{k^2 - k_x^2}, & |k| \geq |k_x|, \\ i\sqrt{k_x^2 - k^2}, & |k| < |k_x| \end{cases} \tag{3}$$

where the second case accommodates evanescent radiation, thus accomplishing the near-field portion of SONAH.

In this paper, only the $l = 0$ (axisymmetric) case is considered for the set of wavefunctions. Due to the measurement array being confined to the ground, the representation of higher-order azimuthal modes would be inaccurate. In addition, Leete et al. [44] showed favorable azimuthal coherence up to several hundred hertz for a high-performance military jet, lending credence to the inclusion of only the axisymmetric wavefunctions for this paper. The complete EWM is then formed as the matrix $\boldsymbol{A}$, given as

$$\boldsymbol{A} = \begin{bmatrix} \Psi_1(r_{h1}) & \cdots & \Psi_1(r_{hm}) \\ \vdots & \ddots & \vdots \\ \Psi_N(r_{h1}) & \cdots & \Psi_N(r_{hm}) \end{bmatrix} \tag{4}$$

where N is the number of wavefunctions used, r_{hv} is the radial distance of the vth measurement (hologram) point, and m is the number of measurement (hologram) points. A sufficient number of wavefunctions are generated to construct an effectively complete basis over a source-free region of interest. While no analytical criterion exists for determining what constitutes a complete basis in SONAH, a complete basis is effectively achieved when the addition of additional wavefunctions produces no change in the solution. Additional discussion on the selection of wavefunctions in $\boldsymbol{A}$ is given by Hald [42]. In essence, the matrix $\boldsymbol{A}$ is a transfer matrix from the hologram to a reference surface very close to the jet centerline. The inverse problem is then formulated as

$$\boldsymbol{c} = \boldsymbol{A}^{-1}\boldsymbol{p_h} \tag{5}$$

In practice, $\boldsymbol{A}$ is nonsquare, and the inversion is nontrivial. Depending on the dimensions of $\boldsymbol{A}$, the solution is obtained in either a least-squares or minimum-norm sense via a regularized inverse. This process results in the statistically optimized portion of SONAH, as the optimal solution is determined in solving the system [45]. Since holography involves an inward propagation of the field, noise present in the signals can quickly blow up, resulting in large errors in the reconstruction. To filter out high-order wavenumbers associated with nonacoustic noise, a modified Tikhonov regularization method [46] is employed, which acts as a low-pass filter. Once the inverse problem has been solved, a matrix $\boldsymbol{\alpha}$ is created to propagate out to reconstruction locations:

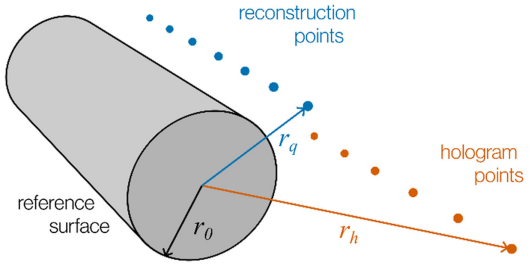

Fig. 3 A diagram showing the holography geometry with hologram (measurement) points, reconstruction points, and the reference surface.

$$\boldsymbol{\alpha} = \begin{bmatrix} \Psi_1(r_{q1}) & \cdots & \Psi_1(r_{qn}) \\ \vdots & \ddots & \vdots \\ \Psi_N(r_{q1}) & \cdots & \Psi_N(r_{qn}) \end{bmatrix} \tag{6}$$

where n is the number of reconstruction locations and r_{qw} is the radial distance of the wth reconstruction point. Figure 3 provides an illustration of the geometry for this holography process, with the reference surface of radius r_0, hologram points at radius r_h, and the reconstruction points at radius r_q.

Like the matrix $\boldsymbol{A}$, $\boldsymbol{\alpha}$ serves as a transfer matrix from the reference surface out to various reconstruction locations. The inverse problem can then be leveraged to predict acoustic properties at the reconstruction locations by evaluating the linear equation

$$\boldsymbol{p_q^T} = \boldsymbol{c\alpha} = \boldsymbol{p_h^T R_{A^H A} A^H \alpha} \tag{7}$$

where $\boldsymbol{R_{A^H A}}$ is the regularized pseudoinverse of $\boldsymbol{A^H A}$. Thus, the acoustic behavior at reconstruction locations is obtained from the hologram via a two-step transfer process. The SONAH process shown here is applied to complex acoustic pressure; however, its application can be extended to particle velocity as well, enabling the construction of acoustic intensity [47]. This paper focuses only on the acoustic pressure results.

D. OLVR Partial Field Decomposition

The OLVR methodology has been previously applied to jet noise measurements by Wall et al. [17]. This technique, however, is largely adapted from a PFD technique described by Kim et al. [16], who essentially showed that using VRs selected using a source-elucidating procedure to decompose the field produces physically meaningful PFs, closely mimicking the expected PFs in a laboratory experiment.

1. NAH Reconstruction

To elucidate information about the jet noise source, references should be placed near the jet such that source-related phenomena can be resolved. Kim et al. [16] found that the best PFD results were obtained when references were placed as close as possible to the physical sources. However, placing acoustic sensors near the jet is problematic, and thus an acoustic imaging method is employed to project measurements from a more distant location to near the jet, where VRs can be placed. In this application, SONAH is used to reconstruct the acoustic field at the nozzle lipline, a reasonable proxy for the acoustic source of a jet.

SONAH is an SVD-based NAH method that is used to provide accurate reconstructions of sound fields with multiple sources of limited mutual coherence. The SONAH formulation expresses

measured acoustic properties at a microphone array (called the hologram, see Fig. 4a) as a linear combination of appropriately chosen wavefunctions that form a basis for the acoustic field. This poses an inverse problem, where the wavefunction coefficients are determined in a least-squares or minimum-norm sense, producing the best fit of the chosen basis to the measured acoustic field. This set of wavefunctions and optimized coefficients comprises the EWM, which can be evaluated at other points of interest and can be thought of as a transfer operator that projects the measurement onto a desired surface or field of interest. This can be summarized as

$$\boldsymbol{Y}' = \boldsymbol{H}_{\mathrm{YP}}\boldsymbol{P}$$

where $\boldsymbol{P}$ is the measured hologram, $\boldsymbol{Y}'$ are the reconstructed complex acoustic pressures, and $\boldsymbol{H}_{\mathrm{YP}}$ is the transfer matrix determined by the SONAH algorithm.

To address multiple sources with limited mutual coherence, SONAH relies on an SVD-based PFD to separate the measured signals into energetically ordered, self-coherent PFs. This is done before the EWM is determined; thus, the EWM is computed for each PF, and the resulting field reconstruction is represented as an energetic sum of the resulting PFs.

2. *Selection of Virtual References*

With an equivalent source representation produced through NAH, VRs can then be placed in the field, which will provide a new basis for separation into physically meaningful PFs. Notably, VRs can be placed anywhere in the field with NAH. In this paper, candidate VRs are placed along the jet lipline (represented in Fig. 4a) to attempt the separation of independent source mechanisms. Candidate VR locations were further spatially restricted to be no farther downstream than the point where the level at the lipline was less than 20 dB from the maximum value. This restriction ensures that candidate locations are placed in regions where meaningful energy is being emitted. The OLVR algorithm uses two subroutines to select VRs: a metric for determining the likelihood of sources in the vicinity of a VR and a spatial coherence-based separation of VRs.

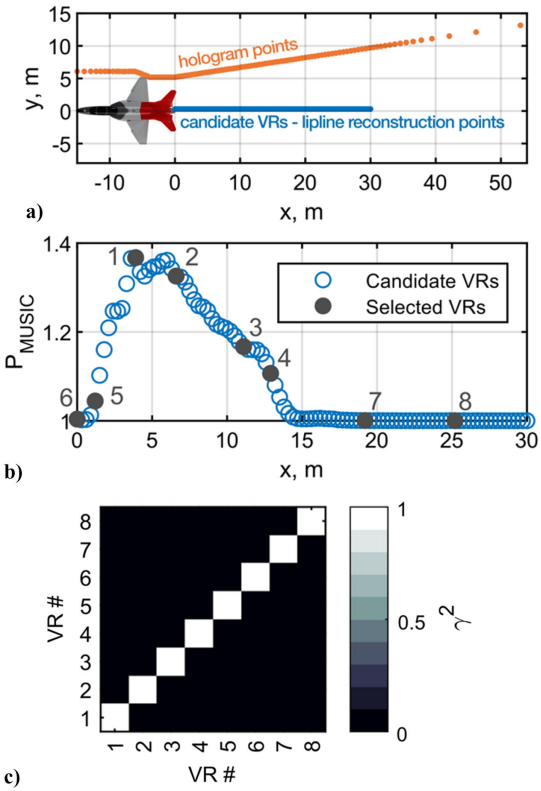

Fig. 4 Outline of VR selection scheme. a) Measured hologram and candidate VRs. b) MUSIC power at candidate and selected VRs. c) Coherence between selected VRs.

To select VRs that are likely to be near acoustic sources, the multiple signal classification (MUSIC) power [48–50] is computed at each candidate VR location. The MUSIC power algorithm provides an estimate of the likelihood that an acoustic source is located at any given point. To calculate the MUSIC power, the CSM at each candidate VR location, $\boldsymbol{S}_{yy}^{N\times N}$, is estimated for every SVD PF; that is,

$$\boldsymbol{S}_{yy}^{N\times N} = \boldsymbol{Y}\boldsymbol{Y}^{H}$$

where $\boldsymbol{Y}^{N\times L}$ is a vector of reconstructed complex pressures at each candidate VR location. Following this, the CSMs are decomposed via SVD to obtain

$$\boldsymbol{S}_{yy}^{N\times N} = \boldsymbol{W}\boldsymbol{\Sigma}\boldsymbol{W}^{H}$$

where $\mathrm{diag}(\boldsymbol{\Sigma}^{N\times N})$ are the singular values and the unitary matrix $\boldsymbol{W}^{N\times N} = [\,\boldsymbol{w}_1\ \boldsymbol{w}_2\ \cdots\ \boldsymbol{w}_N\,]$ contains the associated singular vectors. If there are $K \le N$ independent sources in the field, then there are K source-related and $N-K$ noise-related singular vectors. Thus, the signal space can be partitioned into two subspaces—one associated with noise and one associated with sources. The noise subspace, $\boldsymbol{R}_{\mathrm{noise}}^{N\times N}$, is calculated as

$$\boldsymbol{R}_{\mathrm{noise}}^{N\times N} = \sum_{n=K+1}^{N} \boldsymbol{w}_n \boldsymbol{w}_n^{H}$$

In practice, determining the order of K for a jet noise source is a heuristic. The jet noise source, composed of turbulence, has no finite number of sources but a quasi-ergodic distribution of turbulent perturbations. Thus, K must be chosen to represent the total field appropriately. Similar to the approach used by Wall et al. [17], K was chosen to be the number of singular values in $\boldsymbol{\Sigma}$ within 20 dB of $\max(\boldsymbol{\Sigma})$. This criterion was chosen to be less than the 40 dB in Ref. [17], as the number (and spatial extent) of VRs in this paper are fewer. While this method produces favorable results, further investigation into the estimation of K is warranted.

The noise subspace is then used to determine the MUSIC power at each candidate location. Given the orthogonality of the SVD, $\boldsymbol{R}_{\mathrm{noise}}$ is orthogonal to the span of the source-related singular vectors. This is exploited in the determination of the MUSIC power. To calculate the MUSIC power, a trial vector is used to "sift" the noise subspace for likely sources. The trial vector is defined as

$$\boldsymbol{u}_n^{N\times 1} = [0\ \cdots\ 0\,1\,0\ \cdots\ 0]^{T}$$

where the vector is composed of zeros, with only the nth component being unity. The trial vector is, however, alterable based on the type of source, with further discussion given by Kim et al. [16]. This version of the trial vector assumes point (monopole) sources; however, a trial vector could be designed that assumes a particular source distribution. Further investigation into trial vectors for jet noise sources is needed. The MUSIC power is then calculated for the nth candidate location as

$$P_{\mathrm{MUSIC}} = \frac{1}{\boldsymbol{u}^{T}\boldsymbol{R}_{\mathbf{noise}}\boldsymbol{u}}$$

This routine is performed for each of the N candidate VR locations. Due to the orthogonality of the source- and noise-related subspaces, if $\boldsymbol{u}_n^{N\times 1} = \boldsymbol{w}_n^{N\times 1}$ for $n = 1$ to K (the source-associated singular vectors), the denominator approaches zero and the MUSIC power becomes infinite. Thus, if the assumed source distribution, $\boldsymbol{u}_n^{N\times 1}$, matches the "actual" source distribution, the MUSIC power becomes large. Thus, higher values of the MUSIC power calculated with the trial vectors indicate a higher likelihood of being near an acoustic source. In practice, with distributed sources and many candidate VR locations, the range of MUSIC powers calculated is relatively small. The finer the resolution of the VR grid (i.e., the larger the value of N), the smaller the variation in the MUSIC power.

If the field contained ideal point sources, the MUSIC power, computed using this trial vector, would theoretically produce a "comb"-like result that would localize the sources precisely. However, with a distributed source, the MUSIC powers form a smoothly varying distribution, as seen in Fig. 4b. If only high MUSIC powers were chosen without considering the location of these points, the separation of sources would be poor. This is because there are redundant VRs that identify the same source. Kim et al. [16] suggest that in the case where the number of incoherent sources is greater than N (i.e., redundancy of candidate VRs is likely), that coherence be used to separate VRs. VRs with high MUSIC power and high mutual coherence likely identify the same source, and thus a set of VRs with high MUSIC power and low mutual coherence is sought.

The search for this set of VRs begins by reordering the complex acoustic pressures of all candidate VRs ($\boldsymbol{Y}^{N\times L}$) in order of MUSIC power as $\boldsymbol{X}'^{N\times L}$, then calculating the associated CSM $\boldsymbol{S}_{yy}^{N\times N} = \boldsymbol{X}'\boldsymbol{X}'^{H}$. From this, the coherence between candidate locations i and j is calculated as

$$\gamma_{ij}^2 = \frac{|S_{ij}|^2}{S_{ii}S_{jj}}$$

where S_{ij} is the ijth component of $\boldsymbol{S}_{yy}^{N\times N}$. Then, an iterative algorithm is used to select the set of VRs with high MUSIC power and low mutual coherence. First, the candidate location with the highest MUSIC power is selected as the first VR. Then, a coherence criterion is chosen (γ_{crit}^2), starting with a low value. The second VR is chosen as the location with the next highest MUSIC power, whose mutual coherence with the previous VR is less than the coherence criterion ($\gamma_{ij}^2 < \gamma_{\text{crit}}^2$). This process is repeated until either K VRs have been identified, or there are no more possible VRs below the coherence threshold. In the latter case, the coherence criterion is then increased, and the process is repeated until a full set of K VRs is found.

Then, a final matrix of coherence-separated, high MUSIC power VRs is constructed as

$$\boldsymbol{X}^{K\times L} = \begin{bmatrix} \boldsymbol{Y}_{R_1} \\ \vdots \\ \boldsymbol{Y}_{R_K} \end{bmatrix}$$

where $\boldsymbol{Y}_{R_k}$ is the R_kth row of $\boldsymbol{Y}^{N\times L}$, with R_k being the index of the kth selected VR.

3. *Decomposition by Virtual References*

The utility of VRs is realized in the decomposition technique. With the selected VRs, $\boldsymbol{X}^{K\times L}$ is decomposed into an orthogonal basis that ideally corresponds to the independent, incoherent sources. The decomposition method used follows the partial coherence decomposition (PCD) method, discussed in detail by Bendat [51]. This method relies upon the Cholesky decomposition to iteratively remove energy from the VR CSM. This CSM is constructed as

$$\boldsymbol{S}_{xx}^{K\times K} = \boldsymbol{X}\boldsymbol{X}^H = \boldsymbol{L}\boldsymbol{L}^H$$

where $\boldsymbol{L}^{K\times K} = [\boldsymbol{l}_1\ \boldsymbol{l}_2\ \cdots\ \boldsymbol{l}_K]$ is a lower-triangular matrix of linearly independent vectors, $\boldsymbol{l}_k$. Due to the nature of the Cholesky decomposition, each vector $\boldsymbol{l}_k$ contains all the energy that is coherent with the kth VR, as the energy is removed iteratively. With this new basis set, the OLVR PFs can then be generated. First, the CSM between all M field points and all K VRs is computed as

$$\boldsymbol{S}_{xy}^{K\times M} = \boldsymbol{X}\boldsymbol{Y}^H$$

Then, the OLVR PFs are generated from this CSM using the basis set as

$$\boldsymbol{P}_{\boldsymbol{x}}^{M\times K} = \boldsymbol{S}_{\boldsymbol{xy}}^{H}(\boldsymbol{L}^H)^{-1}$$

This is the final step in the OLVR algorithm. The resulting OLVR PFs, $\boldsymbol{P}_{\boldsymbol{x}}^{M\times K}$, are separated based on likely, incoherent sources. This increases the likelihood of PFs being physically meaningful since they were generated using VRs of high MUSIC power and low mutual coherence. The OLVR PFs, $\boldsymbol{P}_{\boldsymbol{x}}^{M\times K}$, are necessarily ordered spatially according to the VRs as a byproduct of the decomposition method. For this paper, they are finally re-ordered according to integrated energy from highest to lowest.

III. Results

A. Validation

To provide a first-order validation of the holography method, a reconstruction at the imaging array is compared to the original measurement. Ideally, the reconstructed acoustic behavior should match, but errors are introduced by the holography process. A measured spatiospectral map along the array is presented in Fig. 5 for the AB engine condition. Noticeable in this map is the dominant radiation region, which contracts and moves upstream with increasing frequency. Also visible are spatiospectral lobes, which manifest as distinct local maxima in the map. BSN is manifest near the nozzle at higher frequencies (above $Sr = 0.3$), making a "j"-type shape in the map.

Significant energy is present between $Sr = 0.1$ and $Sr = 0.3$, which is consistent with the general understanding of jet noise in the literature. However, much energy is present well below $Sr = 0.1$, with a large local maximum appearing far downstream around $Sr = 0.05$. It should be noted that the results here are for the afterburning condition, where the TTR approaches seven. Other studies, such as that by Liu et al. [11], have shown the emergence of high-amplitude noise below $Sr = 0.1$ in high TTR jets. It should also be noted that noise from rockets (substantially hotter and faster than jets) exhibits characteristic peak frequencies approximately an order of magnitude lower than other supersonic jets [52,53]. This shift in Strouhal number to lower frequencies with increasing TTR and jet velocity is an open matter of research in the literature.

Figure 6 shows the SONAH reconstruction error at the imaging array for the AB engine condition, with (Fig. 6b) and without (Fig. 6a) the application of the UPAINT bandwidth-extension method. Contours are drawn to show the regions corresponding to the −10 and −20 dB re maximum regions, indicating the areas of greatest energetic importance. Although this preliminary application of the UPAINT algorithm introduces errors upstream and

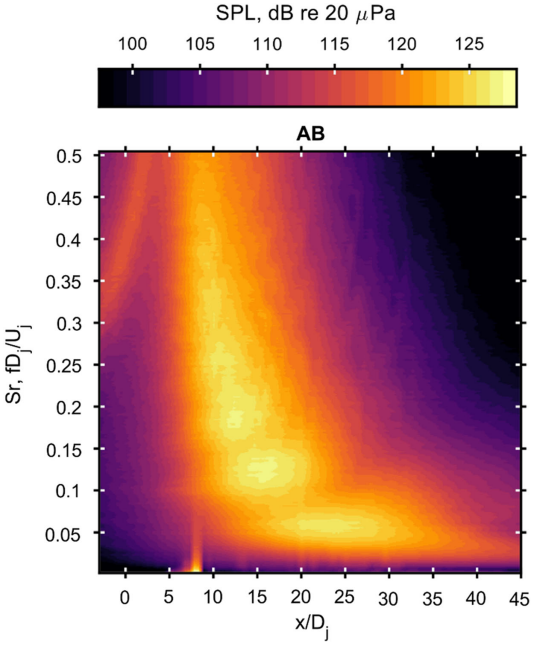

Fig. 5 Measured spatiospectral maps along the imaging array for MIL and AB engine conditions.

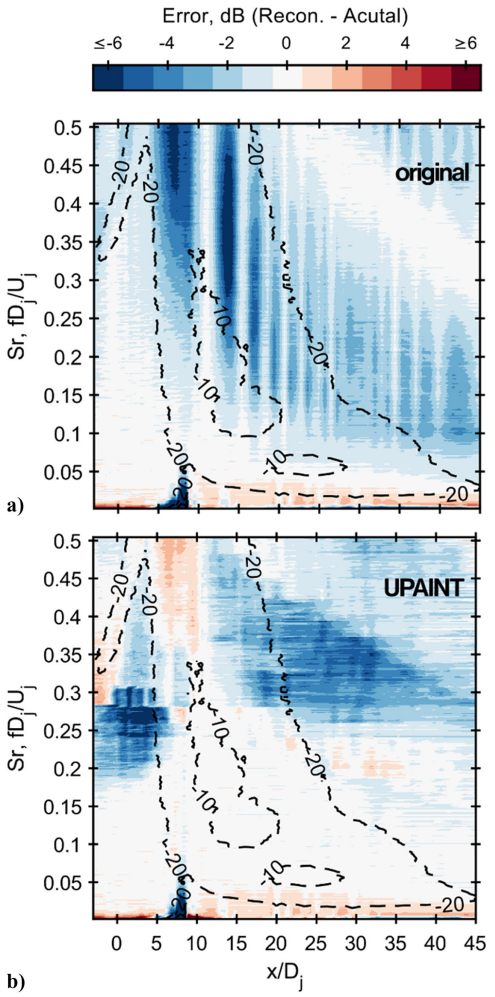

Fig. 6 Reconstruction error at the imaging array for the AB engine condition for a) the original measured data and b) after applying UPAINT.

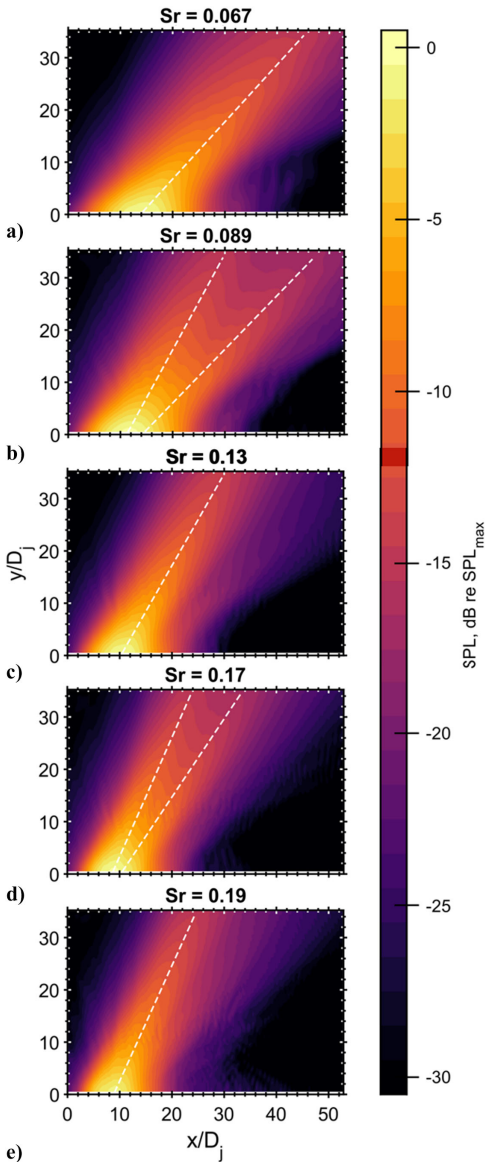

Fig. 7 SONAH reconstruction at AB for five frequencies of interest at the ground plane ($z = 0$).

downstream of the highest amplitude regions (where the signal is relatively low), it is important to note that it significantly improves reconstruction accuracy within the −10 dB contour. While this first application of UPAINT has yielded appreciable improvements in areas of greatest energy, further refinements are being explored to achieve greater accuracy overall, especially in regions with lower amplitude signals. It is worthy of note that, due to the installed nature of this jet, locations near and upstream of the nozzle/aircraft may have aircraft-related scattering. This may account for some of the difficulty in the phase unwrapping and interpolation near the nozzle seen in Fig. 6, since scattering would likely corrupt or mask the true phase information at affected locations, resulting in erroneous phase unwrapping and/or poor interpolation.

B. Field Reconstructions

SONAH field reconstructions at the ground ($z = 0$) are shown in Fig. 7 for the AB condition at five frequencies of interest, which will be discussed further in subsection C. Figures 7a, 7c, and 7e show a single dominant radiation lobe in the field, whose direction has been highlighted by the white dashed lines. However, Figs. 7b and 7d, located at intermediate frequencies, display multilobed radiation behavior, which is also highlighted. Also visible is the trend for the dominant radiation angle to shift forward with increasing frequency. These patterns of single-lobed radiation behavior shifting to multilobed behavior and then back to single-lobed behavior have been observed and characterized with several other installed tactical engines [5,8,70]. These multiple radiation lobes have been commonly referred to as "spatiospectral lobes" due to their manifestation in both space and frequency, and recent investigations have also characterized the temporal structure of these lobes [53].

C. Apparent Source Reconstructions and Local Maxima

A spatiospectral reconstruction is performed at the nozzle lipline as an analogous source representation. As the locations of actual acoustic sources (turbulent structures undergoing rapid convection) are ill-defined, the nozzle lipline serves as a surrogate for the source region. Although the approximate shear layer could be assumed, for the region considered in this analysis, the difference between the two is very small, and the results would be largely equivalent. The reconstruction at the afterburner across a wide range of frequencies along the nozzle lipline is shown in Fig. 8a. Local maxima (LMs) are observed, distinct in frequency and space, and are highlighted by contours corresponding to −1 dB re max level in the enclosed region. These LMs are similar in appearance to those shown for other tactical aircraft by Leete et al. [5] and Wall et al. [3], and they have been postulated to be related to the phenomenon of so-called spatiospectral lobes. The local maxima centers are quasi-harmonic, an observation that has been shared with the spatiospectral lobe phenomenon [54,55]. Several theories have been proposed to explain this nearly harmonic nature of the spatiospectral lobes, including shock–cell interaction [3,5]. However, no definitive explanation has been found

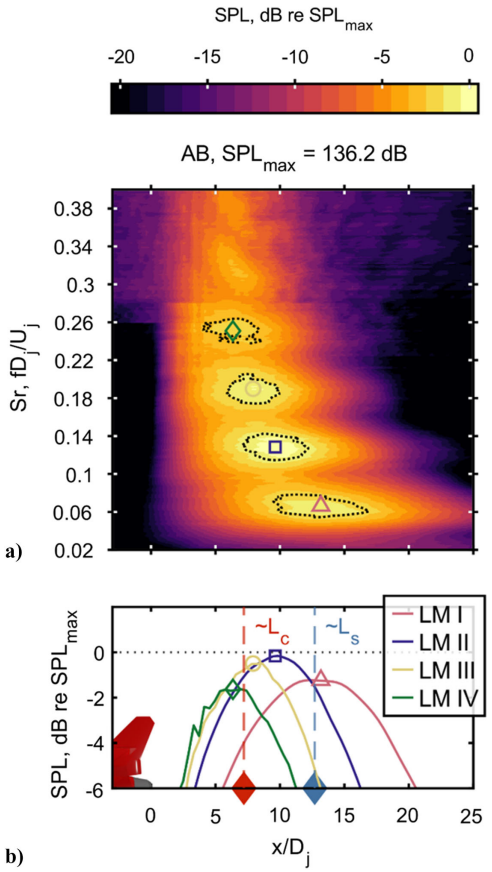

Fig. 8 Apparent source spatiospectral reconstructions at the nozzle lipline at AB. Relative SPL contours are shown for each of the identified local maxima.

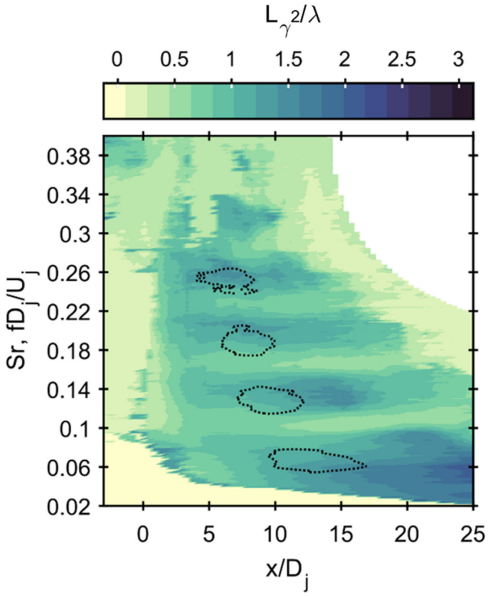

Fig. 9 Acoustic wavelength-normalized coherence length along the nozzle lipline at AB from NAH. LM contours from Fig. 8 are overlain in black dots.

to date. In this reconstruction, four LMs have been highlighted by contours; however, five or more are visible, though their appearances become more irregular at higher frequencies where the performance of the SONAH method begins to degrade. For this analysis, only the first three LMs are considered since they lie within frequencies where the SONAH method is most accurate.

Below the reconstruction (Fig. 8b) are the relative spatial SPL distributions of the first four highlighted LMs. These distributions correspond to the center frequency of each LM. Overlain on the subplots are the approximate locations of the potential and supersonic core tips ($\tilde{L}_c$ and $\tilde{L}_s$, respectively). More discussion on the approximate location of these regions is given in Mathews et al. [56,57]; see also Leete et al. [58] and Liu et al. [11,59,60].

The energetic order of the LMs, from greatest to least, is II, III, I, and IV. Spatially, LM II falls midway between $\tilde{L}_c$ and $\tilde{L}_s$, which has long been regarded as the region of maximum sound power production of the jet [61–63]. While LM II has the greatest amplitude, LM III is only slightly lower in amplitude. Thus, while LM II is well within the region between $\tilde{L}_c$ and $\tilde{L}_s$, the combination of LM II and III peaks very near but just downstream of $\tilde{L}_c$. This is consistent with findings from laboratory-scale heated jets by Baars et al. [64], who observed that the primary flow instability in the jet grew throughout the shear layer, reached a maximum just downstream of L_c, then decayed.

To further characterize the local maxima and their properties, Fig. 9 shows the upstream coherence length normalized by the acoustic wavelength calculated along the nozzle lipline at AB. Although the dimensional coherence length decreases at higher frequencies, caused by a decrease in the characteristic scale of the turbulence producing the noise, this normalization reveals greater self-similarity and allows for a relative comparison of coherence lengths across frequencies [55]. Coherence information was obtained through the SONAH reconstruction. Here, coherence length is defined as the distance required for the coherence between two points to drop from unity to below a threshold of 0.5. The portion of the plot in the upper right corner has been excluded as the reconstruction accuracy in this area is poor, and hence the results in this region are likely nonphysical. It should be noted that this downstream region at high frequencies has low amplitude and contributes very little to the total radiation, and hence any coherence information in this area would be of little value. Overlain on the plot are the contours corresponding to the local maxima from Fig. 8. The areas around the local maxima have a greater normalized coherence length, while the normalized coherence length appears to drop at frequencies between the local maxima. This reinforces the idea that the local maxima represent distinct, quasi-independent radiators. The shortening of the coherence length at frequencies between the LMs where multilobed radiation behavior is present in the field suggests that there may be more uncorrelated sources active. These observations are consistent with the coherence findings of Harker et al. [65] and Swift et al. [55], who showed that local maxima in their data, attributed to the spatiospectral lobe phenomenon, had higher relative coherence.

D. Source Decompositions

Since the LMs indicated in the previous discussion demarcate the most acoustically active frequencies near the source, decompositions can be performed at these frequencies to describe the spatial distribution of potential acoustic sources that contribute to each of these LMs. Additionally, frequencies between these LMs are where multiple-lobed behavior is observed in the field (as seen in Fig. 7), so decompositions can be performed here to identify potentially separate source phenomena present that may contribute to the multi-lobed radiation effect. The OLVR method was used to perform these decompositions. The coherence criteria used and the number of resulting PFs are summarized in Table 1. Note that with increasing frequency, more OLVR PFs (K) were selected in the algorithm, indicating the greater complexity of the field. This has been noticed

Table 1 OLVR process parameters for each frequency analyzed at the AB engine condition

LM#	Sr	γ^2_{crit}	K	M
I	0.067	0.33	4	3
I–II	0.089	0.30	6	4
II	0.13	0.31	7	4
II–III	0.17	0.36	13	7
III	0.19	0.32	9	4

in the field by Swift et al. [55], who showed reduced coherence length with increasing frequency when normalizing by acoustic wavelength. As Wall et al. [66] have shown coherence length to be an important figure of merit in sensing subsources, the result of achieving appreciably low coherence criteria in the decomposition is that the VRs separated are separated by greater than one coherence length. Noticeably, at frequencies between the LMs, more OLVR PFs (K) were required to represent the source, indicating that there are likely more sources of low mutual coherence at these frequencies. For example, LM II requires $K = 7$ PFs, and LM III requires $K = 9$. However, between these LMs, the number of PFs jumps to $K = 13$. Additionally, the number of OLVR PFs at the lipline within 10 dB of the maximum lipline SPL (M) also increased. For example, $M = 4$ for PF II and III, while between them, this jumps to seven. If the LMs do correspond to distinct, incoherent sources, then it would make sense that at frequencies between LMs, where principally two LMs may be contributing to radiation, there would be a greater number of deduced sources of low coherence. In terms of implications for reduced-order models of jet noise, this shows that frequencies around the LMs represent relative local minima in terms of the order of models required, while between the LMs, higher-order models are required to accurately represent full-scale radiation.

Figure 10 shows the results of OLVR decomposition at AB for the five frequencies of interest. Normalized levels of the first 4 OLVR PFs along the nozzle lipline are shown. The resulting energetic sum of the first four OLVR PFs is also shown. At the first frequency (Fig. 10a), the first four PFs produce an accurate representation of the total lipline SPL. As the frequency increases, four PFs become insufficient to accurately reproduce the total energy. This noticeably affects the upstream and downstream areas the most. This is due to a shortening of the coherence length both upstream and downstream at the source as frequency increases, which is shown in Fig. 9. Due to this, more PFs are necessary at these higher frequencies to accurately represent the source.

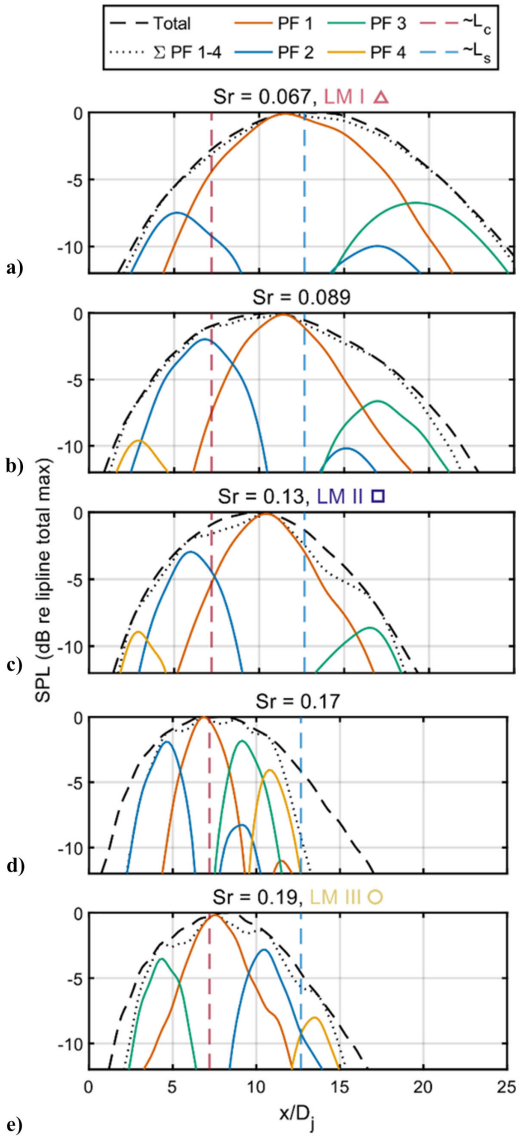

Fig. 10 OLVR decompositions for five frequencies of interest. Relative partial field levels along the lipline are shown.

In examining the OLVR decompositions further, Fig. 10a, corresponding to LM I ($Sr = 0.067$), consists of one primary OLVR PF, with the other remaining PFs being ~6 dB less in peak amplitude. Spatially, this corresponds with the field likely being composed of one principal acoustic source, which appears to be located near $\tilde{L}_s$ as the flowfield transitions locally to fully subsonic behavior. For Fig. 10c, corresponding with LM II ($Sr = 0.13$), there are two dominant sources likely, with the lower amplitude one peaking in the potential core region and the dominant one peaking between $\tilde{L}_c$ and $\tilde{L}_s$. Between LM I and LM II in frequency (Fig. 10b), the decomposition yields a primary PF reaching a maximum just before $\tilde{L}_s$, and a second PF, only about 2–3 dB less in maximum amplitude, near the end of $\tilde{L}_c$. At this frequency, multilobed behavior is observed in total field reconstructions; thus, this decomposition suggests that there are two primary active acoustic sources within 3 dB of the maximum magnitude of each other with low mutual coherence (less than or equal to $\gamma^2 = 0.30$). Spatially, these two likely sources appear to have maxima just before end of $\tilde{L}_c$ and just before the end of $\tilde{L}_s$.

For Fig. 10e, corresponding to LM III ($Sr = 0.23$), there are similar arrangements of the OLVR PFs as in Fig. 10c, with the dominant field (PF 1) reaching a maximum near $\tilde{L}_c$, with another high-amplitude contributing PF in the potential core region (PF 2). Here, though, the PF in the potential core region is of much higher amplitude, being only 2–3 dB lower in amplitude than PF 1. Thus, it appears that LM III may be comprised primarily of radiation from the shear layer region, with the primary source locations being near or upstream of $\tilde{L}_c$. Finally, at a frequency between LM II and LM III, Fig. 10d shows the PF 1 maximum being just ahead of the $\tilde{L}_c$, with LM III being 2–3 dB lower in amplitude, and the other two PFs being ~7–8 dB lower in amplitude than PF 1.

The OLVR decomposition yields PFs that can represent the field accurately in a significantly reduced-order sense. Figure 11 shows the relative error between the total reconstructed holography field and the sum of the first M OLVR PFs at the ground plane, where M has been defined as the number of OLVR PFs within 10 dB of the nozzle lipline maximum value. Dashed contours are drawn on the error plots to demarcate the −10 dB re max region of the field reconstruction. The inclusion of the first M OLVR PFs shows highly accurate representations of the acoustic field within the highest amplitude regions with a relatively small number of PFs. Such results show that reduced-order modeling of jet noise can be accomplished with relatively low-order models at these frequencies of interest. In all cases, the greatest error appears in the upstream direction, where the field is known to have low coherence. This has been accommodated previously in reduced-order models by increasing the order (adding more wavepackets) [67] or by including a secondary compact noise source such as a monopole [68].

To visualize the contribution of each OLVR PF to the acoustic radiation pattern, Fig. 12 shows the total field reconstruction and the first four OLVR PFs for each frequency analyzed on the plane $z = 0$ at AB. Dashed contours are overlain for the −10 dB re max total level. At the frequency corresponding to LM I, PF 1 (Fig. 12b) primarily contributes to the radiation lobe observed in the total field, with PF 2 and PF 3 (Figs. 12c and 12d) contributing up and downstream of PF 1 at significantly lower amplitudes (8–10 dB lower). Similar behavior is observed for LM II and LM III, with the relative amplitudes of higher-order PFs growing. At frequencies between the LMs, multilobe radiation behavior is observed in the total field reconstructions (Figs. 12f and 12p). Between LM II and III in particular, PF 1 and 2 primarily contribute to the dominant lobe

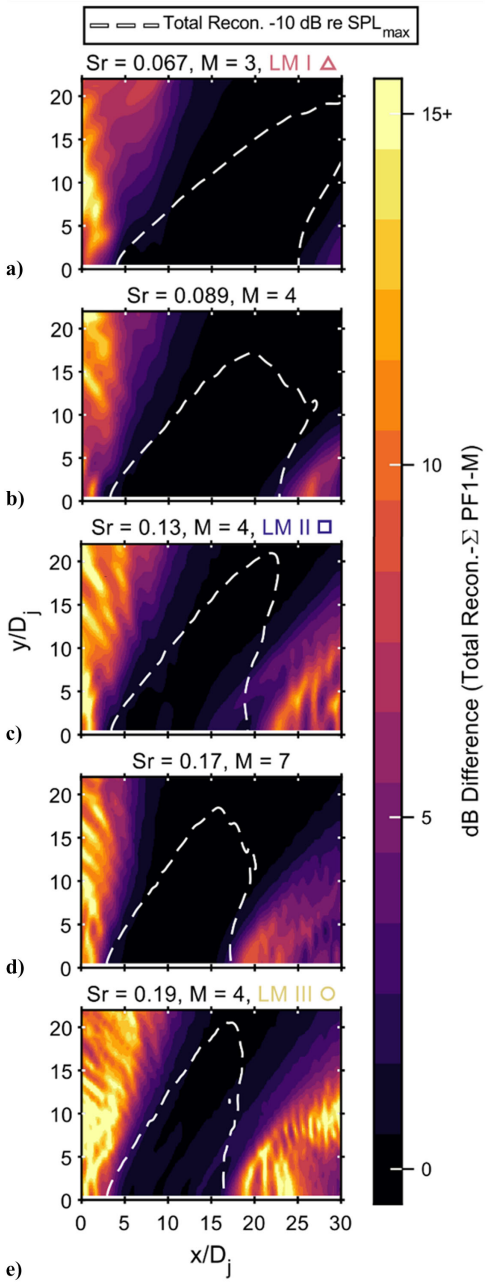

Fig. 11 The relative error at the ground plane is shown between the total reconstruction and the energetic sum of OLVR PFs 1 − *M*.

(Figs. 12q and 12r), while PF 3 contributes mainly to the second, less-energetic lobe (Fig. 12s). Note that at both frequencies between LMs, the OLVR PFs are not strictly contributing to one radiation lobe. This is readily observed in Figs. 12h and 12r. While each of these PFs contributes mainly to one lobe, they retain some energy from the other radiation lobe. This aligns with what is understood about spatiospectral lobes; they have low but finite coherence [55,69,70]; thus, the presence of some energy in each lobe in a given PF is expected. However, there is a possibility of these residues being present in part due to numerical error; however, since a finite coherence criterion was used to select and separate the PFs, this "sharing" of energy is likely due primarily to the coherence between VRs used to decompose the field.

A notable feature of the separated PFs is that at frequencies corresponding to LMs, the PFs have roughly the same directivities, whereas, between the lobes, PFs reflect different directivities. At LM-associated frequencies, the "breaking up" of the single radiation lobe into multiple PFs of similar directivity may be because the source is likely several coherence lengths long. The effect depends on frequency: at $Sr = 0.067$ (LM I), PF1 (Fig. 12b) contains much of the primary radiation. PF 2 and PF 3 (Figs. 12c and 12d) are much lower in amplitude. Thus, the splitting of the most energetic source region has a relatively low effect. At $Sr = 0.19$, however (LM III), PF 1–3 (Figs. 12v–12x) have similar directivities and both have relatively high amplitudes (all within 6 dB of the maximum). This may reflect the most energetic region of the source being more than a coherence length. Harker et al. [65] have shown that coherence length shrinks disproportionately more than the extent of the source region in full-scale supersonic jets; thus, the placement of OLVR VRs greater than a coherence length apart results in splitting the primary source region at higher frequencies into multiple PFs. Thus, even though there are multiple high-amplitude PFs at frequencies corresponding to LMs, they may not be attributable to separate source phenomena, as their directivities (and, by extension, convective velocities) are similar. However, whether or not this is the case remains to be seen.

For the frequency corresponding to LM I, there appears to be one dominant acoustic radiator (shown as PF 1, see Fig. 12b) that contributes primarily to the main radiation lobe. This PF has noticeably more aft-skewed directivity than most of the other frequencies shown. Additionally, PF 1 reaches its maximum level around $\tilde{L}_s$ as seen in Fig. 10a, which is more downstream than the principal PF at any other frequency shown. Given that LSN has been shown to originate farther downstream and have shallower radiation angles [11], it is possible that the dominant noise for LM I may be associated with LSN.

Local maxima II and III have radiation characteristics more in the forward direction, with their most dominant energy coming from upstream of $\tilde{L}_s$. In the case of LM II, the dominant PF has a maximum in between $\tilde{L}_c$ and $\tilde{L}_s$, with the second most energetic PF being just upstream of $\tilde{L}_c$. This could reflect radiation from fully developed turbulence in the region beyond $\tilde{L}_c$ and MWR originating from the shear layer upstream of $\tilde{L}_c$, respectively. LM III, peaking in amplitude around $\tilde{L}_c$, may be primarily associated with MWR originating from the shear layer. Other studies have suggested that MWR from the shear layer and radiation from the fully developed turbulence region beyond $\tilde{L}_c$ exhibit distinct acoustic radiation. Panda et al. [71] observed the correlation between the jet flow and the acoustic field in a laboratory-scale cold jet and found that in convectively subsonic and supersonic jets, correlation with the centerline flow peaked at 10–12 diameters downstream, while correlation with the shear layer peaked at 5–6 diameters downstream, and only for the convectively supersonic case. Viswanathan [72] showed that in convectively supersonic jets, there were two primary sources: one that existed downstream of the potential core and one that was upstream of $\tilde{L}_c$ that was related to strong MWR from the developing shear layer. Thus, we surmise that LM II and III could be related to these two distinct subsources, with the PFs suggesting that both LM II and III could have components from each of these distinct source regions. While this approach has localized potential sources to these regions and has shown that there are likely distinct acoustic sources in these flow regions, connections to distinct radiation mechanisms are strictly corollary; further work with numerical simulations that connect flow and radiated acoustic energy is necessary to prove causality, such as those by Liu et al. [11,31] and Unnikrishnan and Gaitonde [73].

E. Discussion

Connections can be made between phenomena observed here and in other experiments, both lab-scale and numerical. Schmidt et al. [14] showed, in a characterization of jet flow via LES, that structures throughout the shear layer up to L_c were characterized by K-H-type wavepackets, whereas downstream of the potential core and at lower frequencies, modes associated with Orr-type wavepackets were dominant. The Orr mechanism was found to be present in the shear layer upstream of L_c but at a much lower amplitude than the K-H mechanism. This identification of mechanisms seems to be consistent with what has been described

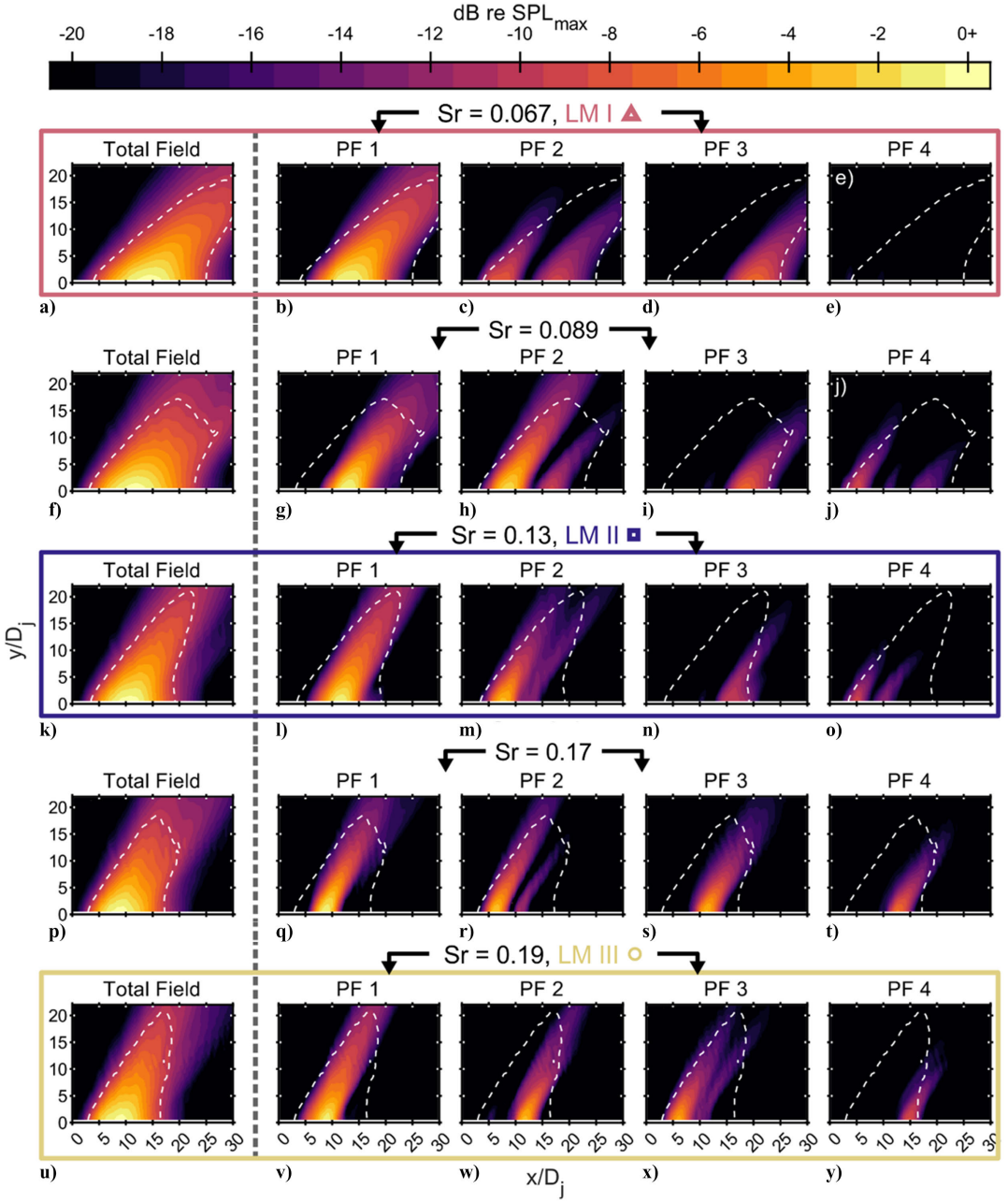

Fig. 12 Total field and first four PFs at AB on the plane $z = 0$. Dashed contours indicate −10 dB re SPL$_{max}$ of the total field. Amplitude scales consistent across each frequency.

elsewhere as the phenomena of MWR and LSN. Liu et al. [11] have shown in acoustic data from LES that MWR appears to originate from throughout the shear layer and continues downstream some distance. This MWR appears to have broadband behavior. LSN was correlated with an acoustically active region located farther downstream with a lower characteristic frequency. This localization of MWR and LSN seems consistent with observed behaviors of the K-H and Orr mechanisms. Additionally, Liu et al. [11] showed that at AB-like conditions, MWR reached a peak intensity at around $Sr = 0.2$, while below $Sr = 0.1$, LSN dominated the radiation. Comparing this with the LM observed in this paper, LM I lies at $Sr = 0.067$ at AB, while LM II and III are in a region that MWR has been suggested to dominate. This reinforces the idea that LM I may principally correspond to LSN (and, by extension, possibly the Orr mechanism), while LM II and III ($Sr = 0.13$ and 0.19) may be primarily attributable to MWR (and therefore, the K-H mechanism in the shear layer and region just after the collapse of the potential core, but before $\tilde{L}_s$). Furthermore, a far-field analysis of the same measurement used in this paper by Christian et al. [34] showed that a convective Mach number associated with the K-H mechanism was most accurate at predicting the peak overall radiation angle of the jet. Thus, given that LM II and III are the two most energetic local maxima, it is indeed likely that they are associated with the K-H mechanism.

IV. Conclusions

A coherence-based acoustic source decomposition has been performed at the maximum afterburner engine condition for an installed GE F404 engine using reconstructions obtained via acoustical holography. The application of a phase-unwrapping and interpolation method increases the bandwidth of acoustical holography applied to jet noise fields.

These analysis tools have been applied to source characterization efforts. Apparent source representations at the nozzle lipline show LMs, distinct in space and frequency, at both engine conditions. These local maxima occur further upstream with increasing frequency.

Decompositions at and between the frequency centers of the first three local maxima show lower overall numbers of PFs required for representing the field at the LM centers, while between the LMs, relatively more PFs are required. Likewise, at frequencies between the LMs, more PFs are higher in amplitude than at the LM centers. This suggests lower coherence between the LM centers, and that the field between LMs is likely a combination of the phenomena constituting each LM. It seems likely that the first LM may be caused primarily by subsonic noise radiation from large-scale turbulence structures, while higher-order LMs may correspond mainly to MWR originating from different regions of the flow—the shear layer and the region just after the collapse of the potential core but before the end of the supersonic core.

While these results are promising, significant research remains. While analyses of full-scale installed engines such as this are useful for identifying real-world acoustic phenomena, additional tools and analyses are required to directly connect and understand the relationship between flow structure and acoustic radiation phenomena. Ultimately, a proper understanding of supersonic jet noise must be fostered by a combination of complementary full-scale analyses, laboratory-scale experiments, and numerical simulations.

Acknowledgments

The authors gratefully acknowledge the Office of Naval Research for funding under grant number N00014-21-1- 2069 with project monitor Steven Martens, Code 351 Jet Noise Reduction. The measurements were funded through the Advanced Pilot Training System Program Office and the Air Force Research Laboratory. The authors also thank Alan T. Wall for his contributions to the OLVR methodology and algorithms, as well as anonymous reviewers for their thoughtful and valuable feedback. Distribution A: Approved for public release; distribution unlimited. Cleared 05/12/2023.

References

[1] Wall, A. T., Gee, K. L., James, M. M., Bradley, K. A., McInerny, S. A., and Neilsen, T. B., "Near-Field Noise Measurements of a High-Performance Military Jet Aircraft," *Noise Control Engineering Journal*, Vol. 60, No. 4, 2012, pp. 421–434. https://doi.org/10.3397/1.3701021

[2] James, M. M., Salton, A. R., Downing, J. M., Gee, K. L., Neilsen, T. B., Reichman, B. O., McKinley, R. L., Wall, A. T., and Gallagher, H. L., "Acoustic Emissions from F-35 Aircraft During Ground Run-Up," *AIAA Aviation 2015 Forum*, AIAA Paper 2015-2375, June 2015. https://doi.org/10.2514/6.2015-2375

[3] Wall, A. T., Gee, K. L., Neilsen, T. B., McKinley, R. L., and James, M. M., "Military Jet Noise Source Imaging Using Multisource Statistically Optimized Near-Field Acoustical Holography," *Journal of the Acoustical Society of America*, Vol. 139, No. 4, 2016, pp. 1938–1950. https://doi.org/10.1121/1.4945719

[4] Tam, C. K. W., Aubert, A. C., Spyropoulos, J. T., and Powers, R. W., "On the Dominant Noise Components of Tactical Aircraft: Laboratory to Full Scale," *Journal of Sound and Vibration*, Vol. 422, May 2018, pp. 92–111. https://doi.org/10.1016/j.jsv.2018.02.023

[5] Leete, K. M., Wall, A. T., Gee, K. L., Neilsen, T. B., James, M. M., and Downing, J. M., "Acoustical Holography-Based Analysis of Spatiospectral Lobes in High-Performance Aircraft Jet Noise," *AIAA Journal*, Vol. 59, No. 10, 2021, pp. 4166–4178. https://doi.org/10.2514/1.J059400

[6] Leete, K. M., Vaughn, A. B., Bassett, M. S., Rasband, R. D., Novakovich, D. J., Gee, K. L., Campbell, S. C., Mobley, F. S., and Wall, A. T., "Jet Noise Measurements of an Installed GE F404 Engine," *AIAA SciTech Forum*, AIAA Paper 2021-1638, Jan. 2021. https://doi.org/10.2514/6.2021-1638

[7] Christian, M. A., Gee, K. L., Streeter, J. B., Mathews, L. T., Wall, A. T., Johnson, J. P., and Campbell, S. C., "Installed F404 Engine Noise Source Characteristics from Far-Field Directivity Measurements," *28th AIAA/CEAS Aeroacoustics Conference*, AIAA Paper 2022-3027, June 2022. https://doi.org/10.2514/6.2022-3027

[8] Olaveson, T., Ward, J. A., Johnson, J. P., Gee, K. L., and Wall, A. T., "Analysis of Spatiospectral Lobes in Installed F404 Engine Noise Radiation," *28th AIAA/CEAS Aeroacoustics Conference*, AIAA Paper 2022-3087, June 2022. https://doi.org/10.2514/6.2022-3087

[9] Murray, N. E., Tinney, C. E., and Panickar, P., "Laboratory-Scale Afterburning Supersonic Jet Noise Reduction Using Contoured Inserts," *28th AIAA/CEAS Aeroacoustics Conference*, AIAA Paper 2022-3030, June 2022. https://doi.org/10.2514/6.2022-3030

[10] Tam, C. K. W., and Parrish, S. A., "Noise of High-Performance Aircraft at Afterburner," *Journal of Sound and Vibration*, Vol. 352, Sept. 2015, pp. 103–128. https://doi.org/10.1016/j.jsv.2015.04.010

[11] Liu, J., Corrigan, A. T., Kailasanath, K., and Taylor, B. D., "Impact of the Specific Heat Ratio on the Noise Generation in a High-Temperature Supersonic Jet," *54th AIAA Aerospace Sciences Meeting*, AIAA Paper 2016-2125, Jan. 2016. https://doi.org/10.2514/6.2016-2125

[12] Arndt, R. E. A., Long, D. F., and Glauser, M. N., "The Proper Orthogonal Decomposition of Pressure Fluctuations Surrounding a Turbulent Jet," *Journal of Fluid Mechanics*, Vol. 340, June 1997, pp. 1–33. https://doi.org/10.1017/S0022112097005089

[13] Towne, A., Schmidt, O. T., and Colonius, T., "Spectral Proper Orthogonal Decomposition and Its Relationship to Dynamic Mode Decomposition and Resolvent Analysis," *Journal of Fluid Mechanics*, Vol. 847, July 2018, pp. 821–867. https://doi.org/10.1017/jfm.2018.283

[14] Schmidt, O. T., Towne, A., Rigas, G., Colonius, T., and Brès, G. A., "Spectral Analysis of Jet Turbulence," *Journal of Fluid Mechanics*, Vol. 855, Nov. 2018, pp. 953–982. https://doi.org/10.1017/jfm.2018.675

[15] Kwon, H. S., and Bolton, J. S., "Partial Field Decomposition in Nearfield Acoustical Holography by the Use of Singular Value Decomposition and Partial Coherence Procedures," *INTER-NOISE and NOISE-CON Congress and Conference Proceedings*, NOISE-CON 98, Ypsilanti MI, April 1998, pp. 649–654.

[16] Kim, Y. J., Bolton, J. S., and Kwon, H. S., "Partial Sound Field Decomposition in Multireference Near-Field Acoustical Holography by Using Optimally Located Virtual References," *Journal of the Acoustical Society of America*, Vol. 115, No. 4, 2004, pp. 1641–1652. https://doi.org/10.1121/1.1642627

[17] Wall, A. T., Gee, K. L., Leete, K. M., Nielsen, T. B., Stout, T. A., and James, M. M., "Partial-Field Decomposition Analysis of Full-Scale Supersonic Jet Noise Using Optimized-Location Virtual References," *Journal of the Acoustical Society of America*, Vol. 144, No. 3, 2018, pp. 1356–1367. https://doi.org/10.1121/1.5053580

[18] Long, D. F., "Jet Noise Source Location via Acoustic Holography and Shadowgraph Imagery," *14th AIAA/CEAS Aeroacoustics Conference (29th AIAA Aeroacoustics Conference)*, AIAA Paper 2008-2888, May 2008. https://doi.org/10.2514/6.2008-2888

[19] Vold, H., Shah, P. N., Davis, J., Bremmer, P. G., McLaughlin, D., Morris, P., Veltin, J., and McKinley, R., "High Resolution Continuous Scan Acoustical Holography Applied to High-Speed Jet Noise," *16th AIAA/CEAS Aeroacoustics Conference*, AIAA Paper 2010-3754, June 2010. https://doi.org/10.2514/6.2010-3754

[20] Neilsen, T. B., Gee, K. L., Wall, A. T., and James, M. M., "Similarity Spectra Analysis of High-Performance Jet Aircraft Noise," *Journal of the Acoustical Society of America*, Vol. 133, No. 4, 2013, pp. 2116–2125. https://doi.org/10.1121/1.4792360

[21] Neilsen, T. B., Vaughn, A. B., Gee, K. L., Swift, S. H., Wall, A. T., Downing, J. M., and James, M. M., "Three-Way Spectral Decompositions of High-Performance Military Aircraft Noise," *AIAA Journal*, Vol. 57, No. 8, 2019, pp. 3467–3479. https://doi.org/10.2514/1.J057992

[22] Tam, C. K. W., "Supersonic Jet Noise," *Annual Review of Fluid Mechanics*, Vol. 27, No. 1, 1995, pp. 17–43. https://doi.org/10.1146/annurev.fl.27.010195.000313

[23] Tam, C. K. W., Golebiowski, M., and Seiner, J. M., "On the Two Components of Turbulent Mixing Noise from Supersonic Jets," *2nd AIAA/CEAS Aeroacoustics Conference*, AIAA Paper 1996-1716, May 1996. https://doi.org/10.2514/6.1996-1716

[24] Tam, C. K. W., Viswanathan, K., Ahuja, K. K., and Panda, J., "The Sources of Jet Noise: Experimental Evidence," *Journal of Fluid Mechanics*, Vol. 615, Nov. 2008, pp. 253–292. https://doi.org/10.1017/S0022112008003704

[25] Tam, C. K. W., "Mach Wave Radiation from High-Speed Jets," *AIAA Journal*, Vol. 47, No. 10, 2009, pp. 2440–2448. https://doi.org/10.2514/1.42644

[26] Viswanathan, K., "Aeroacoustics of Hot Jets," *Journal of Fluid Mechanics*, Vol. 516, Oct. 2004, pp. 39–82. https://doi.org/10.1017/S0022112004000151

[27] Schlinker, R. H., Liljenberg, S. A., Polak, D. R., Post, K. A., Chipman, C. T., and Stern, A. M., "Supersonic Jet Noise Characteristics & Propagation: Engine and Model Scale," *13th AIAA/CEAS Aeroacoustics Conference (28th AIAA Aeroacoustics Conference)*, AIAA Paper 2007-3623, May 2007. https://doi.org/10.2514/6.2007-3623

[28] Epps, K. A., Merrill, C. D., Vaughn, A. B., Leete, K. M., Gee, K. L., and Wall, A. T., "Preliminary Similarity Spectra Analysis of Noise from a High-Performance Trainer Aircraft," *Proceedings of Meetings on Acoustics*, Vol. 42, No. 1, 2020, Paper 040006. https://doi.org/10.1121/2.0001623

[29] Prasad, C., and Morris, P. J., "Steady Active Control of Noise Radiation from Highly Heated Supersonic Jets," *Journal of the Acoustical Society of America*, Vol. 149, No. 2, 2021, pp. 1306–1317. https://doi.org/10.1121/10.0003570

[30] Jordan, P., and Colonius, T., "Wave Packets and Turbulent Jet Noise," *Annual Review of Fluid Mechanics*, Vol. 45, Jan. 2013, pp. 173–195. https://doi.org/10.1146/annurev-fluid-011212-140756

[31] Liu, J., and Ramamurti, R., "Numerical Study of Supersonic Jet Noise Emanating from an F404 Nozzle at Model Scale," *AIAA SciTech 2019 Forum*, AIAA Paper 2019-0807, Jan. 2019. https://doi.org/10.2514/6.2019-0807

[32] Ennix, K. A., Burcham, F. W., and Webb, L. D., "Flight-Determined Engine Exhaust Characteristics of an F404 Engine in an F-18 Airplane," *29th Joint Propulsion Conference and Exhibit*, AIAA Paper 1993-2543. See also NASA TM-4538, June 1993. https://doi.org/10.2514/6.1993-2543

[33] Seiner, J. M., Ukeiley, L. S., and Jansen, B. J., "Aero-Performance Efficient Noise Reduction for the F404-400 Engine," *11th AIAA/CEAS Aeroacoustics Conference*, AIAA Paper 2005-3048, May 2005. https://doi.org/10.2514/6.2005-3048

[34] Christian, M. A., and Gee, K. L., "Connecting the Convective Mach Number to Full-Scale Supersonic Jet Noise Directivity," *AIAA Aviation 2023 Forum*, AIAA Paper 2023-3351, June 2023. https://doi.org/10.2514/6.2023-3351

[35] Goates, C. B., Harker, B. M., Neilsen, T. B., and Gee, K. L., "Extending the Bandwidth of an Acoustic Beamforming Array Using Phase Unwrapping and Array Interpolation," *Journal of the Acoustical Society of America*, Vol. 141, No. 4, 2017, Paper EL407. https://doi.org/10.1121/1.4981235

[36] Harker, B. M., Gee, K. L., Neilsen, T. B., Wall, A. T., and James, M. M., "Source Characterization of Full-Scale Tactical Jet Noise from Phased-Array Measurements," *Journal of the Acoustical Society of America*, Vol. 146, No. 1, 2019, pp. 665–680. https://doi.org/10.1121/1.5118239

[37] Cook, M. R., Gee, K. L., Sommerfeldt, S. D., and Neilsen, T. B., "Coherence-Based Phase Unwrapping for Broadband Acoustic Signals," *Proceedings of Meetings on Acoustics*, Vol. 30, No. 2, 2017, Paper 055005. https://doi.org/10.1121/2.0000611

[38] Shah, P. N., Vold, H., and Yang, M., "Reconstruction of Far-Field Noise Using Multireference Acoustical Holography Measurements of High-Speed Jets," *17th AIAA/CEAS Aeroacoustics Conference (32nd AIAA Aeroacoustics Conference)*, AIAA Paper 2011-2772, June 2011. https://doi.org/10.2514/6.2011-2772

[39] Lee, M., and Bolton, J. S., "Source Characterization of a Subsonic Jet by Using Near-Field Acoustical Holography," *Journal of the Acoustical Society of America*, Vol. 121, No. 2, 2007, pp. 967–977. https://doi.org/10.1121/1.2404626

[40] Long, D., Peters, J., and Anderson, M., "Evaluating Turbofan Exhaust Noise and Source Characteristics from Near Field Measurements," *15th AIAA/CEAS Aeroacoustics Conference (30th AIAA Aeroacoustics Conference)*, AIAA Paper 2009-3214, May 2009. https://doi.org/10.2514/6.2009-3214

[41] Wall, A. T., Gee, K. L., and Neilsen, T. B., "Multisource Statistically Optimized Near-Field Acoustical Holography," *Journal of the Acoustical Society of America*, Vol. 137, No. 2, 2015, pp. 963–975. https://doi.org/10.1121/1.4906585

[42] Hald, J., "Basic Theory and Properties of Statistically Optimized Near-Field Acoustical Holography," *Journal of the Acoustical Society of America*, Vol. 125, No. 4, 2009, pp. 2105–2120. https://doi.org/10.1121/1.3079773

[43] Williams, E. G., "Continuation of Acoustic Near-Fields," *Journal of the Acoustical Society of America*, Vol. 113, No. 13, 2003, pp. 1273–1281. https://doi.org/10.1121/1.1528173

[44] Leete, K. M., Wall, A. T., Gee, K. L., Neilsen, T. B., Harker, B. M., and James, M. M., "Azimuthal Coherence of the Sound Field in the Vicinity of a High Performance Military Aircraft," *Proceedings of Meetings on Acoustics*, Vol. 29, No. 1, 2016, Paper 045007. https://doi.org/10.1121/2.0000673

[45] Steiner, R., and Hald, J., "Near-Field Acoustical Holography Without the Errors and Limitations Caused by the Use of Spatial DFT," *International Journal of Acoustics and Vibration*, Vol. 6, No. 2, 2001, pp. 83–89. https://doi.org/10.20855/ijav.2001.6.278

[46] Williams, E. G., "Regularization Methods for Near-Field Acoustical Holography," *Journal of the Acoustical Society of America*, Vol. 110, No. 4, 2001, pp. 1976–1988. https://doi.org/10.1121/1.1404381

[47] Stout, T. A., Wall, A. T., Gee, K. L., and Neilsen, T. B., "Obtaining Acoustic Intensity from Multisource Statistically Optimized Near-Field Acoustical Holography," *Proceedings of Meetings on Acoustics*, Vol. 33, No. 1, 2018, Paper 055002. https://doi.org/10.1121/2.0000835

[48] Schmidt, R. O., "A Signal Subspace Approach to Multiple Emitter Location and Spectral Estimation," Ph.D. Dissertation, Stanford Univ., Stanford, CA, Nov. 1981.

[49] Schmidt, R. O., "Multiple Emitter Location and Signal Parameter Estimation," *RADC Spectrum Estimation Workshop*, Oct. 1979, Griffiss Air Force Base, NY. Reproduced as: Schmidt, R. O., "Multiple Emitter Location and Signal Parameter Estimation," *IEEE Transactions on Antennas and Propagation*, Vol. 34, No. 3, 1986, pp. 276–280. https://doi.org/10.1109/TAP.1986.1143830

[50] Johnson, D. H., and Dudgeon, D. E., *Array Signal Processing: Concepts and Techniques*, Prentice-Hall, Englewood Cliffs, NJ, 1993, pp. 382–385.

[51] Bendat, J. S., "Modern Analysis Procedures for Multiple Input/Output Problems," *Journal of the Acoustical Society of America*, Vol. 68, No. S1, 1980, pp. 498–503. https://doi.org/10.1121/1.384760

[52] Eldred, K. M., "Acoustic Loads Generated by the Propulsion System," NASA SP-8072, 1971.

[53] Lubert, C. P., Gee, K. L., and Tsutsumi, S., "Supersonic Jet Noise from Launch Vehicles: 50 Years Since NASA SP-8072," *Journal of the Acoustical Society of America*, Vol. 151, No. 2, 2022, pp. 752–791. https://doi.org/10.1121/10.0009160

[54] Olaveson, T. W., Gee, K. L., and Johnson, J. P., "Wavelet-Based Analysis of Spectral and Temporal Structures in F404 Engine Jet Noise," *AIAA Aviation 2023 Forum*, AIAA Paper 2023-3213, June 2023. https://doi.org/10.2514/6.2023-3213

[55] Swift, S. H., Gee, K. L., Neilsen, T. B., Wall, A. T., Downing, J. M., and James, M. M., "Spatiotemporal Correlation Analysis of Jet Noise from a Round-Nozzle Supersonic Aircraft," *2018 AIAA/CEAS Aeroacoustics Conference*, AIAA Paper 2018-3938, June 2018. https://doi.org/10.2514/6.2018-3938

[56] Mathews, L. T., Gee, K. L., Leete, K. M., and Wall, A. T., "Acoustic Source Characterization of an Installed GE F404 Engine Using Near-Field Acoustical Holography," *28th AIAA/CEAS Aeroacoustics Conference*, AIAA Paper 2022-3028, June 2022. https://doi.org/10.2514/6.2022-3028

[57] Mathews, L. T., Gee, K. L., and Wall, A. T., "Coherence-Based Acoustic Source Decomposition of Installed GE F404 Engine Noise," *AIAA Aviation 2023 Forum*, AIAA Paper 2023-3212, June 2023. https://doi.org/10.2514/6.2023-3212

[58] Leete, K. M., Gee, K. L., Liu, J., and Wall, A. T., "Coherence Analysis of the Noise from a Simulated Highly Heated Laboratory-Scale Jet," *AIAA Journal*, Vol. 58, No. 8, 2020, pp. 3426–3435. https://doi.org/10.2514/1.J059112

[59] Liu, J., Corrigan, A. T., Kailasanath, K., and Gutmark, E. J., "Impact of Chevrons on Noise Source Characteristics in Imperfectly Expanded Jet Flows," *21st AIAA/CEAS Aeroacoustics Conference*, AIAA Paper 2015-2835, June 2015. https://doi.org/10.2514/6.2015-2835

[60] Liu, J., Kailasanath, K., and Gutmark, E. J., "Similarity Spectra Analysis in Highly Heated Supersonic Jets Using Large-Eddy Simulations," *55th AIAA Aerospace Sciences Meeting*, AIAA Paper 2017-0926, Jan. 2017. https://doi.org/10.2514/6.2017-0926

[61] Nagamatsu, H. T., Sheer, R. E., and Horvay, G., "Supersonic Jet Noise Theory and Experiments," Basic Aerodynamic Noise Research, NASA SP-207, 1969.

[62] Nagamatsu, H. T., and Horvay, G., "Supersonic Jet Noise," *8th Aerospace Sciences Meeting*, AIAA Paper 1970-0237, Jan. 1970. https://doi.org/10.2514/6.1970-237

[63] Gee, K. L., "A Tale of Two Curves and Their Influence on Rocket and Supersonic Jet Noise Research," *Journal of the Acoustical Society of America*, Vol. 149, No. 4, 2021, pp. 2159–2162. https://doi.org/10.1121/10.0003938

[64] Baars, W. J., Murray, N. E., and Tinney, C. E., "A Proper Framework for Studying Noise from Jets with Non-Compact Sources," *Journal of Fluid Mechanics*, Vol. 929, Dec. 2021, Paper A23. https://doi.org/10.1017/jfm.2021.837

[65] Harker, B. M., Gee, K. L., Neilsen, T. B., Wall, A. T., and James, M. M., "Beamforming-Based Wavepacket Model for Noise Environment Predictions of Tactical Aircraft," *23rd AIAA/CEAS Aeroacoustics Conference*, AIAA Paper 2017-4048, June 2017. https://doi.org/10.2514/6.2017-4048

[66] Wall, A. T., Gardner, M. D., Gee, K. L, and Neilsen, T. B., "Coherence Length as a Figure of Merit in Multireference Near-Field Acoustical Holography," *JASA Express Letters*, Vol. 132, No. 3, 2012, Paper EL215. https://doi.org/10.1121/1.4740518

[67] Olaveson, T., Harker, B. M., and Gee, K. L., "Beamforming-Based Wavepacket Model for Noise Predictions of Tactical Aircraft," *Proceedings of Meetings on Acoustics*, Vol. 29, No. 1, 2016, Paper 040011. https://doi.org/10.1121/2.0001639

[68] Papamoschou, D., "Wavepacket Modeling of the Jet Noise Source," *17th AIAA/CEAS Aeroacoustics Conference (32nd AIAA Aeroacoustics Conference)*, AIAA Paper 2011-2835, June 2011. https://doi.org/10.2514/6.2011-2835

[69] Harker, B. M., Neilsen, T. B., Gee, K. L., Wall, A. T., and James, M. M., "Spatiotemporal Correlation Analysis of Jet Noise from a High-Performance Military Aircraft," *AIAA Journal*, Vol. 54, No. 5, 2016, pp. 1554–1566. https://doi.org/10.2514/1.J054442

[70] Wall, A. T., Gee, K. L., Neilsen, T. B., Harker, B. M., McInerny, S. A., McKinley, R. L., and James, M. M., "Investigation of Multi-Lobed Fighter Jet Noise Sources Using Acoustical Holography and Partial Field Decomposition Methods," *21st AIAA/CEAS Aeroacoustics Conference*, AIAA Paper 2015-2379, June 2015. https://doi.org/10.2514/6.2015-2379

[71] Panda, J., Seasholtz, R. G., and Elam, K. A., "Investigation of Noise Sources in High-Speed Jets via Correlation Measurements," *Journal of Fluid Mechanics*, Vol. 537, Aug. 2005, pp. 349–385. https://doi.org/10.1017/S0022112005005148

[72] Viswanathan, K., "Investigation of the Sources of Jet Noise," *13th AIAA/CEAS Aeroacoustics Conference (28th AIAA Aeroacoustics Conference)*, AIAA Paper 2007-3601, May 2007. https://doi.org/10.2514/6.2007-3601

[73] Unnikrishnan, S., and Gaitonde, D. V., "A Pressure Decomposition Framework for Aeroacoustic Analysis of Turbulent Jets," *European Journal of Mechanics/B Fluids*, Vol. 81, May 2018, pp. 41–61. https://doi.org/10.1016/j.euromechflu.2020.01.006

C. Bailly
Associate Editor

Chapter 3

On Broadband Shock-Associated Noise Source and Radiation Characteristics from an Installed, Afterburning GE F404 Engine

Broadband shock-associated noise (BSN) is a major source of high-frequency noise in imperfectly expanded supersonic jet aircraft. While BSN has been extensively studied, source characterization from full-scale engines remains limited. This paper investigates BSN source and radiation characteristics from a full-scale, installed GE F404 engine on the T-7A trainer aircraft using the same acoustical holography processing as Chapter 2, but applied to a different region of the source and in a higher-frequency regime where BSN becomes dominant and does not include the OLVR decomposition technique used in Chapter 2. This chapter is an article published as L. T. Mathews and K. L. Gee, "On Broadband Shock-Associated Noise Source and Radiation Characteristics from an Installed, Afterburning GE F404 Engine," *AIAA SciTech Forum,* 2025. It is reprinted in this dissertation under the terms of AIAA's Rights and Permissions with the permission of the copyright holders, L. T. Mathews and K. L. Gee. I hereby confirm that the use of this article is compliant with all publishing agreements.

AIAA Aviation Forum and ASCEND co-located Conference Proceedings
21 - 25 July 2025, Las Vegas, Nevada
AIAA AVIATION FORUM AND ASCEND 2025

10.2514/6.2025-3008

On Broadband Shock-Associated Noise Source and Radiation Characteristics from an Installed, Afterburning GE F404 Engine*

Logan T. Mathews† and Kent L. Gee‡

Brigham Young University, Provo, UT, 84604, United States

Broadband shock-associated noise (BSN) is a major source of high-frequency noise in imperfectly expanded supersonic jets. While BSN has been extensively studied, source characterization from full-scale engines remains limited. This paper investigates BSN source and radiation characteristics from a full-scale, installed GE F404 engine on the T-7A trainer aircraft using acoustic holography. Apparent BSN sources are identified along the nozzle lipline and corroborated with in-situ imaging. The observed shock spacing aligns with similar jets in the literature but deviates significantly from traditional analytical models. Likewise, BSN peak frequencies at forward angles match trends from other full-scale jets but differ from simulations and lab-scale data, likely due to temperature and scale-related differences. A widely used BSN frequency model underperforms when relying on historical analytic shock spacing predictions but yields excellent agreement when corrected with measured spacing. Coherence analysis reveals connections between upstream-directed BSN and downstream Mach wave radiation, and shows elevated coherence between shock cells, indicating a partially coherent, distributed BSN source.

Nomenclature

A	=	nozzle area, m^2
β_C	=	convergent nozzle off-design parameter equal to $\sqrt{M_j^2 - 1}$
β	=	generalized off-design parameter equal to $\sqrt{\lvert M_j^2 - M_D^2 \rvert}$
D	=	nozzle, meters
f	=	frequency, Hz
γ	=	ratio of specific heats
L_n	=	nth shock cell spacing, measured as the distance between shock cell tips, meters
$\bar{L}$	=	average shock cell spacing/characteristic shock wavelength, meters
$\bar{L}_{\text{meas}}$	=	average shock cell spacing from acoustical measurements, meters
M	=	Mach number
NPR	=	nozzle pressure ratio, defined as the ratio of the chamber pressure to the ambient pressure.
Sr	=	Strouhal number, defined as fD_j/U_j
TTR	=	total temperature ratio, defined as the ratio of the inlet total temperature to the exit total temperature.
x	=	downstream distance from nozzle exit, meters
y	=	sideline distance from jet centerline, meters

* Distribution A: Approved for public release; distribution unlimited.
† PhD Candidate, Department of Physics and Astronomy, AIAA student member.
‡ Professor, Department of Physics and Astronomy, AIAA Associate Fellow

Subscripts

a	=	ambient condition
c	=	relating to the convection (advection) of turbulence, wavepackets in the flow
conv	=	relating to a convergent nozzle
C-D	=	relating to a convergent-divergent nozzle
d	=	jet design condition
e	=	exit jet condition
j	=	fully-expanded jet condition
t	=	throat jet condition

I. Introduction

IN an imperfectly expanded supersonic jet, the mismatch between the nozzle exit pressure and ambient pressure gives rise to a series of oblique shocks and expansion fans. This structure forms a train of shock cells, commonly referred to as "Mach diamonds," which appear in the jet's potential core, as shown in Fig. 1. These shock structures interact with turbulent wavepacket-like structures in the shear layer, giving rise to two types of shock-associated noise [1]. The first type, known as screech, arises from a feedback loop between flow perturbations and the shock structure, resulting in discrete tonal components in the radiated sound [1-3]. Screech is most prominent in laboratory-scale and transonic jets, but has not been consistently observed in full-scale tactical aircraft engines[4]. The second type is broadband shock-associated noise (BBSAN or BSN), which has a broadband spectral character and typically radiates in the forward direction at frequencies higher than the dominant mixing noise.

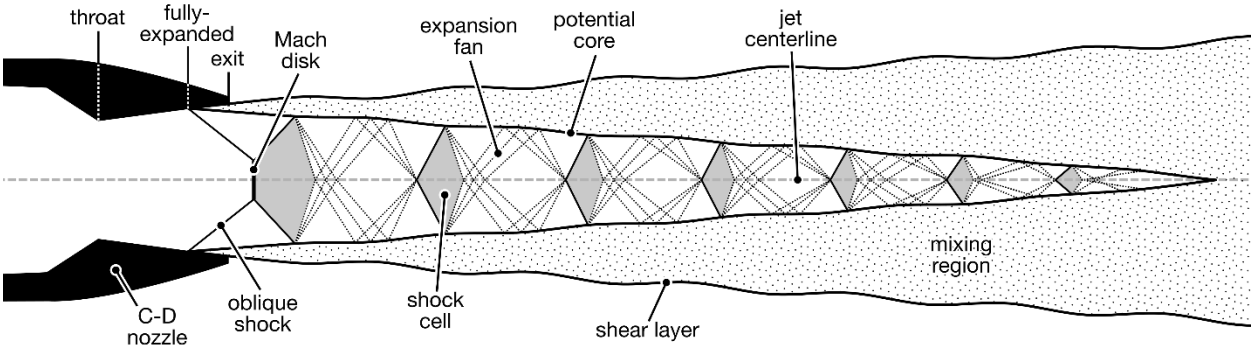

Figure 1. Schematic of shock structure in a supersonic, overexpanded jet.

The foundational study of BSN was conducted by Harper-Bourne and Fisher[1], who introduced a model for BSN in sonic jets from convergent nozzles. Their work, along with subsequent studies by Tanna[5] and Howe and Ffowcs-Williams[6], expanded the theoretical and experimental understanding of BSN from convergent nozzles. Further investigations extended this research to convergent-divergent (C-D) supersonic jets, notably by Seiner and Norum[4], Norum and Seiner[7,8], Pao and Seiner[9], and Seiner and Yu[10]. Important theoretical developments by Tam and Tanna[11], Tam et al. [12], and Tam[13] provided predictive models for BSN spectra and shock-cell structure. More recent studies—including experimental, numerical, and theoretical approaches—have broadened the scope of BSN research and increasingly connected fluid dynamic and acoustic domains [14-25].

Despite this progress, the direct characterization of BSN sources in full-scale, afterburning-capable engines remains limited, primarily due to the difficulty of capturing detailed in-situ flow measurements alongside acoustic data. These studies have primarily focused on acoustic characteristics radiated to the field [26,27,28]. Because of the constraints of full-scale measurements, most BSN studies have relied on unheated or mildly heated laboratory-scale jets or numerical simulations. While advances in computational modeling [29-32] and afterburning jet facilities [33,34] have improved understanding of highly heated jet acoustics, these approaches still require further validation against full-scale engine behavior.

This paper presents the most detailed source characterization of BSN in a full-scale, afterburning-capable jet engine to date. The apparent spatial characteristics of BSN sources are compared with in-situ photographs, and the apparent spacing of the noise sources and associated shock cells are compared with other models and data present in the literature. The peak frequency of the measured BSN as a function of radiation angle is compared to both analytical

models and data from other full-scale measurements. A coherence analysis is conducted of the radiated BSN, and coherence is found between upstream and downstream radiated noise from each apparent shock noise source, which suggests that upstream-radiated BSN may influence or couple with downstream-radiating mixing noise.

II. Methods

A. Measurement and Data

The data in this paper were obtained through an extensive acoustical measurement of the T-7A trainer aircraft in August 2019 at Holloman Air Force Base in New Mexico, USA. Additional details of this measurement campaign are given by Leete et al.[35]. This analysis uses a 120-element quasi-linear ground microphone array of ¼" GRAS 46BD and 46BG pressure microphones located near the aircraft, depicted in Fig. 2. For context, the microphone array was located at its closest approximately 9 diameters from the centerline of the jet, and the peak BSN at the array was approximately 800-900 Hz, which translates to the closest microphones being in excess of 10 acoustic wavelengths away at these frequencies. The aircraft was run up through several engine conditions six times. This analysis uses the acoustic data averaged across the six engine runs at the maximum afterburner (AB) engine condition.

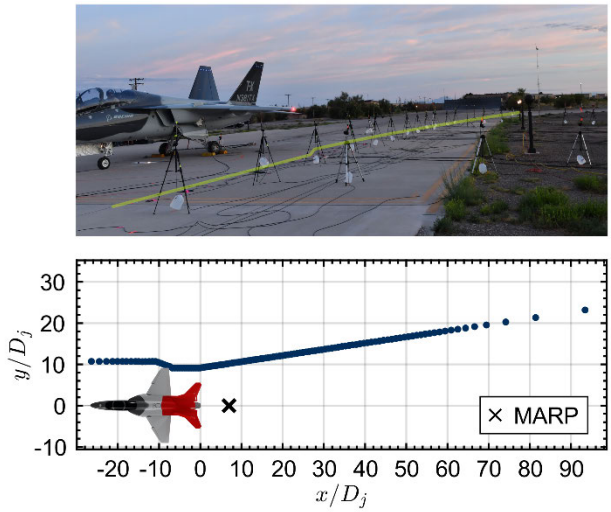

Figure 2. a) Photograph of aircraft as positioned during the measurement, microphone array highlighted in yellow. b) Schematic of microphone array, inlet angle shown.

Several key jet parameters for the T-7A at AB are reported in Table 1. These parameters were obtained through running a numerical propulsion system simulation code based on the ambient conditions of the test and input data from the engine during the run-ups. The jet was operating in an overexpanded condition at AB.

Table 1. Engine parameters at AB engine condition.

Parameter	Value
M_j	1.46
M_d	1.55
β_{conv}	1.07
β	0.52

NPR	3.3
TTR	7.0

The design Mach number (M_d) for the nozzle is calculated from the transcendental quasi-1D area Mach number relation

$$\frac{A_e}{A_t} = \frac{1}{M_d}\left[\frac{2}{\gamma+1}\left(1+\frac{\gamma-1}{2}M_d^2\right)\right]^{\frac{\gamma+1}{2(\gamma-1)}}, \tag{1}$$

where A_e is the exit area of the nozzle, $A_t = A^*$ is the throat (critical) area of the nozzle, and γ is the ratio of specific heats[36].

The parameter β used in connection with BSN is an application of the Prandtl-Glauert factor. In the context of jet nozzle operation, it is often referred to as the off-design parameter and quantifies the degree to which a jet is operating off-condition. This parameter was first introduced in the jet noise literature by Harper-Bourne and Fisher[1] in the context of convergent nozzles and is defined as

$$\beta_{conv} = \sqrt{M_j^2 - 1}, \tag{2}$$

where M_j is the fully-expanded Mach number of the jet. Though initially used for only convergent nozzles (hence the subscript conv used here for convenience), several subsequent studies used β_{conv} in their analysis of jets from both convergent and C-D nozzles (e.g. Refs. [4,7-10]). Hence, even though this parameter is not appropriate for the T-7A/F404, it is included here to compare with some of the historic literature that used it for C-D nozzles.

Tam and Tanna[11] introduced a slightly different, generalized formulation for β in the case of a C-D nozzle to achieve the same BSN intensity scaling of $I_{\text{BSN}} \propto \beta^4$, which is given as

$$\beta = \sqrt{\left|M_j^2 - M_d^2\right|}, \tag{3}$$

where M_d is the design Mach number of the nozzle. In the case of a convergent, choked nozzle, $M_d = 1$, hence the expression reduces to the same form as β_{conv}. Due to inconsistencies in the literature regarding the use of β and β_{conv} —particularly with several studies using β_{conv} to characterize C-D nozzles in supersonic flow—both parameters are reported here to facilitate comparison across the full range of existing research.

B. Acoustical Holography

This paper leverages an acoustical holography-based analysis technique to reconstruct the acoustic field using the array microphone. This technique is discussed in mathematical detail in the context of this dataset by Mathews and Gee[37]. Other discussions of the holography method used are given in several papers[38,39]. The methods used in this paper are identical to those used in Ref. [37]. For the purposes of the discussion, a brief qualitative summary of the process is given here to orient the reader to the overall methodology of the process.

The statistically optimized near-field acoustical holography process begins with transforming the raw recorded pressure data from each array microphone into the frequency domain through traditional autospectral and cross-spectral methods for noise. This results in a cross-spectral matrix at each frequency bin that contains both the magnitude and phase relationships between each microphone pair in the array. Given the partially coherent nature of jet noise, the spectral data from each frequency are then decomposed into individual partial fields using singular value decomposition, resulting in separate, self-coherent partial fields that can each have acoustical holography performed on them. Then, for each partial field at each frequency analyzed, the holographic algorithm is conducted: firstly, a numerical routine is employed to extend the aperture of the array and taper the ends of the array to zero amplitude to both prevent wraparound error, and to prevent errors from discontinuities present when the edges of the array are nonzero (similar in principle to the windowing required in Fourier analysis of noise). Then, a matrix of wavefunctions, referred to as an equivalent wave model (EWM), is constructed that contains analytic functions that form a basis for the acoustic field in a suitable geometry for the source in question. In the case of a jet, cylindrical wavefunctions are chosen and have been shown to be an appropriate choice [40]. Now, given the EWM and the measured pressures for the partial field at hand, a linear equation is formulated and the coefficients of the EWM are determined via a regularized pseudo-inverse, resulting in either a least-squares or minimum norm solution of coefficients, depending on the choice of dimensions for the EWM. In the case of this study, the system was set up to be underdetermined, and a minimum norm solution was sought. Finally, another similar matrix of wavefunctions is formulated, though the geometry of points to reconstruct can now be used in the wavefunctions, and the reconstructed field is estimated through the simple multiplications of the reconstruction EWM with the determined coefficients. Since each of the partial fields has its own EWM, the total result at each frequency is obtained by energetically summing the reconstructed partial fields.

III. Analysis

A. Lipline Acoustic Reconstruction

To investigate the source characteristics of shock-associated noise, acoustic holography is employed to reconstruct the noise field along the nozzle lipline—an effective proxy for shock noise source locations. Because this reconstruction is based only on acoustic signals that reach the microphone array, it excludes near-field energy and hydrodynamic components. Therefore, the result represents only the portion of the acoustic field that successfully propagates to the array.

Figure 3 presents the reconstructed sound field along the nozzle lipline, shown as a function of downstream distance from the nozzle exit and frequency, expressed as the Strouhal number $\mathrm{Sr} = fD_j/U_j$. Amplitude is color-mapped relative to the maximum value. A vertical white dashed line shows the estimated location of the potential core terminus. Below $\mathrm{Sr} \approx 0.35$, the field is dominated by mixing noise, with at least three distinct local maxima. These features are discussed in detail by Mathews and Gee [37]. Above this threshold, however, vertical striations appear, continuing up to the upper frequency limit of the reconstruction at $\mathrm{Sr} = 0.5$, highlighting their broadband character. Similar striations have been observed in both laboratory- and full-scale reconstructions [41,42], though with limited interpretation. In the present study, these features are further examined both spatially and spectrally, and evidence is presented linking them directly to shock noise sources.

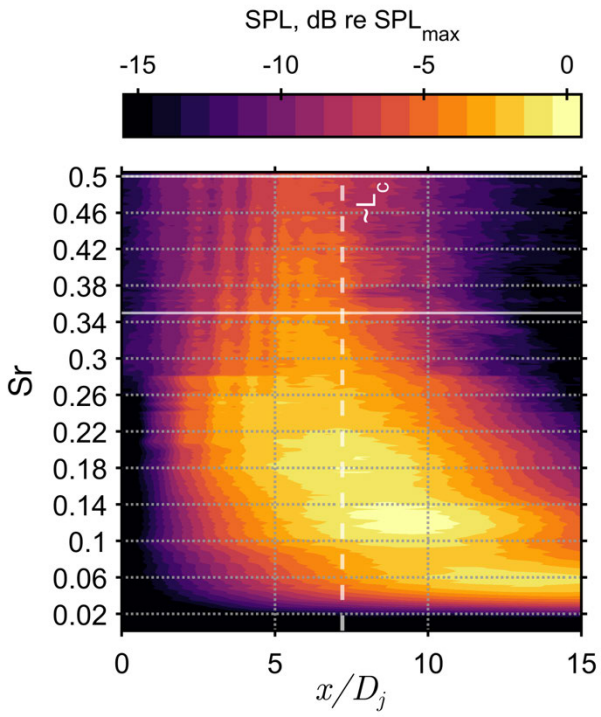

Figure 3. Spatiospectral acoustical holography reconstruction at the nozzle lipline. The estimated end of the potential core is indicated.

Since the shock noise sources are most prominent in the $0.35 \leq \mathrm{Sr} \leq 0.5$ region, and most of the mixing noise energy is below this band, this frequency band is selected as the analysis region for shock noise analyses in this paper. This region of analysis is indicated by the two horizontal white lines in Fig. 3.

To analyze the spatial characteristics of the noise sources, the reconstruction amplitude is integrated across this selected frequency range. The resulting spatial distribution is shown in Fig. 4. To reinforce the link between the observed acoustic sources and the shock cell structure, a scaled in-situ photograph of the jet is provided alongside the integrated acoustic reconstruction. Peaks in the reconstructed acoustic signature align with visible shock cell locations in the photograph, supporting the assertion that these noise sources are associated with shock-turbulence interactions.

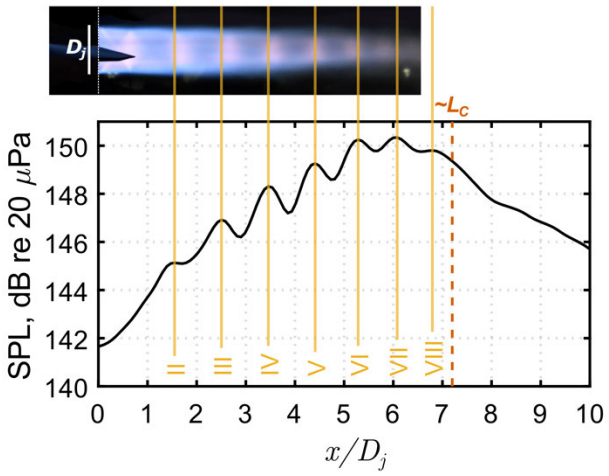

Figure 4. Integrated SPL from lipline holography reconstruction between $0.35 \leq \mathrm{Sr} \leq 0.5$ and comparison with in-situ scaled photograph of the jet at afterburner. Locations of suspected shock noise sources are indicated.

Remarkably, the first shock cell (I) does not correspond to a significant acoustic source in the reconstruction. This could indicate either a limitation in the measurement and reconstruction process or that the first shock cell radiates minimal acoustic energy. Harper-Bourne[43], using an acoustic mirror technique in a laboratory-scale jet, reported a similarly weak signature for the first shock cell. This may be attributed to the underdeveloped turbulence present near the nozzle exit upstream of the potential core terminus, which can be visually confirmed in many images of supersonic jets. The early work of Nagamatsu et al.[44] showed that sound power production in supersonic jets grows linearly downstream of the nozzle through the potential core region with very little sound power output in the first few jet diameters, and hence it would follow that less BSN would be radiated from the first few shocks. Interestingly, the amplitude of apparent BSN source locations in Fig. 4 grows roughly linearly through location VI, perhaps reflective of a linear increase in sound power output.

As shown in Fig. 4, the strongest acoustic signatures occur at shock locations VI and VII. This finding is consistent with results from Podboy et al.[45], who also observed that downstream shock cells produced the highest amplitude shock-associated noise.

These results reinforce the conclusion that radiated BSN in supersonic jets originates from discrete locations correlated with the shock cell structure, especially in the downstream portion of the potential core. The absence of strong radiation from the first shock cell suggests a dependence on turbulence development, highlighting the relationship between flow evolution and acoustic radiation. Overall, the holography analysis confirms that acoustically significant shock-turbulence interactions are spatially organized and spectrally broadband.

B. Shock Spacing

Shock spacing in imperfectly expanded jets has long been studied due to its relevance to jet noise. The spacing between shocks has traditionally been linked to the peak frequency of the radiated noise and is often referred to as the "characteristic wavelength" of BSN. Several models have been proposed for this spacing, denoted as $\bar{L}$. One of the earliest analytical models is attributed to Pack [46], in what has come to be known as the Prandtl-Pack formula, given by

$$\frac{\bar{L}}{D_j} = \frac{\pi}{\mu_1}\sqrt{M_j^2 - 1} = 1.306\,\beta_{conv} \tag{4}$$

where $\mu_1$is the first root of the zeroth-order Bessel function of the first kind ($J_0(\mu_1) = 0$). This formula does not account for energy losses and is generally applicable only to the first shock, where such losses are minimal. To account for shock spacing reductions due to losses, Harper-Bourne and Fisher[1] introduced an empirical correction:

$$\frac{\bar{L}_n}{D_j} = 1.306\,\beta_{conv}\,[1-(n-1)\epsilon], \tag{5}$$

where $\epsilon \approx 0.06$ is an empirical constant derived from experimental observations. Note that in the case of the first shock's spacing, Eq. (5) reduces simply to Eq. (4).

While this model was originally developed for convergent nozzles, it could potentially be generalized to use with C-D nozzles by substituting β for β_{conv}, leading to the expression

$$\frac{\bar{L}}{D_j} = \frac{\pi}{\mu_1}\beta = \sqrt{\left|M_j^2 - M_d^2\right|} = 1.306\,\beta. \tag{6}$$

Figure 5 compares the inter-shock spacing estimated from the acoustical holography reconstruction with predictions from Eqs. (4–6) and measurements from other experimental and simulated jets. This includes overexpanded jet data from Norum and Seiner [8] and Podboy et al. [45], as well as LES results from Liu et al. for an underexpanded TTR = 7 jet [29] and an overexpanded TTR = 2.9 jet [30]. Notably, the latter jet closely matches the T-7A conditions, aside from the TTR. The spacing between shocks IV–VIII in that case shows excellent agreement with the acoustic estimates in this study. Given that the downstream shocks were identified as the most acoustically active, the best accuracy for acoustic identification of shock locations is expected here due to their higher signal-to-noise ratio.

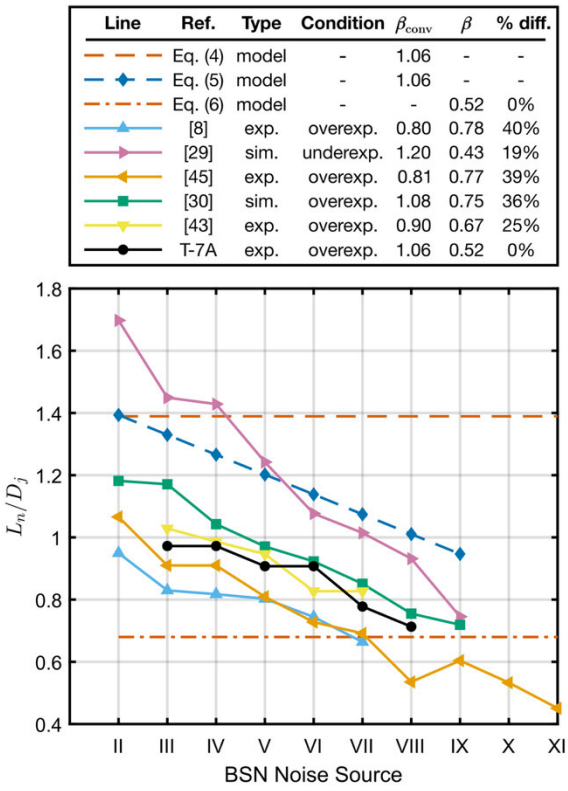

Figure 5. Inter-shock spacing for the jet in the present study compared with various models and other data sources in the literature. Details for each data source are given in the legend, including the data type (model, experiment, simulation), values of β_{conv} and β, as well as the percent difference between each value of β and that from the T-7A/F404 in this study.

Also noteworthy is that the underexpanded jet from Liu et al. [29], despite being a highly-heated supersonic F404-like jet with the closest β value among the comparisons, exhibits significantly larger shock spacing. Similar trends were observed in other underexpanded jets not shown here. While Eqs. (4) and (5) align well with the underexpanded jets, they fail to predict shock spacing for the overexpanded cases, likely due to their original design for convergent nozzles. Nevertheless, Eq. (5) agrees reasonably with L_{V-VIII} for the underexpanded jet in [29], even though it emanates from a C–D nozzle.

Furthermore, Eq. (6), which uses β instead of β_{conv}, does not reliably predict the average shock spacing for the jet in this study. The reason for this discrepancy is unclear but may stem from the limitations of using constants from convergent nozzle theory in C–D nozzle applications. This highlights the need for a more accurate, analytically derived model tailored to supersonic jets from C–D nozzles.

Also included in Fig. 5 are shock locations inferred from localized BSN sources by Harper-Bourne [43], using an acoustic mirror technique. Although that experiment used a cold, laboratory-scale model jet, the shock spacing results closely resemble those observed in this study. Both jets are overexpanded with similar β values. This similarity suggests that shock spacing—and hence the locations of BSN sources—is relatively insensitive to TTR and may be more directly correlated with β and whether the jet is over- or underexpanded.

Interestingly, when comparing the inferred shock locations from the T-7A/F404 with other datasets, the expansion condition appears to be the dominant factor influencing shock spacing, followed by β. The two datasets that showed the closest agreement were both overexpanded jets with the most similar values of β. However, even in these cases, β differed by as much as 36% from the T-7A/F404 value—highlighting that while β is a useful parameter, it alone may not fully capture the complexity of shock spacing behavior as appreciably large differences in β between different experiments gave similar results in terms of shock spacing.

In summary, shock cell spacing estimated from acoustical holography reveals limitations in current analytical models. While models such as the Prandtl–Pack relation and its variants provide reasonable predictions for underexpanded jets, they consistently fail to capture shock spacing in overexpanded flows from C–D nozzles. Notably, the trend of larger shock spacing in underexpanded jets compared to overexpanded ones is not reflected in existing formulations. These discrepancies highlight the need for updated models that accurately apply to C–D nozzles and span both over- and underexpanded regimes.

C. Peak Frequency

Another key characteristic of BSN is its spectral peak frequency, which varies with angle—generally increasing as the observer moves downstream. Various models have been developed to describe this behavior, most of which build upon the formulation by Harper-Bourne and Fisher [1], which expresses the peak frequency as:

$$f_{pk}(\theta) = \frac{U_c}{\bar{L}\,(1 - M_c\,cos\,\phi)}, \tag{7}$$

where U_c is the convection velocity (typically taken as $0.7U_j$), $\bar{L}$ is the characteristic shock cell spacing, M_c is the convective Mach number, and $\phi = 180^\circ - \theta$ is the angle relative to the jet axis. This model has been widely used in BSN studies [5,6,9]. In the present work, both the measured average shock spacing ($\bar{L}_{\text{meas}}$) and the estimates from Eqs. (4) and (6) are used.

To identify BSN propagation angles, a shock noise reference point (SNRP) was selected based on the relative amplitudes of shock signatures in Fig. 4. Since signatures VI and VII exhibited the strongest amplitudes, the SNRP was placed between them at $x/D_j = 5.6$ and this point was used as the origin from which to compute propagation angles. Figure 6(a) shows the SNRP location, several microphone positions, and their inlet angles relative to the SNRP. The corresponding autospectral densities are shown in Fig. 6(b), plotted against both frequency and Strouhal number. As expected, the BSN peak frequency increases with aftward angle, becoming most prominent between 40° and 60°.

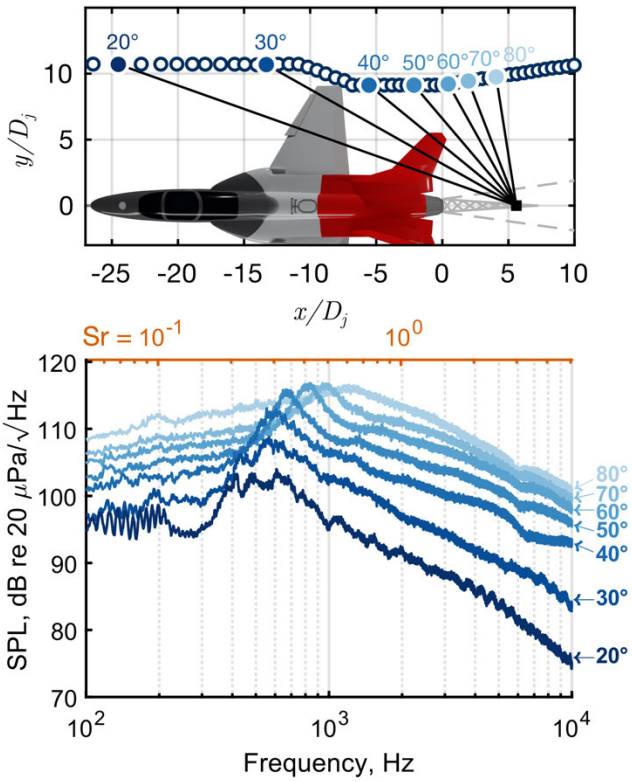

Figure 6. (a) Location of shock noise reference point and microphone locations for several angles. (b) Autospectral densities for each of the microphone locations indicated in (a).

To present a more comprehensive view of the BSN peak frequency angular variation, Figure 7(a) presents a spatiospectral map of SPL across the imaging array as a function of frequency and angle relative to the SNRP. The white line tracks the peak frequency trend. BSN dominates at angles below ~85°, while mixing noise prevails at angles >90°. Figure 7(b) isolates the peak frequency versus angle for clarity, and compares it with the model prediction from Eq. (6), evaluated using three different shock spacing estimates: one from Eq. (4), another from Eq. (6), and the $\bar{L}_{\text{meas}}$ as determined from Fig. 4 for the T-7A/F404 at AB. As expected, Eq. (4) performs poorly—consistent with its derivation for convergent nozzles and the mismatch shown in Fig. 5.

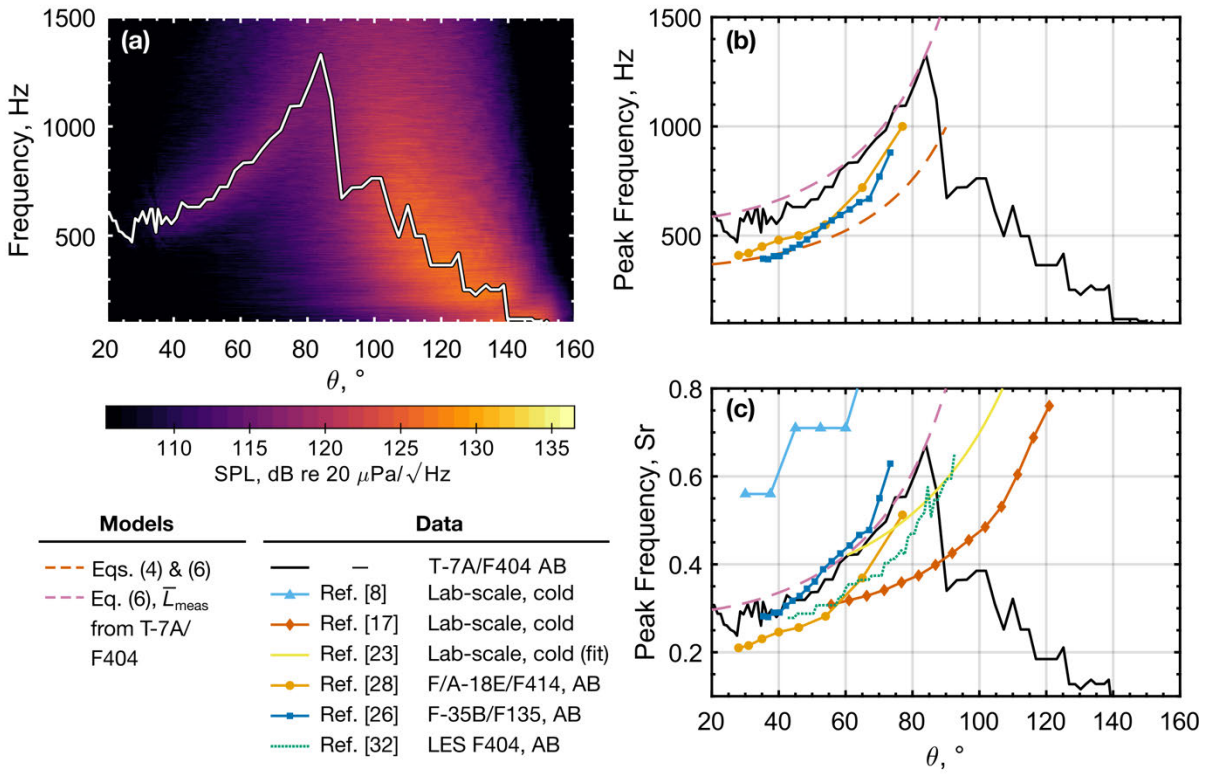

Figure 7. a) Spatiospectral map showing the sound pressure level at the imaging array, as a function of frequency and angle relative to the MARP. The peak frequency at each angle is shown by the white line. b) The peak frequency is depicted as a function of angle relative to the SCRP; additionally, two BSN peak frequency models are shown and two full-scale data sources are compared. c) The peak Strouhal number is shown as a function of angle relative to the SCRP, several datasets from the literature are also shown.

Additionally, Fig. 8(b) includes full-scale data from Refs. [26] and [28]. While trends are similar, the BSN peak frequencies measured here are consistently higher—by roughly half an octave—likely due to differences in jet diameter and velocity. To facilitate comparison across scales, Fig. 7(b) is recast in terms of Strouhal number in Fig. 7(c). Jet parameters from Refs. [26] and [28] were approximated for this conversion. For Ref. [26], values of $U_j \approx$ 1400 m/s and $D_j \approx 1.0$ m were assumed. Ref. [28] lacked direct AB-condition parameters, but Seiner et al. [47] reported MIL-condition data for the same engine. A nominal 150% increase in Uj and Dj from MIL to AB yields approximate values of $U_j \approx 1210$ m/s and $D_j \approx 0.62$ m. While the trend from Ref. [26] aligns reasonably well, Ref. [28] reports lower Strouhal numbers, suggesting either physical differences or inaccuracies in parameter estimation.

Also shown in Fig. 7(c) are peak Strouhal number trends from several laboratory-scale jets [8,17,23]. These differ significantly from the T-7A and other full-scale results. The largest discrepancy is with Norum and Seiner [8], while data from Refs. [17] and [23] show moderate agreement but suggest more forward BSN radiation. One likely factor is temperature ratio: the lab-scale jets are cold, whereas the full-scale jets operate with afterburners. Kuo et al. [21] showed that for overexpanded jets, peak BSN frequency decreases with increasing TTR. Their data (up to TTR = 2.2) showed an 18% decrease in peak Strouhal number at 120° between TTR = 1 and TTR = 2.2. Given that AB operation corresponds to TTR ≈ 7, much lower peak Strouhal numbers are expected. Unfortunately, no afterburner-like lab-scale data are available in the open literature for direct comparison.

Lastly, Fig. 8(c) includes peak Strouhal trends from a large-eddy simulation of a TTR = 7 jet with an F404-like nozzle analyzed by Leete et al. [32]. While the LES results trend similarly to the T-7A data, their frequencies are generally lower, suggesting that while LES captures key features of afterburning BSN, further refinement is needed to match experimental results more closely.

D. Coherence Analysis

Signal coherence is a valuable tool for assessing the linear relationship between two signals in the frequency domain. Coherence analyses have been employed by many recent jet noise studies to characterize various properties of jet noise[32,37,48-52]. In this study, coherence between the reconstructed sources at the nozzle lipline and microphones in the imaging array is used to investigate the source and propagation behavior of broadband shock-associated noise (BSN). Figure 8 shows coherence maps between each reconstructed source location at the lipline shock maxima (as identified in Fig. 4) and the field microphones. Each subfigure corresponds to a specific apparent source (II–VIII), and plots coherence (γ^2) as a function of observer angle and Strouhal number. These maps provide insight into how energy from each apparent source radiates throughout the field.

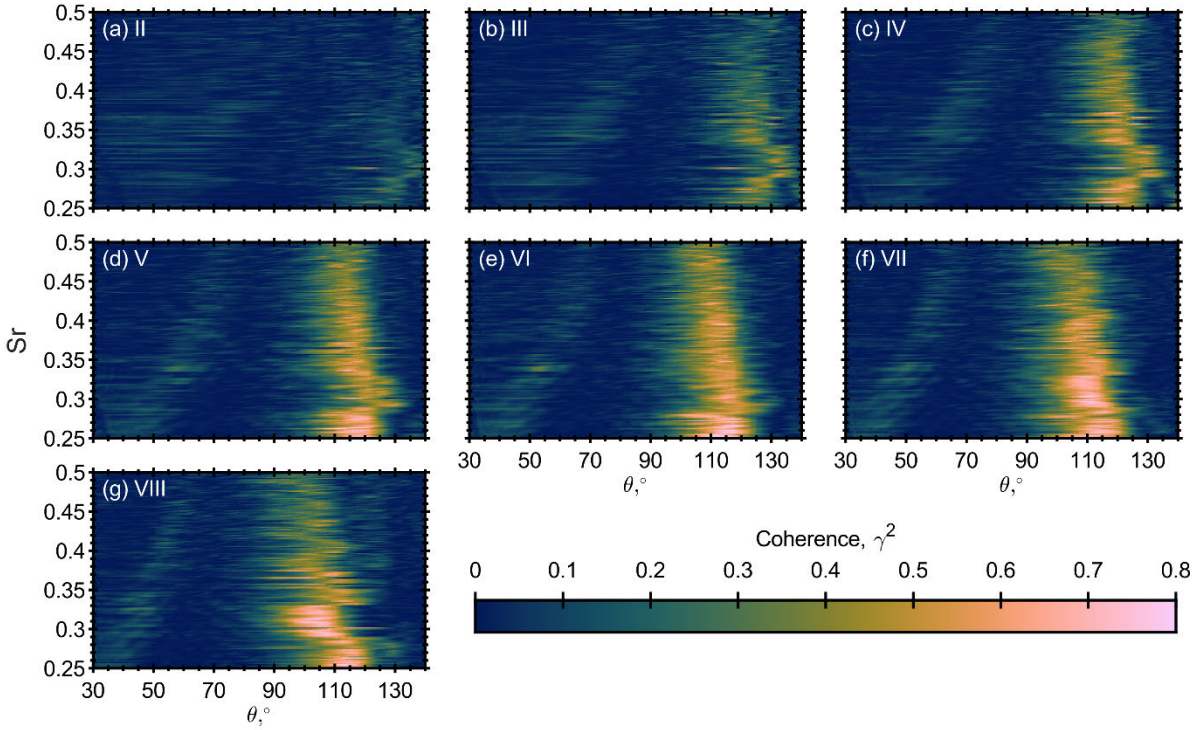

Figure 8. Coherence between each indicated shock locations at the nozzle lipline and imaging array microphones. Results are shown as a function of downstream distance as well as propagation angle relative to shock lipline location.

A few key trends are apparent. First, most apparent sources exhibit appreciable coherence with the field microphones over two distinct regions—aft (e.g., from 90-130°) and forward (e.g. 30-90°). This corresponds to the relative regions where mixing noise and BSN dominate, respectively as seen in Fig. 7(a). While the downstream angles have the greatest coherence with the apparent source locations, there is still moderate coherence levels at the upstream angles. This supports the idea that the turbulence interacting with the shock cells not only radiates Mach-wave-like energy downstream but also excites upstream-directed components. This supports similar findings by Swift et al.[51] at full-scale and Leete et al.[32] for a simulated, TTR = 7 jet.

Among the apparent sources, locations V-VIII exhibit the strongest and broadest coherence with the field, especially at mid-to-high angles. This suggests these sources contribute most prominently to the radiated BSN field and may correspond to the region of highest shock-turbulence interaction intensity. In contrast, sources II-IV show weaker coherence, particularly at higher Strouhal numbers, indicating their limited contribution to radiated BSN.

With coherence between the source region and the field established, further insight is gained by examining coherence within the source region itself. Figure 9 presents a coherence map computed between all pairs of lipline reconstruction locations—effectively a spatial correlation map along the nozzle lipline. Each axis corresponds to a location along the lipline (in diameters), and the color indicates the magnitude of coherence between source pairs.

Several key observations emerge from this map. First, location II again shows weak coherence with all other lipline locations, suggesting it may be acoustically isolated or that its contribution to the BSN mechanism is minimal. This aligns with the weak field coherence observed in Fig. 8(a). For sources III–VIII, however, a clear pattern of structured

coherence appears. The box-like shape and diagonal striations across the map reveal correlated activity between distinct shock locations.

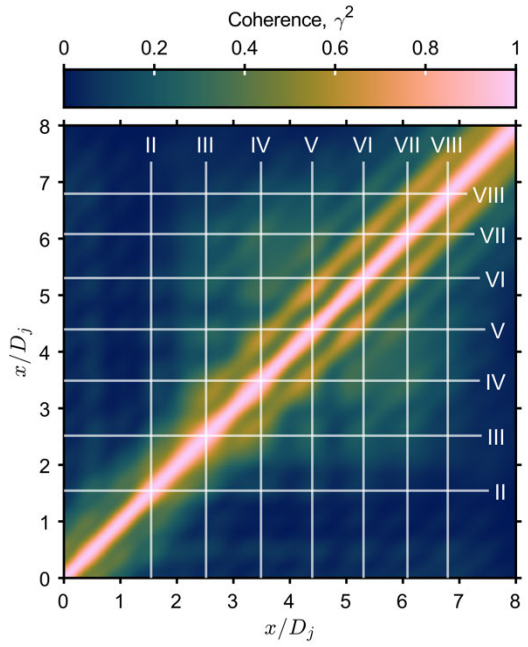

Figure 9. Coherence map along nozzle lipline with white grid lines indicating apparent shock noise source locations.

These off-diagonal coherence "islands" suggest that BSN generation is not purely localized but involves spatially distributed interactions—potentially due to the coherent advection of turbulence structures across multiple shock cells. For example, strong coherence between source III and sources IV–VII implies that a single turbulence structure/wavepacket may interact coherently with several consecutive shocks, radiating BSN at multiple spatial points. This fits with the findings of Seiner and Yu [10], who found appreciable spatial coherence spanning several shock wavelengths via correlations between near-field acoustic and flow sensors. Additionally, several recent wavepacket-based models for BSN include spatial coherence factors to appropriately model BSN [22,24].

In summary, the coherence analysis in Figs. 9 and 10 reveals that BSN generation is not confined to isolated points but is distributed and partially correlated across multiple shock cells. Certain locations, especially VI and VII, dominate the field radiation and share coherent links with other source regions. This supports the notion of a partially correlated BSN source mechanism, where turbulence structures interacting with successive shock cells generate spatially structured radiation. These findings emphasize the importance of modeling BSN as a distributed and interconnected source field, rather than as a sum of isolated monopoles.

IV. CONCLUSION

Acoustic holography applied to a full-scale, installed F404 engine in afterburning overexpanded operation has revealed apparent sources of broadband shock-associated noise (BSN) along the nozzle lipline. These sources were identified solely from far-field microphone array measurements and show clear spatial correlation with shock structures visible in in-situ photographs of the jet in operation. The observed shock spacing matches closely with that seen in other similar overexpanded jets from the literature at both laboratory scale and in large-eddy simulations, yet two widely used analytical models—originally developed for convergent nozzles—fail to predict this spacing accurately. A possible generalization of the Prandtl–Pack model, replacing the off-design parameter with one adapted for convergent-divergent nozzles, also underperforms, highlighting the need for updated models that properly work for convergent-divergent nozzles and factor in whether the jet is under- or overexpanded.

Measured BSN peak frequencies show good agreement with other full-scale engine data when normalized by Strouhal number but diverge from laboratory-scale results—likely due to temperature differences, particularly the absence of afterburner heating in lab jets—but also possibly including other differences in the flow physics. The

Harper-Bourne and Fisher model for BSN peak frequency, when paired with analytic shock spacing estimates, fails to produce accurate BSN predictions for the F404/T-7A, however, substituting the measured average shock spacing yields excellent agreement. This underscores the potential for improved BSN modeling if shock spacing can be more accurately predicted.

Coherence analysis provides further insight into BSN radiation mechanisms. Apparent sources downstream—particularly BSN sources V-VII—exhibit strong coherence with the acoustic field downstream and moderate coherence upstream. Moreover, elevated coherence between multiple lipline shock locations suggests a spatially distributed, partially correlated source mechanism, wherein turbulence structures interact coherently with multiple shock cells. Overall, these findings reinforce the idea that BSN should be modeled not as a set of isolated monopole sources, but as a distributed and interconnected series of sources. Improved predictive models for shock spacing—specifically for C–D nozzles—could enhance both spectral and spatial predictions of BSN and inform jet noise reduction in future engine designs.

Funding Sources

The authors acknowledge the Office of Naval Research for funding under grant number N00014-21-1-2069 with project monitor Steven Martens, Code 351 Jet Noise Reduction. The measurements were funded through the Advanced Pilot Training System Program Office and the Air Force Research Laboratory. This research was supported in part by the appointment of L. T. M. to the Department of Defense (DOD) Research Participation Program administered by the Oak Ridge Institute for Science and Education (ORISE) through an interagency agreement between the U.S. Department of Energy (DOE) and the DOD. ORISE is managed by Oak Ridge Associated Universities (ORAU) under DOE contract number DE-SC0014664. All opinions expressed in this paper are the authors' and do not necessarily reflect the policies and views of DOD, DOE, or ORAU/ORISE.

Professor Daniel Edgington-Mitchell of Monash University is thanked for his helpful discussion relating to this analysis.

References

[1] Harper-Bourne, M., and Fisher, M. J., "The Noise from Shock Waves in Supersonic Jets," *Proc. AGARD Conf.*, Conference Preprint 131, September 1973.

[2] Powell, A., "On the Mechanism of Choked Jet Noise," *Proc. Phys. Soc. B* **66**(12), pp. 1039-1057 (1953). https://doi.org/10.1088/0370-1301/66/12/306

[3] Yu, J. C., and Seiner, J. M., "Nearfield Observations of Tones Generated from Supersonic Jet Flows," *AIAA 8th Aeroacoustics Conference*, AIAA Paper 1983-0706, April 1983. https://doi.org/10.2514/6.1983-706

[4] Seiner, J. M., and Norum, T. D., "Aerodynamic aspects of shock containing jet plumes," *AIAA 6th Aeroacoustics Conference*, AIAA Paper 1980-0965, June 1980. https://doi.org/10.2514/6.1980-965

[5] Tanna, H. K., "An experimental study of jet noise part II: Shock associated noise," *Journal of Sound and Vibration* **50**(3), pp. 429-444 (1977). https://doi.org/10.1016/0022-460X(77)90494-1

[6] Howe, M. S., and Ffowcs-Williams, J. E., "On the noise generated by an imperfectly expanded supersonic jet," *Philosophical Transactions of the Royal Society of London. Series A, Mathematical and Physical Sciences* **289**(1358), pp. 271–314 (1978). http://doi.org/10.1098/rsta.1978.0061

[7] Norum, T. D., and Seiner, J. M., "Broadband Shock Noise from Supersonic Jets," *AIAA J.* **20**(1), pp. 68-73 (1982). https://doi.org/10.2514/3.51048

[8] Norum, T. D., and Seiner, J. M., "Measurements of Mean Static Pressure an d Far-Field Acoustics of Shock-Containing Supersonic Jets," NASA TM-84521 (1982).

[9] Pao, S. P., and Seimer, J. M., "Shock-Associated Noise in Supersonic Jets," *AIAA J.* **21**(5), pp. 687-693 (1983). https://doi.org/10.2514/3.8134

[10] Seiner, J. M., and Yu, J. C., "Acoustic Near-Field Properties Associated with Broadband Shock Noise," *AIAA J.* **22**(9), pp. 1207-1215 (1984). https://doi.org/10.2514/3.8762

[11] Tam, C. K. W., and Tanna, H. K., "Shock associated noise of supersonic jets from convergent-divergent nozzles," *Journal of Sound and Vibration* **81**(3), pp. 337-358 (1982). https://doi.org/10.1016/0022-460X(82)90244-9

[12] Tam, C. K. W., Jackson, J. A., and Seiner, J. M., "A multiple-scales model of the shock-cell structure of imperfectly expanded supersonic jets," *Journal of Fluid Mechanics* **153**, pp. 129-149 (1985). https://doi.org/10.1017/S0022112085001173

[13] Tam, C. K. W., "Stochastic model theory of broadband shock associated noise from supersonic jets," *Journal of Sound and Vibration* **116**(2), pp. 265-302 (1987). https://doi.org/10.1016/S0022-460X(87)81303-2

[14] Lui, C., and Lele, S. K., "Sound Generation Mechanism of Shock-Associated Noise," *9th AIAA/CEAS Aeroacoustics Conference and Exhibit*, AIAA Paper 2003-3315, May 2003. https://doi.org/10.2514/6.2003-3315

[15] Long, D. F., "The Structure of Shock Cell Noise from Supersonic Jets," *11th AIAA/CEAS Aeroacoustics Conference*, AIAA Paper 2005-2840, May 2005. https://doi.org/10.2514/6.2005-2840

[16] Viswanathan, K., Alkislar, M. B., and Czech, M. J., "Characteristics of the Shock Noise Component of Jet Noise," *AIAA J.* **48**(1), pp. 25-46 (2010). https://doi.org/10.2514/1.38521

[17] Zaman, K. B. M. Q., Bridges, J. E., and Brown, C. A., "Excess Broadband Noise Observed with Overexpanded Jets," *AIAA J.* **48**(1), pp. 202-214 (2010). https://doi.org/10.2514/1.43383

[18] Miller, S. A. E., and Morris, P. J., "The prediction of broadband shock-associated noise including propagation effects," *International Journal of Aeroacoustics* **11**(7-8), pp. 755-781 (2012). https://doi.org/10.1260/1475-472X.11.7-8.75

[19] André, B., Castelain, T., and Bailly, C., "Broadband Shock-Associated Noise in Screeching and Non-Screeching Underexpanded Supersonic Jets," *AIAA J.* **51**(3), pp. 665-673 (2013). https://doi.org/10.2514/1.J052058

[20] Liu, J., Corrigan, A., Kailasanath, K., Heeb, N., Munday, D., and Gutmark, E. (2013). "Computational Study of Shock-Associated Noise Characteristics Using LES," *19th AIAA/CEAS Aeroacoustics Conference*, AIAA Paper 2013-2199, May 2013. https://doi.org/10.2514/6.2013-2199

[21] Kuo, C. W., McLaughlin, D. K., Morris, P. J., and Viswanathan, K., "Effects of Jet Temperature on Broadband Shock-Associated Noise," *AIAA J.* **53**(6), pp. 1515-1530 (2015). https://doi.org/10.2514/1.J053442

[22] Wong, M. H., Jordan, P., Honnery, D. R., and Edgington-Mitchell, D., "Impact of coherence decay on wavepacket models for broadband shock-associated noise in supersonic jets," *Journal of Fluid Mechanics* **863**, pp. 969-993 (2019). https://doi.org/10.1017/jfm.2018.984

[23] Wong, M. H., Kirby, R., Jordan, P., and Edgington-Mitchell, D., "Azimuthal decomposition of the radiated noise from supersonic shock-containing jets," *Journal of the Acoustical Society of America* **148**(4), pp. 2015-2027 (2020). https://doi.org/10.1121/10.0002166

[24] Wong, M. H., Jordan, P., Maia, I. A., Cavalieri, A. V. G., Kirby, R., Fava, T. C. L, and Edgington-Mitchell, D., "Wavepacket modelling of broadband shock-associated noise in supersonic jets," *Journal of Fluid Mechanics* **918**, A9 (2021). https://doi.org/10.1017/jfm.2021.324

[25] Nogueira, P. A. S., and Edgington-Mitchell, D., "Study of Broadband Shock-Associated Noise using the Parabolised Floquet Equations," *28th AIAA/CEAS Aeroacoustics Conference*, AIAA Paper 2022-3063, June 2022. https://doi.org/10.2514/6.2022-3063

[26] Vaughn, A. B., Neilsen, T. B., Gee, K. L., Wall, A. T., Downing, J. M., and James, M. M., "Broadband shock-associated noise from a high-performance military aircraft," *Journal of the Acoustical Society of America* **144**, EL242 (2018). https://doi.org/10.1121/1.5055392

[27] Aujogue, N., Huber, J., Julliard, E., Antoni, J., and Leclère, Q., "Experimental investigation of the supersonic jet noise from aircraft engines using acoustic imaging," *28th AIAA/CEAS Aeroacoustics 2022 Conference*, AIAA Paper 2022-2867, Jun. 2022. https://doi.org/10.2514/6.2022-2867

[28] Tam, C. K. W., Aubert, A. C., Spyropoulos, J. T., and Powers, R. W., "On the dominant noise components of tactical aircraft: Laboratory to full scale," *Journal of Sound and Vibration* **422**, pp. 92-111 (2018). https://doi.org/10.1016/j.jsv.2018.02.023

[29] Liu, J., Corrigan, A. T., Kailasanath, K., and Taylor, B. D., "Impact of the Specific Heat Ratio on the Noise Generation in a High-Temperature Supersonic Jet," *54th AIAA Aerospace Sciences Meeting*, AIAA Paper 2016-2125, Jan. 2016. https://doi.org/10.2514/6.2016-2125

[30] Liu, J., and Ramamurti, R., "Numerical Study of Supersonic Jet Noise Emanating from an F404 Nozzle at Model Scale," *AIAA SciTech Forum*, AIAA Paper 2019-0807, Jan. 2019. https://doi.org/10.2514/6.2019-0807

[31] Brès, G. A., Towne, A., and Lele, S. K., "Investigating the effects of temperature non-uniformity on supersonic jet noise with large-eddy simulation," *25th AIAA/CEAS Aeroacoustics Conference*, AIAA Paper 2019-2730, May 2019. https://doi.org/10.2514/6.2019-2730

[32] Leete, K. M., Gee, K. L., Liu, J., and Wall, A. T., "Coherence Analysis of the Noise from a Simulated Highly Heated Laboratory-Scale Jet," *AIAA J.* **58**(8), pp. 3426-3435 (2020). https://doi.org/10.2514/1.J059112

[33] Murray, N. E., Tinney, C. E., and Panickar, P., "Laboratory-Scale Afterburning Supersonic Jet Noise Reduction using Contoured Inserts," *28th AIAA/CEAS Aeroacoustics Conference*, AIAA Paper 2022-3030, Jun. 2022. https://doi.org/10.2514/6.2022-3030

[34] Kumar, A., Meadows, J., Olaveson, T. W., Gee, K. L., Mathews, L. T., and Pratt, H. J., "Far-field noise measurements of a supersonic jet operating near afterburning conditions," *Aerospace Science and Technology* **157**, 109842 (2025). https://doi.org/10.1016/j.ast.2024.109842

[35] Leete, K. M., Vaughn, A. B., Bassett, M. S., Rasband, R. D., Novakovich, D. J., Gee, K. L., Campbell, S. C., Mobley, F. S., and Wall, A. T., "Jet Noise Measurements of an Installed GE F404 Engine," *AIAA SciTech Forum*, AIAA Paper 2021-1638, Jan. 2021. https://doi.org/10.2514/6.2021-1638

[36] Anderson, J. D., *Modern Compressible Flow: With Historical Perspective*, 4th ed., McGraw-Hill, New York, 2021.

[37] Mathews, L. T., and Gee, K. L., "Acoustical Holography and Coherence-Based Noise Source Characterization of an Installed F404 Engine," *AIAA J.* **62**(6), pp. 2186-2199 (2024). https://doi.org/10.2514/1.J063543

[38] Hald, J., "Basic Theory and Properties of Statistically Optimized Near-Field Acoustical Holography," *Journal of the Acoustical Society of America* **125**(4), pp. 2105–2120 (2009). https://doi.org/10.1121/1.3079773

[39] Wall, A. T., Gee, K. L., and Neilsen, T. B., "Multisource Statistically Optimized Near-Field Acoustical Holography," *Journal of the Acoustical Society of America* **137**(2), pp. 963–975 (2015). https://doi.org/10.1121/1.4906585

[40] Wall, A. T., Gee, K. L., Neilsen, T. B., McKinley, R. L., and James, M. M., "Military Jet Noise Source Imaging Using Multisource Statistically Optimized Near-Field Acoustical Holography," Journal of the Acoustical Society of America, **139**(4), pp. 1938–1950 (2016). https://doi.org/10.1121/1.4945719

[41] Leete, K. M., Wall, A. T., Gee, K. L., Neilsen, T. B., James, M. M., and Downing, J. M., "Acoustical Holography-Based Analysis of Spatiospectral Lobes in High-Performance Aircraft Jet Noise," *AIAA J.* **59**(10), pp. 4166-4178 (2021). https://doi.org/10.2514/1.J059400

[42] Morata, D., and Papamoschou, D., "High-Resolution Continuous-Scan Beamforming," *AIAA J.* **61**(1), pp. 429-443 (2023). https://doi.org/10.2514/1.J061910

[43] Harper-Bourne, M., "The Jet Noise of a Convergent-Divergent Nozzle," *28th AIAA/CEAS Aeroacoustics 2022 Conference*, AIAA Paper 2022-2827, Jun. 2022. https://doi.org/10.2514/6.2022-2827

[44] Nagamatsu, H. T., Sheer, R. E., and Horvay, G., "Supersonic Jet Noise Theory and Experiments," in Basic Aerodynamic Noise Research, NASA SP-207, July 1969.

[45] Podboy, G. G., Wernet, M. P., Clem, M. M., and Fagan, A. F., "Noise Source Location and Flow Field Measurements on Supersonic Jets and Implications Regarding Broadband Shock Noise," NASA TM-2017-219544 (2017).

[46] Pack, D. C., "A note on Prandtl's formula for the wavelength of a supersonic gas jet," Q. J. Mech. Appl. Math. **3**, pp. 173–181 (1950); doi.org/10.1093/qjmam/3.2.173.

[47] Seiner, J. M., Jansen, B. J., and Ukeiley, L. S., "Acoustic Fly-Over Studies of F/A-18 E/F Aircraft During FCLP Mission," *9th AIAA/CEAS Aeroacoustics Conference*, AIAA Paper 2003-3330, May 2003. https://doi.org/10.2514/6.2003-3330

[48] Harker, B. M., Neilsen, T. B., Gee, K. L., Wall, A. T., and James, M. M., "Spatiotemporal-Correlation Analysis of Jet Noise from a High-Performance Military Aircraft," AIAA J. 54(5), pp. 1554-1566 (2016). https://doi.org/10.2514/1.J054442

[49] Miller, S. A. E., "Broadband shock-associated noise near-field cross-spectra," Journal of Sound and Vibration 372, pp. 82-104 (2016). https://doi.org/10.1016/j.jsv.2016.01.048

[50] Leete, K. M., Wall, A. T., Gee, K. L., Neilsen, T. B., Harker, B. M., and James, M. M., "Azimuthal coherence of the sound field in the vicinity of a high performance military aircraft," Proceedings of Meetings on Acoustics 29, 045007 (2016). https://doi.org/10.1121/2.0000673

[51] Swift, S. H., Gee, K. L., Neilsen, T. B., Wall, A. T., Downing, J. M., and James, M. M., "Spatiotemporal-correlation analysis of jet noise from a round nozzle high-performance aircraft," 2018 AIAA/CEAS Aeroacoustics Conference, AIAA Paper 2018-3938, June 2018. https://doi.org/10.2514/6.2018-3938

[52] Harker, B. M., Gee, K. L., Neilsen, T. B., Wall, A. T., and James, M. M., "Source characterization of full-scale tactical jet noise from phased-array measurements," Journal of the Acoustical Society of America 146(1), pp. 665-680 (2019). https://doi.org/10.1121/1.5118239

Chapter 4

An overview of acoustical measurements made of the Atlas V JPSS-2 rocket launch

On 10 November 2022, measurements were made of the Atlas V JPSS-2 rocket launch from SLC-3E at Vandenberg Space Force Base, California. Primarily, this chapter documents azimuthal asymmetry in both the ignition overpressure of the rocket as well as in the spectral peak frequency at peak directivity. This second finding represents the first documentation and analysis of this phenomenon in the open literature. Of note, Eqs. (1-3) contain an error, where geometric spreading was incorrectly shown as $20\log_{10}(4\pi r^2)$ instead of $10\log_{10}(4\pi r^2)$. This has been corrected in the updated methodology outlined in Chapter 5 of this dissertation. This chapter is an article published as L. T. Mathews, M. C. Anderson, C. D. Gardner, B. W. McLaughlin, B. M. Hinds, M. R. McCullah-Boozer, L. K. Hall, and K. L. Gee, "An overview of acoustical measurements made of the Atlas V JPSS-2 rocket launch," *Proc. Mtgs. Acoust.* **51**, 040003 (2025). https://doi.org/10.1121/2.0001768. It is reprinted in this dissertation under the terms of ASA's Transfer of Copyright Agreement, item 3 with the article cover page per ASA policy. I hereby confirm that the use of this article is compliant with all publishing agreements.

SEPTEMBER 15 2023

An overview of acoustical measurements made of the Atlas V JPSS-2 rocket launch FREE

Logan T. Mathews ; Mark C. Anderson; Carson D. Gardner; Bradley W. McLaughlin; Brooke M. Hinds; Megan R. McCullah-Boozer; Lucas K. Hall; Kent L. Gee

Proc. Mtgs. Acoust. 51, 040003 (2023)
https://doi.org/10.1121/2.0001768

Volume 51 http://acousticalsociety.org/

184th Meeting of the Acoustical Society of America

Chicago, Illinois

8-12 May 2023

*Noise: Paper 1aNS9

An overview of acoustical measurements made of the Atlas V JPSS-2 rocket launch

Logan T. Mathews, Mark C. Anderson, Carson D. Gardner and Bradley W. McLaughlin
Department of Physics and Astronomy, Brigham Young University, Provo, UT, 84602; loganmathews103@gmail.com; anderson.mark.az@gmail.com; cgard25@byu.edu; mclau4@byu.edu

Brooke M. Hinds, Megan R. McCullah-Boozer and Lucas K. Hall
Department of Biology, California State University Bakersfield, Bakersfield, CA, 93311; bhinds@csub.edu; mmccullah@csub.edu; lhall12@csub.edu

Kent L. Gee
Department of Physics and Astronomy, Brigham Young University, Provo, UT, 84602; kentgee@byu.edu

On 10 November 2022, measurements were made of the Atlas V JPSS-2 rocket launch from SLC-3E at Vandenberg Space Force Base, California. Measurements were made at 11 stations from distances of 200 m to 7 km from the launch pad. Measurement locations were arranged at various azimuthal angles relative to the rocket to investigate possible noise asymmetry. This paper discusses preliminary results from this measurement including overall levels, temporal and spectral characteristics, evidence of nonlinear propagation, and potential azimuthal asymmetry effects.

**POMA Student Paper Competition Winner*

Published by the Acoustical Society of America

 https://doi.org/10.1121/2.0001768

1. INTRODUCTION

In an era when the space launch industry is experiencing rapid growth, proper understanding of rocket launch acoustics is of ever-growing importance[1]. With increased launch cadence and the construction of new launch facilities, the understanding and modeling of rocket noise is vital to the design of rockets and payloads, pad and ground facilities design, and environmental and community noise assessments. To this end, acoustical measurements of rocket launches can inform noise models and regulations[2]. This paper gives an overview of one such measurement of a medium-lift orbital rocket launch and explores some of the basic acoustic characteristics observed.

Since most launch vehicles in use today have multi-nozzle configurations, understanding the associated effects on the acoustic radiation is important. This becomes particularly relevant when there is asymmetry in the nozzle configuration which creates the possibility for plume shielding, resulting in the potential for azimuthal asymmetry in the noise radiation. While the jet noise community has studied clustered jet effects widely, studies particular to rocket noise have been sparse. Several numerical and experimental studies on supersonic jets have shown an effective shielding of overall levels on the order of 2-3 dB in twin jets[3-6].

Eldred et al.[7] proposed a model for the flow characteristics of multi-nozzle jet noise flows. For jets spaced closer than 3 nozzle diameters, a two-zone model for noise production was proposed. The radiated noise was expected to consist of single-nozzle type radiation originating from the portion of the flow upstream of where coalescence begins and combined-nozzle type radiation originating farther downstream where the flows have effectively coalesced. This results in a double-peaked spectrum, with the higher frequency peak corresponding to single-nozzle behavior and a lower frequency peak corresponding to the combined flow. Kandula[8] successfully applied this model in conjunction with the propagation methodology from Eldred[9] (NASA SP-8072) to predict sound pressure level spectra from a clustered-nozzle rocket configuration. Potter and Crocker[10] extended Eldred's methodology to rocket noise but noted its inherent limited characteristics; namely that the computation assumes a flow of constant density and that rocket exhausts are much more extreme in temperature, velocity, etc. than turbojets.

The purpose of this paper is to document the acoustical measurement of the Atlas V JPSS-2 launch and to publish relevant preliminary findings. An analysis of the ignition overpressure event is shown, with azimuthal variability in peak levels being shown to correspond with the flame trench orientation. Maximum overall levels are shown, and a simple method for predicting this parameter is shown to be accurate at all stations with an uncertainty of ±2.5 dB. Evidence of nonlinearity in signals is shown. Spectral characteristics are discussed. Evidence for and against azimuthal asymmetry in launch noise due to the nozzle configuration is discussed, both in terms of maximum overall levels and spectral peak frequency.

2. METHODS

A. LAUNCH VEHICLE

The Atlas V is a medium- to heavy-lift launch vehicle developed and operated by United Launch Alliance. A diagram of the Atlas V rocket is shown in Fig. 1. It is the last member of the Atlas rocket family, which originated with the SM-65 Atlas ballistic missile in 1957. As of this article's publication, 97 Atlas V rockets have launched from two launch facilities: SLC-3E at Vandenberg Space Force Base (VSFB) and SLC-41 at Cape Canaveral Space Force Station (CCSFS). For this launch, the Atlas V vehicle was in the 401 configuration (four-meter fairing, no solid rocket boosters, and one RL10C-1 engine on the Centaur upper stage). Thus, the entirety of the first-stage thrust was generated by the RD-180 engine. The RD-180 engine, developed from the RD-170, is produced by NPO Energomash and is a single-engine unit with two closely spaced nozzles of diameter $D = 1.43$ m, each with a combined maximum thrust of 3.83 MN at sea level[11]. The equivalent diameter of a single nozzle with the same exit area as the two nozzles of the RD-180 is defined as $D_e = D\sqrt{2} = 2.02$ m. The approximate center-to-center distance between the nozzles is estimated to be approximately 1.63 m, which results in $S/D \approx 1.14$.

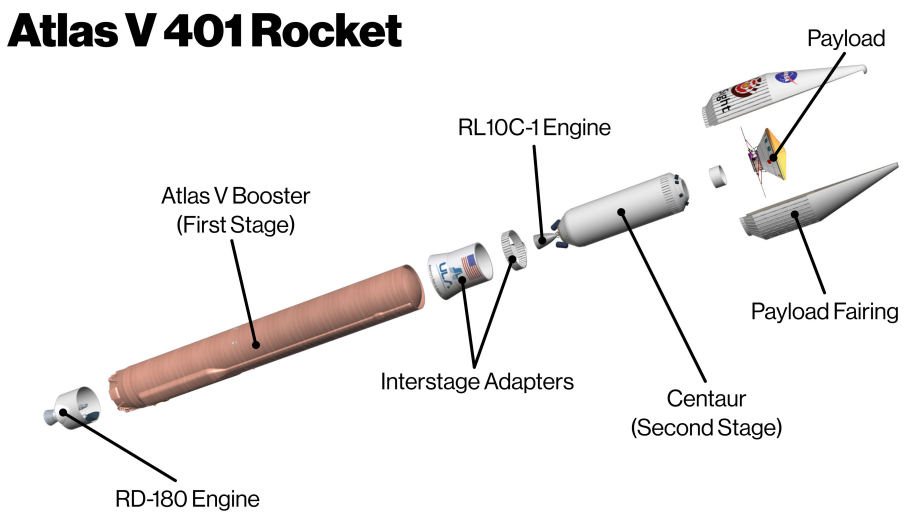

Figure 1. Atlas V 401 rocket diagram. Base image credit: NASA/JPL-Caltech. Public domain.

For reference, an azimuthal coordinate system relative to the rocket nozzle configuration has been defined for this analysis. A graphical overview of the coordinate system is presented in Fig. 2. The azimuthal angle φ indicates the orientation of the observer relative to the nozzles. At $\varphi = 0°$, the observer sees the two nozzles broadside (Fig. 2b), whereas at $\varphi = 90°$, the observer sees only one nozzle (Fig. 2c).

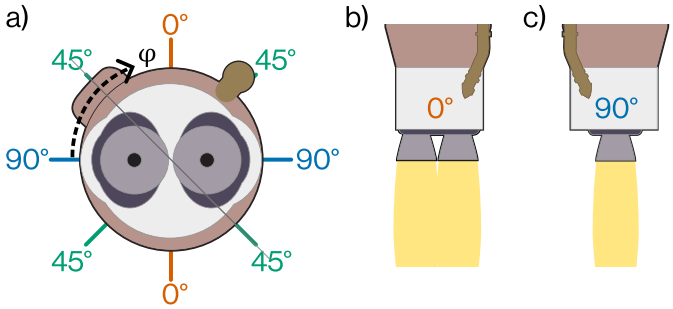

Figure 2. a) Orientation of rocket nozzles with the angle φ in the defined coordinate system. b) At φ = 0°, the observer sees two nozzles and cores broadside. c) At φ = 90°, the observer sees one nozzle/core end-on.

B. MEASUREMENT

On 10 November 2022 at 01:49 AM PST (09:49 AM UTC), an Atlas V 401 rocket lifted off from SLC-3E at Vandenberg Space Force Base, California, USA carrying the Joint Polar Satellite System (JPSS)-2 and Low-Earth Orbit Flight Test of an Inflatable Decelerator (LOFTID) payloads. Measurements were conducted at 11 primary stations, strategically placed around the rocket at radial distances ranging from 217 m to 7.2 km radially from the launch pad. Figure 3 shows the layout of these measurement locations, with the rocket axes defined in Fig. 2 shown. This measurement configuration is similar to a measurement conducted of the Atlas V Landsat 9 launch from the same facility, discussed by Cunningham et al.[12]. However, it should be noted that in the measurement by Cunningham et al., the measurement axes were defined relative to the Mobile Service Tower. However, the vehicle was discovered to be rotated by ~22° with respect to the building. This misalignment was noticed after the launch, and the axes were corrected in this measurement to align with the rocket properly.

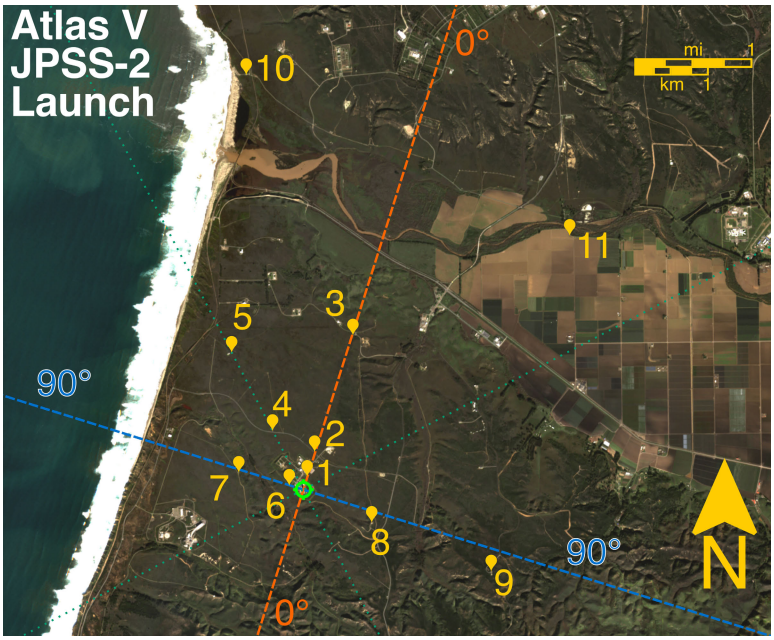

Figure 3. Map of measurement station locations at JPSS-2 launch. Station numbers and rocket axes are indicated.

A summary of each of the 11 measurement stations is reported in Table 1. The horizontal distance from the launch facility to the measurement location is reported as d. The actual angle with respect to the rocket axes, φ, is reported, as well as the approximate angle $\tilde{\varphi}$ (within ~±10°) for convenience in discussing similar angular site groupings.

Table 1. Station information with distances relative to the launch pad and angles in the described coordinate system.

Station	d (m)	φ	$\tilde{\varphi}$
1	217	2°	0°
2	656	4°	0°
3	2800	2°	0°
4	1080	47°	45°
5	2650	47°	45°
6	283	89°	90°
7	1118	87°	90°
8	1368	79°	90°
9	3625	82°	90°
10	7250	24°	30°
11	6430	31°	30°

Measurements were made with a mixture of custom PUMA (Portable Unit for Measuring Acoustics) systems, which consist of NI CompactDAQ data acquisition modules, a portable computer system running custom data acquisition software, and batteries for power[13]. Due to limited hardware resources at the time of the measurement, GPS time clocks were unavailable for absolute time synchronization across stations at this measurement. In addition to PUMA systems, Larson Davis 831C sound level meters were used at some locations, which recorded acoustic data as an uncompressed *WAV* file at a sample rate of 51.2 kHz and which has been determined to be of sufficient fidelity for rocket noise applications[14]. All systems had microphones placed in a custom ground plate/windscreen setup, referred to at BYU as a COUGAR (compact outdoor unit for ground-based acoustical recordings, see Anderson et al.[15]). Figure 4 shows the instrumentation setups at two representative stations. The COUGAR microphone setup can be seen in each, along with the instrumentation box and portable weather monitoring equipment on tripods.

Figure 4. (Left) Station 7 at 1.1 km. (Right) Station 6 at 283 m. In both images, the launch facility Mobile Service Tower is visible, and within it is the rocket. Also visible in the foregrounds are the microphone ground plate/windscreen setups, instrumentation boxes, and weather stations.

3. RESULTS

A. IGNITION OVERPRESSURE (IOP)

Ignition of the RD-180 engines on the Atlas V vehicle produces an ignition overpressure (IOP) event with a characteristic signature. Waveforms containing the IOP are shown for stations 1-9 in Fig. 5. The IOP signature for the Atlas V is unique; it produces a noticeable whooshing sound unlike IOPs observed on other vehicles such as the Falcon 9 and Space Launch System, which produce a more impulse-like signature. The unique behavior of this IOP is also shared with the Antares vehicle launched from the Mid-Atlantic Regional Spaceport. It is possible that the configuration of the flame trench could allow for strong resonances to be excited by the IOP event, producing the characteristic sound. It is also worth noting that the Antares vehicle uses RD-181 engines, which are largely the same as the RD-180 used on the Atlas V. Thus, the unique IOP signature of the Atlas V and Antares vehicles could also be related to the engines themselves.

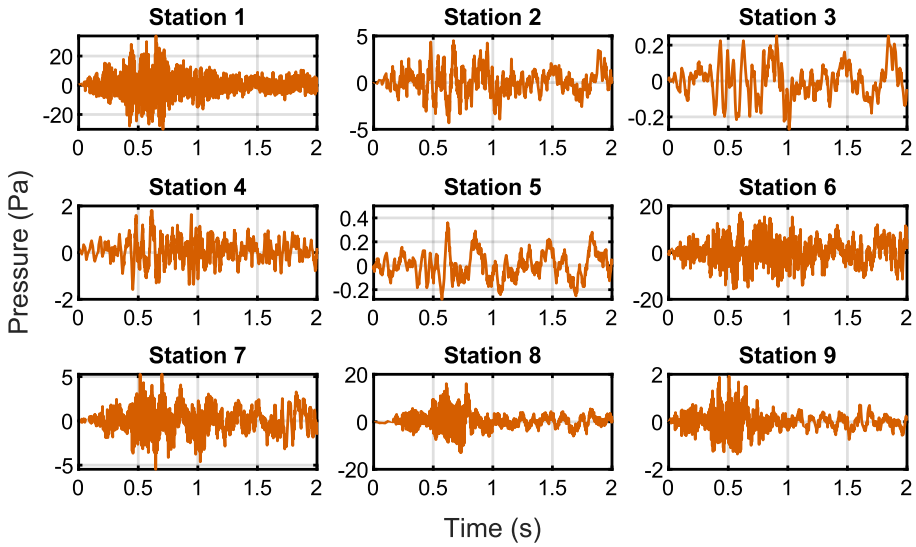

Figure 5. Ignition overpressure (IOP) waveform signatures from stations 1-9.

Figure 6 shows the peak sound pressure level (L_{pk}) associated with the IOP event at stations 1-9, relative to the mean L_{pk} across these stations. All levels have been scaled for spherical spreading to $100D_e$. The direction of the flame trench exit is indicated by the red dashed line. There is considerable azimuthal asymmetry in the scaled peak IOP levels. Stations closest to the flame trench exit azimuth consistently have a higher L_{pk} than average, with station 8 being 16 dB greater than the mean L_{pk}. Opposite the flame trench exit, there are consistently lower-than-average peak levels, with the lowest being 14 dB lower than average. This indicates a scaled variability of 30 dB in the IOP L_{pk}, which is considerable. Similar IOP asymmetry corresponding to the flame trench direction was noticed by Gee et al.[16] with the Space Launch System vehicle. This observation reinforces the understanding that significant IOP directionality exists with flame trenches, which should be considered when designing launch facilities and evaluating the environmental and ecological effects of rocket launches.

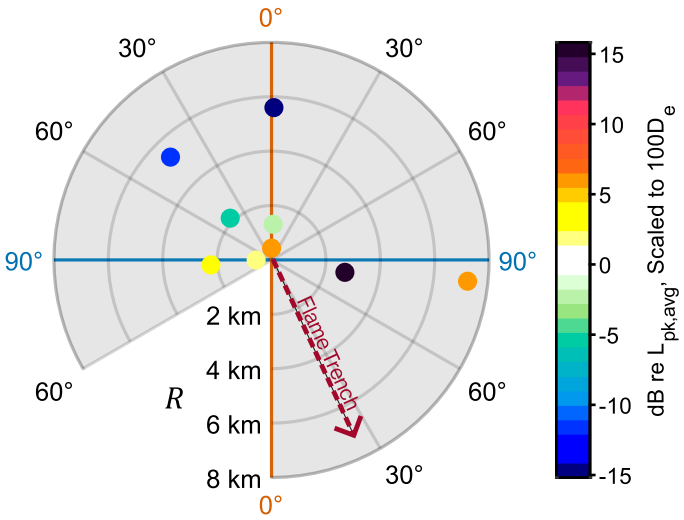

Figure 6. Ignition overpressure (IOP) peak levels, relative to the average across all depicted sites, adjusted for geometric spreading to 100D_e (202 m) from the launch pad. The direction of the flame trench exit is indicated by the dashed red line.

B. OVERALL SOUND PRESSURE LEVELS

Figure 7 shows the maximum 1-s averaged overall sound pressure levels ($\mathrm{OASPL_{max}}$) as a function of distance to the source (the distance being calculated assuming a peak overall directivity angle of 65°). Note that all levels reported in this discussion are referenced to 20 μPa unless otherwise noted. Also shown are the $\mathrm{OASPL_{max}}$ values adjusted for ground effects (triangular blue markers) by provisionally subtracting 6 dB from the level. This is a reasonable correction for the overall level as discussed by Hart et al.[17], since the majority of rocket noise energy is concentrated at sufficiently low frequencies that typical ground surfaces essentially create a pressure-doubling effect at the microphone.

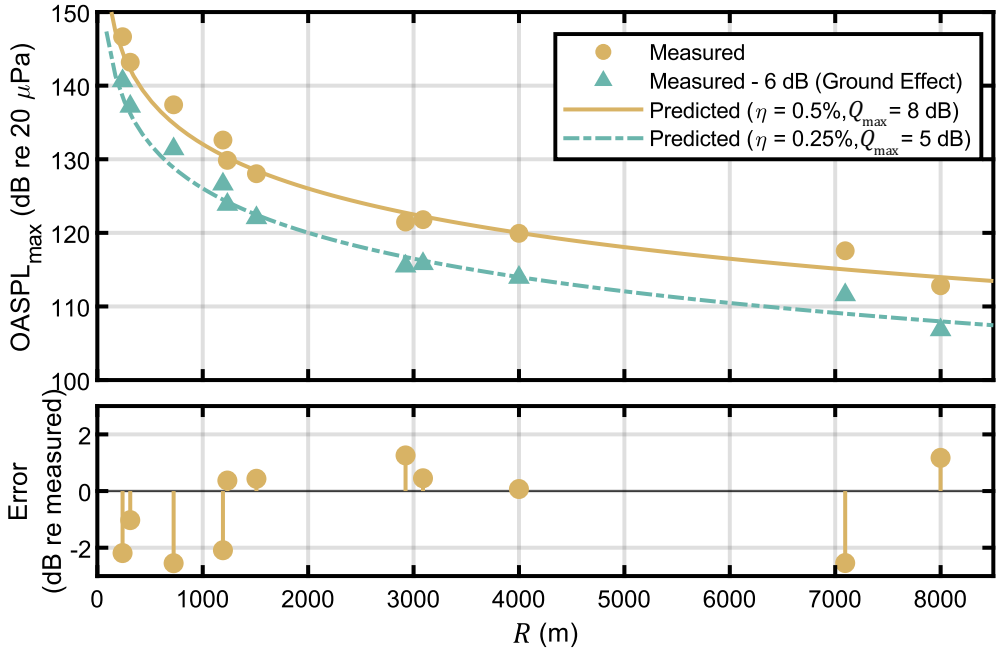

Figure 7. (Top) Maximum overall sound pressure levels as measured, compared with the prediction method of Eq. (1). Also shown are levels adjusted for ground effects and an adjusted prediction. (Bottom) Difference between measurement and prediction at each station.

Also shown in Fig. 7 are curves representative of a simple predictive method for $\mathrm{OASPL_{max}}$ of a rocket. The maximum overall sound pressure level of a launch vehicle at a given distance from the rocket may be approximated by the expression

$$OASPL_{max} = 10\,log_{10}\left(\frac{\eta W_m}{10^{-12}W}\right) - 20\,log_{10}(4\pi R^2) + Q_{max} \\ = OAPWL - 20\,log_{10}(4\pi R^2) + Q_{max}, \quad (1)$$

where η is an acoustic efficiency ($\eta = W_a/W_m$) and W_m is the mechanical power, taken to be approximately equal to $\frac{1}{2}TU_e$, where T is the total thrust and U_e is the engine exit velocity. In Eq. (1), R is the distance to the source which is the distance to the launch site. Assuming an overall angle of maximum radiation of 65°[1], the relationship between these variables can be expressed as $R = d/\sin 65°$.

This model, first applied to rocket noise by McInerny[18], combines three elements: the estimation of acoustic power from the mechanical power of the rocket by assuming an acoustic efficiency, accounting for spherical spreading (which gives the maximum overall sound pressure level for an equivalent monopole), and finally accounting for directionality by adding on a maximum directivity index $Q_{\max}$. Historically, an efficiency of $\eta = 0.5\%$ has been assumed with a maximum directivity index of $Q_{\max} = 8$ dB. However, accounting for ground reflections and applying a provisional decrease in measured pressures by a factor of two, the estimate for acoustic efficiency would then be reduced by a factor of two as well, which yields $\eta \approx 0.25\%$. This adjustment also affects the calculation of $Q_{\max}$, which would become $Q_{\max} = 5$ dB. Using these adjusted values, the predicted maximum overall sound pressure levels now match closely the measured data that has been adjusted for ground effects.

This model was also used earlier by Franken[19] for turbojet noise, however, the geometric spreading term differed by treating the radiation as a half-space problem ($2\pi R^2$, hemispherical spreading) instead of a free-space problem ($4\pi R^2$, spherical spreading) due to the presence of the ground. It is worth noting that the formulation in Eq. (1) makes no provision to correct for ground effects, but also treats the problem as free space (hence the $4\pi R^2$). If Eq. (1) is adjusted to half-space, this changes the value of $Q_{\max}$ to be 5 dB instead of 8 dB. Since the acoustic efficiency is a property of the source regardless of whether the half- or free-space problem is considered, we can conclude that $\eta \approx 0.25\%$. Hence, the maximum overall level without accounting for ground effects (half-space) becomes

$$OASPL_{max,half} = 10\,log_{10}\left(\frac{\eta W_m}{10^{-12}W}\right) - 20\,log_{10}(2\pi R^2) + Q_{max} \\ = OAPWL - 20\,log_{10}(2\pi R^2) + Q_{max}, \quad (2)$$

and the maximum overall level accounting for ground effects (free space) is

$$OASPL_{max,free} = 10\,log_{10}\left(\frac{\eta W_m}{10^{-12}W}\right) - 20\,log_{10}(4\pi R^2) + Q_{max} \\ = OAPWL - 20\,log_{10}(4\pi R^2) + Q_{max}. \quad (3)$$

In both cases, then, $\eta \approx 0.25\%$ and $Q_{\max} = 5$ dB, which reflects these quantities being fundamental source properties unaffected by the presence or absence of the ground.

The predicted values for $\text{OASPL}_{\max}$ underestimate the true level slightly on average. However, there is not a consistent bias visible in the error between the measurement and the prediction in Fig. 7. Generally, the model predicts $\text{OASPL}_{\max}$ accurately within a ±2.5 dB margin of error[i]. For a simplistic model that has no inclusion of propagation, nonlinear, or terrain effects, this performance is satisfactory. McInerny previously applied the same model across 5 rocket launches (4 distinct vehicles) with a considerably larger relative error of ±6.4 dB[ii].

To investigate potential azimuthal asymmetry effects on the overall maximum level, Table 2 shows the measured $\text{OASPL}_{\max}$ at each station, as well as the $\text{OASPL}_{\max}$ scaled for geometric spreading to a common distance of $100D_e = 202$ m from the source. Also shown is the scaled $\text{OASPL}_{\max}$ values relative to the average. There appears to be no apparent discernable bias in levels between $\tilde{\varphi} = 0°$ and 90° that is greater than the variation observed in each angular grouping.

Table 2. $OASPL_{max}$ and $OASPL_{max}$ scaled for geometric spreading to a common distance of $100D_e$.

Station	d (m)	R (m)	$\tilde{\varphi}$	$\text{OASPL}_{\max}$	$\text{OASPL}_{\max}$ (Scaled to $100D_e$)	dB re average $\text{OASPL}_{\max}$
1	217	239	0°	146.7	148.1	1.5
2	656	724	0°	137.4	148.5	1.9
3	2800	3090	0°	121.8	145.5	-1.1
4	1080	1192	45°	132.6	148.0	1.4
5	2650	2924	45°	121.5	144.7	-1.9
6	283	312	90°	143.2	147.0	0.4
7	1118	1234	90°	129.9	145.6	-1.0
8	1368	1509	90°	128.0	145.5	-1.1
9	3625	4000	90°	119.9	145.9	-0.7
10	7250	8000	30°	112.8	144.8	-1.8
11	6430	7095	30°	117.6	148.5	1.9

C. SPECTRAL CHARACTERISTICS

Representative third-octave band maximum launch noise spectra are shown in Fig. 8. The maximum spectra are generated from the region where the noise is within 3 dB of the maximum overall level. Results are shown for the mid-field (Fig. 8a) and far-field (Fig. 8b) at $\tilde{\varphi} = 0°$ and 90°. The levels of each spectrum have been adjusted for spherical spreading to a common radial distance of $100D_e = 202$ m. Visible in each spectrum is a high-frequency slope corresponding roughly to f^{-2} (-10 dB/decade in a one-third octave sense), which is understood to correspond to acoustic shocks in the time domain[20]. Noticeably, this slope rolls off in the far-field at around 2-3 kHz, whereas in

[i] Error max/min: +1.3/-2.5 dB, average (signed/absolute): -0.6/1.3 dB, rms: 1.6 dB; number of data points: 11.
[ii] Error max/min: +6.4/-4.7 dB, average (signed/absolute): 2.0/3.6 dB, rms: 4.0 dB; number of data points: 19.

the mid-field, the shock-correlated slope continues through 20 kHz. This is evidence of the evolution and decay of shocks from the mid- to far-field, where the shock strength has decayed as atmospheric absorption begins to dominate at the higher frequencies[21].

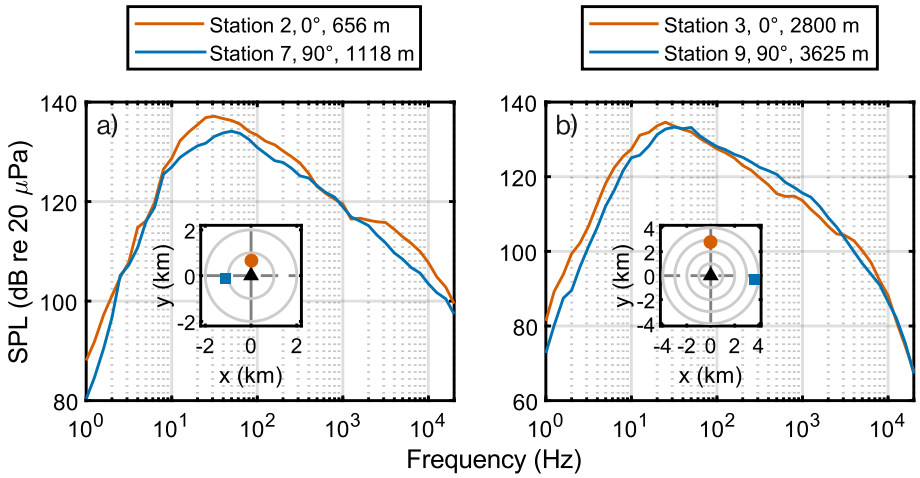

Figure 8. Spectra from 0° and 90° for a) mid- and b) far-field locations.

A noticeable feature in these spectra is the shifting in spectral peak frequency with azimuthal angle $\tilde{\varphi}$. The peak frequency at $\tilde{\varphi} = 90°$ occurs at a higher frequency than $\tilde{\varphi} = 0°$. This is summarized in Table 3, where the peak frequencies for all stations at $\tilde{\varphi} = 0°$ and $\tilde{\varphi} = 90°$ are shown.

Table 3. One-third-octave peak frequency for each station at $\tilde{\varphi} = 0°, 90°$.

Station	$\tilde{\varphi}$	f_{pk}
1	0°	40
2	0°	31.5
3	0°	25
6	90°	50
7	90°	50
8	90°	40
9	90°	31.5

If these observed changes in peak frequency are related to single plume/merged plume behavior at $\tilde{\varphi} = 90°$ and 0°, respectively, it would be expected that a Strouhal number scaling of the peak frequency could account for this effect since a characteristic diameter is included in the nondimensionalization. The classical Strouhal number used in jet noise is given by the expression

$$Sr = \frac{f D_c}{U_c}, \tag{4}$$

where f is the frequency, D_c is a characteristic diameter (typically taken to be D or D_j for jets), and U_c is a characteristic flow velocity (typically taken to be U_e or U_j for jets). If true merged-plume behavior is present at $\tilde{\varphi} = 0°$ (observing both plumes broadside), then the characteristic diameter should be $D_c = D_e = D\sqrt{2}$. Likewise, for an observer at $\tilde{\varphi} = 90°$, only one plume is visible with the other being shielded from view, so the characteristic diameter is expected to be that of just one nozzle $D_c = D$. Using these different characteristic diameters in calculating the mean and median peak Strouhal number for $\tilde{\varphi} = 0°$ and 90°, the results in Table 4 show that for both the mean and median frequencies, the calculated Strouhal numbers for $\tilde{\varphi} = 0°$ and 90° are nearly identical. This suggests that the shift in peak frequency does appear to be related to a change in characteristic diameter corresponding to single and merged-plume behavior. While this link is promising, more data are needed to strengthen this hypothesis.

Table 4. Mean and median one-third octave peak frequency at all sites for $\tilde{\varphi} = 0°, 90°$. Mean and median Strouhal numbers, computed using the indicated characteristic diameters are also shown.

$\tilde{\varphi}$	Mean(f_{pk})	Median(f_{pk})	D_c	Mean($\mathrm{Sr}_{\mathrm{pk}}$)	Median($\mathrm{Sr}_{\mathrm{pk}}$)
0°	32.2	31.5	$D_e = D\sqrt{2}$	0.0195	0.0191
90°	42.9	45	D	0.0184	0.0193

While the peak frequency noticeably shifts, the portions of the spectra above and below the peak frequency do not appear to shift to the same degree. Instead, at $\tilde{\varphi} = 0°$ a lower frequency "bump" is added to the spectrum, corresponding to the merged plume, which alters the peak frequency of the spectrum while keeping the remaining portions of the spectrum largely the same. This is especially visible in Fig. 8a. Coltrin et al.[22] noticed a similar phenomenon in a laboratory experiment, where as merged plume behavior began to dominate, a lower-frequency peak corresponding to the equivalent diameter appeared and began to dominate the single-nozzle frequency peak. This addition of a lower-frequency spectral peak also mirrors the two-zone model for clustered jets by Eldred et al.[7] and Kandula[8], which predicts a double-peaked spectrum for clustered jet flows. It is worth noting that this model incorporates no provisions for azimuthal variation. While the spectra shown in Fig. 8 do not appear to exhibit explicit double-peaked behavior, this could be due to the peaks not being well separated. Since the nozzles are relatively closely spaced on the Atlas V ($S/D \approx 1.14$), the radiation coming from the unmerged portion of the plume may be relatively weak as the plumes merge rather quickly; thus at $\tilde{\varphi} = 0°$, merged plume behavior with a lower characteristic frequency may dominate the higher frequency peak corresponding to unmerged (single) plume behavior. Further measurements are required to verify this theory.

4. CONCLUSION

An acoustical measurement of the Atlas V JPSS-2 launch has been conducted. Measurements were made at 11 stations, ranging in distance from 217 to 7250 m from the launch site at a variety of azimuthal angles. Significant asymmetry of the ignition overpressure peak sound pressure level was observed. This asymmetry corresponded to the flame trench orientation; the distance-scaled peak sound pressure level was observed to be up to ~30 dB higher at locations near the flame trench exit azimuth than those opposite this direction.

A simple directional source model predicted the maximum overall sound pressure level at all 11 sites accurately within ±2.5 dB. This model, accounting for ground effects, assumed an acoustic efficiency of $\eta \approx 0.25\%$ and a maximum directivity index of $Q_{\max} = 5$ dB.

During the launch, the maximum overall sound pressure level appeared to not correlate with the orientation of the nozzles with respect to the observer. However, where two nozzles were visible to the observer, the spectral peak frequency was lower. By applying Strouhal number scaling, the spectral peak frequencies were shown to correspond to single-plume behavior where only one nozzle was visible and combined-plume behavior where two nozzles were visible. This suggests that asymmetric clustered nozzle configurations may have different spectral characteristics depending on the orientation of the observer with respect to the nozzles. Further research into different nozzle configurations is warranted to quantify any possible effects.

ACKNOWLEDGMENTS

This research was supported in part by appointments of L. T. M. and M. C. A. to the Department of Defense (DOD) Research Participation Program administered by the Oak Ridge Institute for Science and Education (ORISE) through an interagency agreement between the U.S. Department of Energy (DOE) and the DOD. ORISE is managed by ORAU under DOE contract number DE-SC0014664. All opinions expressed in this paper are the author's and do not necessarily reflect the policies and views of DOD, DOE, or ORAU/ORISE.

REFERENCES

[1] Lubert, C. P., Gee, K. L., and Tsutsumi, S., "Supersonic jet noise from launch vehicles: 50 years since NASA SP-8072," *J. Acoust. Soc. Am.* **151**(2), 752-791 (2022). doi: 10.1121/10.0009160

[2] Jones, N., "Does the roar of rocket launches harm wildlife? These scientists seek answers," *Nature* **618**, 16-17 (2023). doi: 10.1038/d41586-023-01713-7

[3] Kantola, R. A., "Acoustic properties of heated twin jets," *J. Sound Vib.* **79**(1), 79-106 (1981). doi: 10.1016/0022-460X(81)90330-8

[4] Pineau, P., and Bogey, C., "Acoustic shielding and interaction effects for strongly heated supersonic twin jets," *AIP Advances* **11**, 075114 (2021). doi: 10.1063/5.0059789

[5] Greska, B., and Krothapalli, A., "A Comparative Study of Heated Single and Equivalent Twin Jets," *13th AIAA/CEAS Aeroacoustics Conference (28th AIAA Aeroacoustics Conference)*, 21-23 May 2007, Rome, Italy; AIAA 2007-3634. doi: 10.2514/6.2007-3634

[6] Bozak, R., "Twin Jet Effects on Noise of Round and Rectangular Jets: Experiment and Model," *20th AIAA/CEAS Aeroacoustics Conference*, 16-20 June 2014, Atlanta, GA, USA; AIAA 2014-2890. doi: 10.2514/6.2014-2890

[7] Eldred, K. M., White, R. W., Mann, M. A., and Cottas, M. G., "Suppression of Jet Noise With Emphasis on the Near Field," ASD-TDR-62-578, Wright-Patterson AFB, Ohio; DTIC Accession Number AD0299026 (1963).

[8] Kandula, M., "Near-field acoustics of clustered rocket engines," *J. Sound Vib.* **309**(3-5), 852-857 (2008). doi: 10.1016/j.jsv.2007.06.078

[9] Eldred, K. M., "Acoustic loads generated by the propulsion system," NASA SP-8072, Washington, D. C. (1971).

[10] Potter, R. C., and Crocker, M. J., "Acoustic Prediction Methods for Rocket Engines, Including the Effects of Clustered Engines and Deflected Exhaust Flow," NASA CR-566, Huntsville, AL (1966).

[11] Katorgin, B. I., Chvanov, V. K., Chelkis, F. J., Popp, M., Tanner, L. G., van Giessen, R. C., and Connaly, S. J., "RD-180 Engine Production and Flight Experience," *40th AIAA/ASME/SAE/ASEE Joint Propulsion Conference and Exhibit*, 11-14 July, Fort Lauderdale, FL, USA; AIAA 2004-3998 (2004). doi: 10.2514/6.2004-3998

[12] Cunningham, C. F., Anderson, M. C., Moats, L. T., Gee, K. L., Hart, G. W., Hall, L. K., and Campbell, S. C., "Acoustical measurement and analysis of an Atlas V launch without solid rocket boosters," *Proc. Mtgs. Acoust.,* in press (2022).

[13] Gee, K. L., Novakovich, D. J., Mathews, L. T., Anderson, M. C., and Rasband, R. D., "Development of a Weather-Robust Ground-Based System for Sonic Boom Measurements," NASA/CR-2020-5001870, Hampton, VA (2020).

[14] James, M. M., Salton, A., Calton, M., Downing, M., Gee, K. L., and McInerny, S. A., "Commercial Space Operations Noise and Sonic Boom Measurements," *National Academies of Sciences, Engineering, and Medicine*, Washington, D. C. (2020). doi: 10.17226/25834

[15] Anderson, M. C., Gee, K. L., Novakovich, D. J., Mathews, L. T., and Jones, J. T., "Comparing two weather-robust microphone configurations for outdoor measurements," *Proc. Mtgs. Acoust.* **42**, 040005 (2020). doi: 10.1121/2.0001561

[16] Gee, K. L., Hart, G. W., Cunningham, C. F., Anderson, M. C., Bassett, M. S., Mathews, L. T., Durrant, J. T., Moats, L. T., Coyle, W. L., Kellison, M. S., and Kuffskie, M. J., "Space Launch System acoustics: Far-field noise measurements of the Artemis-I launch," *JASA Express Lett.* **3**, 023601 (2023). doi: 10.1121/1.2369320

[17] Hart, G. W, and Gee, K. L., "Correcting for ground reflections when measuring overall sound power level and acoustic radiation efficiency of rocket launches," *Proc. Mtgs. Acoust.* **50**, 040004 (2022). doi: 10.1121/2.0001733

[18] McInerny, S. A., "Launch Vehicle Acoustics Part 1: Overall Levels and Spectral Characteristics," *Journal of Aircraft* **33**(3), 511-517 (1996). doi: 10.2514/3.46974

[19] Franken, P. A., "Jet Noise," in *Noise Reduction*, edited by L. L. Beranek (McGraw-Hill, New York), Chap. 24, pp. 644-666 (1960). See also Franken, P. A., "Review of Information on Jet Noise," *Noise Control* **4**, 8-16 (1958). doi: doi.org/10.1121/1.2369320

[20] Gurbatov, S. N., and Rudenko, O. V., "Statistical phenomena," in *Nonlinear Acoustics*, edited by M. F. Hamilton and D. T. Blackstock (Academic, San Diego), Chap. 13, pp. 377–398 (1998).

[21] Anderson, M. C., Gee, K. L., Cunningham, C. F., and Hart, G. W., "Analysis of nonlinear acoustic propagation from an Atlas V launch vehicle," *24th International Congress on Acoustics*, 24-28 October, Gyeongju, Korea (2022).

[22] Coltrin, I. S., Maynes, R. D., Blotter, J. D., and Gee, K. L., "Influence of nozzle spacing and diameter on acoustic radiation from supersonic jets in closely spaced arrays," Applied Acoustics **81**, 19-25 (2014). doi: 10.1016/j.apacoust.2014.01.008

Chapter 5

Methods for predicting overall sound power and maximum overall sound pressure levels from heated supersonic jets, including rockets

Prior work has resulted in models for estimating overall sound power levels (OAPWLs) and maximum overall sound pressure levels ($OASPL_{max}$) from jet and rocket engines. Based on fundamental flow properties, this chapter builds on previous results and presents simple methods for predicting OAPWL and $OASPL_{max}$ from heated supersonic jets and rockets. This chapter is an article published as L. T. Mathews and K. L. Gee, "Methods for predicting overall sound power and maximum overall sound pressure levels from heated supersonic jets, including rockets," *Journal of the Acoustical Society of America.* **158**(1), 371-379 (2025); https://doi.org/10.1121/10.0037192. It is reprinted in this dissertation under the terms of ASA's Transfer of Copyright Agreement, item 3 with the article cover page per ASA policy. I hereby confirm that the use of this article is compliant with all publishing agreements.

The Journal of the Acoustical Society of America

JULY 14 2025

Methods for predicting overall sound power and maximum overall sound pressure levels from heated supersonic jets, including rockets

Logan T. Mathews ; Kent L. Gee

J. Acoust. Soc. Am. 158, 371–379 (2025)
https://doi.org/10.1121/10.0037192

JASA ARTICLE

Methods for predicting overall sound power and maximum overall sound pressure levels from heated supersonic jets, including rockets

Logan T. Mathews[a] and Kent L. Gee[b]
Department of Physics and Astronomy, Brigham Young University, Provo, Utah 84602, USA

ABSTRACT:
Prior work [e.g., McInerny (1992). Noise Control Eng. J. **38**(1), 5–16; McInerny (1996). J. Aircraft **33**(3), 511–517; Franken (1958). Noise Control **4**(3), 8–16] has resulted in models for estimating overall sound power levels (OAPWLs) and maximum overall sound pressure levels ($OASPL_{max}$) from jet and rocket engines. Based on fundamental flow properties, this paper builds on previous results and presents simple methods for predicting OAPWL and $OASPL_{max}$ from heated supersonic jets and rockets. A method for estimating ground effects on $OASPL_{max}$ is also presented. The model's performance is evaluated for launched Atlas V and Vulcan Centaur rockets and an installed F404 jet engine at engine conditions ranging from 38% thrust through afterburner. The results show good agreement for $OASPL_{max}$, where the root mean square error is confined to less than 2 dB for the rockets and jet engine conditions considered. © *2025 Acoustical Society of America.*
https://doi.org/10.1121/10.0037192
(Received 29 March 2025; revised 6 June 2025; accepted 26 June 2025; published online 14 July 2025)
[Editor: Con Doolan] Pages: 371–379

I. INTRODUCTION

Numerous models exist for predicting the far-field radiated noise from supersonic jets and rockets. These models range from simple computations that can be performed on a scientific calculator to full-featured prediction suites, complete with graphical interfaces, that compute advanced noise metrics. Although the complex noise prediction software packages are appealing and useful, elementary models still retain merit. In particular, when fast, reasonably accurate basic metrics are needed, such models excel at providing predictions. Additionally, if these models are based on fundamental flow parameters, they can serve as a straightforward link between flow properties and noise characteristics. Such capabilities may be useful in noise reduction efforts. Furthermore, many advanced models build on the same methodologies as this simple model, such as calculating sound power and, hence, may benefit from advances in these computations.

More advanced models, such as "RUMBLE" (Bradley *et al.*, 2018) and "RNOISE" (Sutherland, 1993; Plotkin *et al.*, 2004; Plotkin, 2010) for rockets, and the Advanced Acoustic model (AAM; Page *et al.*, 2009), Aircraft NOise Prediction Program (ANOPP; NASA Langley Research Center, 2010), and the SAE ARP876F standard (SAE International, 2021) for jets provide advanced metrics, such as sound exposure levels with various weightings, and include numerous model inputs such as weather information and detailed vehicle trajectory. Whereas complex models such as these have great utility in community noise and environmental impact assessments, basic models such as that in this paper provide a quick, simple way to predict basic acoustic parameters. Additionally, advanced noise models do not always produce accurate results (Gee *et al.*, 2024), hence, further research into modeling is warranted.

This paper builds on similar models established by Franken (1958), Franken (1960), and McInerny (1996) by expanding into elementary flow parameters and adding a dedicated correction for ground effects for observers near the ground. Additionally, this model broadens its scope to supersonic air jets and rockets, as the aforementioned models focused on only one application regime. This model for maximum overall sound pressure levels ($OASPL_{max}$) is validated against modern, high-fidelity acoustic data from launched rockets and a full-scale installed jet engine. Because the methods presented in this paper form the basis for several widely used empirical noise models—such as NASA SP-8072 (Eldred, 1971) and its derivatives (e.g., Lubert *et al.*, 2022), "RUMBLE" and "RNOISE"—the discussion provided here is directly relevant to those models as well.

II. MODEL

Here, the predictive methodology is given in two main parts. First, overall sound power level (OAPWL) is estimated from elementary flow parameters. Second, $OASPL_{max}$ is calculated. A correction for ground effects is then outlined. Finally, the effects of using exit vs fully-expanded (FE) parameters for computing the overall sound power are quantified.

[a]Email: loganmathews@byu.edu
[b]Email: kentgee@byu.edu

A. OAPWL

To begin, the jet mechanical stream power, W_m, is expressed as

$$W_m = \frac{1}{2} F U_e \tag{1}$$

(Franken, 1958; Sutton and Biblarz, 2017; Walter, 2019), where F is the total jet thrust and U_e is the mean jet velocity at the nozzle exit. Thrust can be written in terms of jet and ambient fluid properties as

$$F = \dot{m}_e U_e + (P_e - P_0) A_e = \left[\rho_e U_e^2 + (P_e - P_0)\right] A_e \tag{2}$$

(Mattingly, 2006; Sutton and Biblarz, 2017), where $\dot{m}_e$ is the mass flow rate at the nozzle exit, P_e is the mean pressure at the nozzle exit, P_0 is the ambient pressure, A_e is the nozzle exit area, and ρ_e is the mean density at the nozzle exit. The first term, $\dot{m}_e U_e$, is known as the momentum thrust, and the second term, $(P_e - P_0)A_e$, is the pressure thrust. In the case of an ideally expanded jet, $P_e = P_0$, and the pressure thrust term goes to zero, leaving only the momentum thrust term. However, even when the jet is operating at imperfectly expanded conditions, the pressure thrust term is still relatively small (further quantification of this is provided in Sec. II D). Hence, the pressure thrust term is often discarded, and thrust is approximated as

$$F \approx \dot{m}_e U_e = \rho_e U_e^2 A_e. \tag{3}$$

Substituting this expression back into Eq. (1), the approximate mechanical power in terms of elementary flow properties is given as

$$W_m \approx \frac{1}{2} \rho_e U_e^3 A_e. \tag{4}$$

With the mechanical power defined, an acoustic efficiency parameter $\eta = W_a / W_m$ is introduced to relate the mechanical and acoustic powers (Lighthill, 1952), where W_a is the acoustic power. Historically, the acoustic efficiency of supersonic jets and rockets has been bounded in the range $0.1\% < \eta < 1\%$ (Eldred, 1971; Lubert *et al.*, 2022). Using the efficiency, the overall acoustic power can be given as

$$W_a = \eta W_m \approx \frac{1}{2} \eta \rho_e U_e^3 A_e = \frac{\pi}{8} \eta \rho_e U_e^3 D_e^2, \tag{5}$$

where D_e is the exit diameter, written in this form for convenience as diameter is often used instead of area. Because total acoustic power is typically formatted as a decibel quantity as the OAPWL, Eq. (5) is equivalent to

$$\begin{aligned} \mathrm{OAPWL} &= 10 \log_{10}\left(\frac{W_a}{W_{\mathrm{ref}}}\right) \approx 10 \log_{10}\left(\frac{\pi}{8 W_{\mathrm{ref}}} \eta \rho_e U_e^3 D_e^2\right) \\ &= 115.9 + 10 \log_{10}\left(\eta \rho_e U_e^3 D_e^2\right) \ \mathrm{dB}. \end{aligned} \tag{6}$$

This constitutes a compact formulation for calculating the overall acoustic power from elementary flow parameters. Given the simplicity of Eq. (6), it may be useful in applications that pursue optimizing/minimizing the acoustic power of a supersonic jet; as OAPWL is expressed in terms of these fundamental flow properties, it may be possible to determine which parameters can be altered to reduce the total jet sound power output while preserving thrust.

If the pressure thrust term is non-negligible, such as may be the case for significantly over- or underexpanded jets, OAPWL can be more accurately expressed as

$$\begin{aligned} \mathrm{OAPWL} = 115.9 + 10 \log_{10}\big(\eta U_e D_e^2 \big[\rho_e U_e^2 \\ + (P_e - P_0)\big]\big) \ \mathrm{dB}. \end{aligned} \tag{7}$$

In applications in which the thrust is known and density is unknown, it may be more useful to express OAWPL in terms of thrust, using Eq. (1), such that

$$\begin{aligned} \mathrm{OAPWL} &= 10 \log_{10}\left(\frac{W_a}{W_{\mathrm{ref}}}\right) \\ &= 117.0 + 10 \log_{10}(\eta F U_e) \ \mathrm{dB}. \end{aligned} \tag{8}$$

B. Maximum overall sound pressure level ($\mathrm{OASPL_{max}}$)

From the OAPWL, overall sound pressure levels (OASPLs) can then be estimated. This is performed by considering the source to be compact and directional. Whereas the aeroacoustic source of a jet is distributed, in the far-field, its behavior can be approximated as a simple source. Yet, how does the noise amplitude decay with distance? SP-8072 (Eldred, 1971) assumes spherical decay, as do McInerny (1996), Franken (1958), and Franken (1960). Given the shock-like content of supersonic jet and rocket noise waveforms, the noise amplitude decay can be bounded by spherical spreading and weak shock theory, which specify pressure amplitude decay rates of r^{-1} and $r^{-1}(\ln r)^{-1/2}$ (Blackstock *et al.*, 2024), respectively. Here, spherical spreading is considered; however, certain applications may benefit from adjustments to the decay rate, although it should be noted that a different spatial decay rate may modify the apparent acoustic efficiency and directivity index. For spherical spreading, the expression for OASPL at an observer point (r, θ, ϕ) is written as

$$\begin{aligned} \mathrm{OASPL}(r, \theta, \phi) \approx \mathrm{OAPWL} - 10 \log_{10}(4\pi r^2) \\ + Q_{\mathrm{OA}}(\theta, \phi), \end{aligned} \tag{9}$$

where r is the distance from the source to the receiver, θ is the angle between the source-to-receiver vector and the jet plume direction, ϕ is the source-to-receiver vector azimuthal angle, and $Q_{\mathrm{OA}}(\theta, \phi)$ are the overall source directivity indices. Although this calculation assumes spherical spreading from the source $(4\pi r^2)$, note that some models, such as those by Franken (1958) and Franken (1960), instead, implement hemispherical spreading $(2\pi r^2)$ to

https://doi.org/10.1121/10.0037192

account for a horizontally oriented jet on the ground plane, which is approximated as a half-space problem with incoherent ground reflections.

Jets and rockets are typically modeled as azimuthally symmetric sources, particularly when a single nozzle or tightly clustered nozzles are used. Under this assumption, the directivity index varies only with polar angle θ, denoted as $Q_{\mathrm{OA}}(\theta)$. Although modern rockets are often approximated as azimuthally symmetric, azimuthal asymmetries in jet and rocket noise remain an active area of research. Directivity indices can be measured experimentally or obtained from empirical models (Eldred, 1971; James *et al.*, 2014; Hart *et al.*, 2023). Whereas OASPL as a function of θ provides insight into the angular variation of noise, it is common practice to focus on the maximum directivity angle, $\theta_{\max}$, to characterize maximum overall sound levels. This metric is widely used in jet and rocket noise literature as a first-order indicator of maximum acoustic loading and commonly referenced in environmental assessments. In such cases, the directivity index can be simplified to its maximum value, $Q_{\max,\mathrm{OA}} = Q_{\mathrm{OA}}(\theta_{\max})$. Accordingly, the expression for $\mathrm{OASPL}_{\max}$ of an azimuthally symmetric source is given by

$$\mathrm{OASPL}_{\max}(r) \approx \mathrm{OAPWL} - 10\log_{10}(4\pi r^2) + Q_{\max,\mathrm{OA}}. \tag{10}$$

C. Ground effects

The expressions presented thus far for $\mathrm{OASPL}_{\max}$ assume a free-space problem with no ground effects. However, most observers in a jet noise problem will be located near a finite-impedance ground surface. Thus, in addition to the sound transmitted to the receiver directly, there will also be reflected sound that reaches the observer. The ground effect on the sound pressure level at the receiver is complicated and involves ray-path geometry, ground impedance, and noise frequency.

For a medium- to large-sized rocket, the peak frequency is typically quite low with most sound energy being constrained to frequencies below 40 Hz. Hart and Gee (2023) discussed the effect of reflections from a finite-impedance ground surface for rocket launches with observers near the ground. Their findings indicated that for most common surfaces (e.g., dirt, grass, and pavement), the ground would increase $\mathrm{OASPL}_{\max}$ by 5.5–6 dB relative to free-field conditions for rockets with a peak frequency < 60 Hz. This corresponds to $\mathrm{OASPL}_{\max}$ increasing by a factor of 1.9–2. This simplified method of accounting for ground effects uses a parameter δ that can be included in the model as

$$\mathrm{OASPL}_{\max}(r) \approx \mathrm{OAPWL} - 10\log_{10}(4\pi r^2) + Q_{\max,\mathrm{OA}} + 20\log_{10}(\delta), \tag{11}$$

where $\delta = 1$ for the free-space $\mathrm{OASPL}_{\max}$ and $\delta = 2$ for observers on a rigid ground surface. For higher frequency signals, such as jet aircraft engines (peak frequencies between 80 and 500 Hz depending on engine and operating condition), or for lower-impedance ground surfaces (such as soft snow), the factor may be less. For instance, Christian *et al.* (2023a) implemented a ground reflection model for a full-scale static jet measurement and elevated microphones over hard-packed dirt; their results indicate $1.7 < \delta < 1.2$ for a range of engine conditions, where the fully supersonic engine conditions are $1.2 < \delta < 1.3$. However, these were obtained for elevated microphones placed at 1.5 m above ground level. If comparing to ground-based measurements, δ will generally approach two. To this end, the sonic boom community has long used a ground reflection factor of 1.9 for ground-based measurements (Onyeowu, 1975).

To provide an estimation for values of δ, the methodology of Hart and Gee (2023) is followed here, with a few caveats. Instead of modeling the rocket noise spectrum as a simple "haystack" shape, this analysis uses a spectral shape with a broader peak, which is more representative of measured rocket noise. This was achieved by using a modified version of the empirical formula associated with noise from large-scale turbulence structures by Tam *et al.* (1996). Discussion of this modified empirical spectrum is given in Appendix A. The model of Embleton *et al.* (1983) is used to estimate the spectral ground effects at various values of effective flow resistivities. Figure 1(a) shows an example model spectrum with a peak frequency of 30 Hz (an upper bound for medium-lift class rockets) and three estimated, ground-affected spectra corresponding to ground surfaces with different effective flow resistivities (σ, in units of cgs rayls), each with receiver heights of 6 mm. For reference, $\sigma = 20$ corresponds to soft snow, $\sigma = 200$ corresponds to grass, and $\sigma = 100\,000$ corresponds to concrete (Embleton *et al.*, 1983). The effect on the OASPL of each spectrum and the correction factor, δ, are also displayed. Figure 1(b) shows the calculated values of δ for a wide range of spectral peak frequencies and values of σ. These values were computed assuming a receiver height of 6 mm.

D. Exit vs FE parameters

An important distinction to make is whether to use exit or equivalent FE jet parameters when estimating sound power. Some models specify which parameter to use, whereas others remain agnostic. Exact thrust and mechanical calculations, such as those in Eq. (2), employ exit parameters. However, in many situations, the parameters for the pressure thrust term are unknown and, hence, some have advocated for using FE parameters instead, which would not require the inclusion of pressure thrust (e.g., Varnier, 2001). Although it is impossible to quantify the difference between using exit and FE parameters for all jets, in general, the degree to which the difference will matter depends on the specific jet operating parameters—the closer to ideally expanded that a jet is, the less the difference between exit and FE parameters will be. As noted by Lubert *et al.* (2022), the question of whether to use exit or FE parameters remains unresolved. Therefore, a practical comparison of thrust and mechanical power calculated using both sets of parameters is presented here.

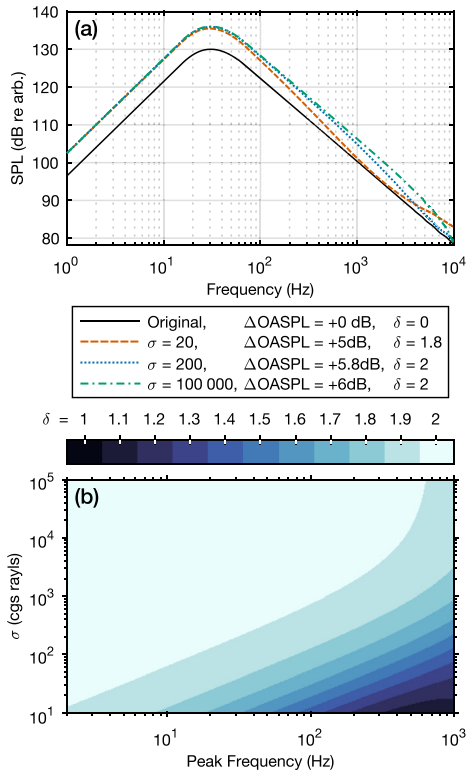

FIG. 1. (a) Sample spectrum with modeled ground effects for an observer 6 mm above the ground at three representative values of σ, and (b) estimated values of δ calculated for model spectra of varying peak frequencies and values of σ are shown.

To quantify the differences between exit and FE power calculations, Table I shows the difference for an afterburning military jet engine and several rockets. The estimation of parameters used in this analysis is discussed in Appendix B. In terms of thrust, the most accurate estimate is given using Eq. (2) with exit parameters. Using FE in place of exit parameters in Eq. (2) also yields accurate results. However, neglecting the pressure thrust term with exit conditions, as is the case with the simplified Eq. (3), yields appreciable thrust errors for the F404 engine at the two lowest engine powers but not for the rocket engines that are considered. It should be noted that these two lower engine conditions for the F404 are in the transonic regime.

In terms of mechanical (and acoustic) power, using the exact expressions of Eqs. (1) and (2) is accurate to within 0.1 dB for all engines and conditions. Aside from the 38% and 55% thrust conditions for the T-7A, the error in mechanical power for the approximate Eq. (4) with either exit for FE parameters is accurate to within 0.3 dB. Hence, whereas we recommend using the full equations with exit parameters whenever feasible, using approximated expressions for calculating the mechanical/acoustic power with either exit or FE parameters yields reasonable results, particularly for rockets.

E. Meteorological and propagation effects

Meteorological conditions can significantly influence noise propagation from jets and rockets, especially at greater distances from the source. Atmospheric absorption, wind, and refractive effects, such as curved-ray propagation, can all contribute to variability in received noise levels. Additionally, nonlinear propagation phenomena may further affect the acoustic signatures observed at far-field locations. Given the complexity and site-specific nature of these effects, a comprehensive treatment is beyond the scope of this work. However, the predictive model developed here can be used in conjunction with corrections from established propagation models—such as ray-tracing techniques and nonlinear acoustic models—which can be used to improve far-field accuracy when such refinements are needed.

III. VALIDATION

In the following examples, the models for OAPWL [Eqs. (6) and (7)] and $\mathrm{OASPL_{max}}$ [Eq. (11)] are validated for two types of supersonic jets: launched, medium-lift class rockets and a high-performance afterburner-capable jet engine. These two scenarios are representative of the types of applications this model is designed for.

A. Rockets

To validate the model for rockets, the predicted $\mathrm{OASPL_{max}}$ values are compared to those obtained through measurements from two liquid-fueled Atlas V 401 rocket launches from Space Launch Complex-3E (SLC-3E) at Vandenberg Space Force (VSFB), CA. Launch details and surface weather conditions for each launch are given in

TABLE I. Error in thrust and mechanical power calculated using exit conditions (exact and without pressure thrust terms), as well as with FE parameters for the F404 jet engine and Merlin 1D, RD-180, and BE-4 rocket engines.

			Thrust error (%)			Mechanical power error (dB)		
Vehicle	Engine	Condition	Eq. (2)	Eq. (3)	Eq. (2), FE	Eqs. (1) and (2)	Eq. (4)	Eq. (4), FE
T-7A	F404	38% thrust	0%	48%	3%	0.0	1.7	−1.4
T-7A	F404	55% thrust	1%	32%	2%	0.0	1.2	−1
T-7A	F404	MIL	1%	8%	1%	0.1	0.4	−0.3
T-7A	F404	AB	2%	11%	1%	0.1	0.4	−0.3
Falcon 9	Merlin 1D	100% thrust	1%	3%	0%	0.0	0.1	−0.1
Atlas V	RD-180	100% thrust	0%	4%	1%	0.0	0.2	−0.1
Vulcan/New Glenn	BE-4	100% thrust	1%	6%	3%	0.1	0.3	−0.1

https://doi.org/10.1121/10.0037192

TABLE II. Launch details and surface weather information for the three launches considered.

Vehicle and mission	Launch site	Launch date/ time (UTC)	Weather observation time	Temperature (°C)	Relative humidity (%)	Wind speed (m/s)	Wind direction (deg)	Cloud cover
Atlas V Landsat 9	VSFB, SLC-3E	27 Sep 2021, 18:12	L + 0:19	15	88	2.6	330	Overcast
Atlas V JPSS-2	VSFB, SLC-3E	10 Nov 2022, 09:49	L − 0:01	8	76	2.1	70	Clear
VC Cert-2	CCSFS, SLC-41	04 Oct 2024, 11:25	L + 0:00	27	87	1	104	Scattered

Table II. Further details for the Atlas V Landsat 9 and JPSS-2 launches are given by Cunningham *et al.* (2023) and Mathews *et al.* (2023), respectively. Furthermore, the model is validated against a recent measurement of the Vulcan Centaur (VC) Cert-2 launch from Space Launch Complex-41 (SLC-41) at Cape Canaveral Space Force Station (CCSFS), FL. This rocket used liquid engines and solid rocket motors. OASPL values were computed from measured waveforms using 1-s blocks with 50% overlap. For the model input parameters, estimations were made from publicly available data and computational tools, which is discussed in Appendix B and are reported in Table III. The acoustic efficiency is assumed to be $\eta = 0.33\%$ per the findings of Kellison and Gee (2023). To account for ground effects, a value of $\delta = 1.9$ is chosen based on Fig. 1, given the measurements were largely made on either dirt or a vegetated surface, and the rocket peak frequencies are <30 Hz. $Q_{\max,\mathrm{OA}}$ is chosen to be 5 dB, based on the findings of McInerny (1996), although it should be noted that this parameter deserves more study. Notably, McInerny (1996) used $Q_{\max,\mathrm{OA}}$ values of 5 dB to estimate average levels across the 6 dB re maximum region and 8 dB for estimating maximum 1-s block averaged $\mathrm{OASPL}_{\max}$ values. However, ground effects were not separately accounted for in the model by McInerny (1996). When accounting for ground effects separately, such as in Eq. (11), $Q_{\max,\mathrm{OA}}$ reduces from 8 to 5 dB.[1]

The resulting predictions, compared with measured values, are reported in Fig. 2 as a function of approximate distance from the source. This distance is approximated by assuming a nominal maximum emission angle of 71° for the Atlas V based on the findings of Mathews *et al.* (2021) for the Falcon 9,[2] as the RD-180 engines of the Atlas V use the same propellant as and have similar performance to the Merlin 1D engines of Falcon 9. Furthermore, a recently proposed convective Mach number model by Gee *et al.* (2025) estimates the peak directivity angle as $\theta_{\max} \approx \cos^{-1}[(c_0/U_e)^{1/2}]$, which also yields $\theta_{\max} \approx 71°$. For the VC vehicle, this is somewhat more complicated as there are two types of engines. Following the methods of Kellison *et al.* (2024) for the Space Launch System rocket, another vehicle with liquid engines and solid rocket motors, a maximum emission angle is estimated to be 69° for the VC2 configuration. The resulting predictions for $\mathrm{OASPL}_{\max}$ from the Atlas V launches in Fig. 2(a) shows good agreement, generally, where the root mean square error (RMSE) is confined to less than 1.8 dB between measurement and prediction.

Interestingly, Fig. 2(a) shows two different data trends, which are grouped by launch. The JPSS-2 launch fits the linear, spherical decay rate (r^{-1}, –20 dB/decade) of Eq. (11) well. However, the Landsat 9 $\mathrm{OASPL}_{\max}$ values appear to decay faster. As mentioned in Sec. II B, weak shock theory would predict a decay rate of $r^{-1}(\ln r)^{-1/2}$ (Blackstock *et al.*, 2024). In the far-field, this approximates to $r^{-1.1}$ (–22 dB/decade; ANSI/ASA, 2011), which is indicated by the gray dashed line. It appears that the Landsat 9 $\mathrm{OASPL}_{\max}$ values follow this decay rate. Although a thorough investigation into the cause of this discrepancy is beyond the scope of this paper, one hypothesis is proposed here. At the respective launches, the surface weather conditions indicated 15 °C/88% relative humidity (RH) and 8 °C/76% RH for Landsat 9 and JPSS-2, respectively. Additionally, the Landsat 9 launch had overcast conditions with dense fog, whereas the JPSS-2 launch was clear. The increased atmospheric humidity at ground level and in the atmosphere at the Landsat 9 launch would decrease absorption (ANSI/ASA, 2009), leading to more shock-like waveforms that would decay closer to weak shock theory.

For the VC Cert-2 launch, depicted in Fig. 2(b), a different trend emerges. Using the same values of η, $Q_{\max,\mathrm{OA}}$, and δ reveals a general overprediction of measured values by 3 dB, which is indicated by the solid line. However, if η is halved (resulting in an acoustic efficiency of 0.17%), the fit is substantially improved with a RMSE of 1.7 dB. This suggests that the acoustic efficiency of the VC2 vehicle is lower than that of the Atlas V 401. One postulate for this discrepancy is that the separated plumes of the VC2 vehicle result in a lower acoustic efficiency than the tightly clustered plumes of the Atlas V 401. Further research is necessary to establish the cause of this apparent difference in acoustic efficiency between these two vehicles.

TABLE III. Estimated plume parameters for the Atlas V 401 and VC VC2 rockets.

Vehicle	Engine/motor	Number	Component total		Vehicle total	
			F (MN)	W_m (GW)	F (MN)	W_m (GW)
Atlas V 401	RD-180	1	3.83	6.06	3.83	6.06
VC VC2	BE-4	2	4.90	7.80	9.02	12.9
	GEM 63XL	2	4.12	5.09		

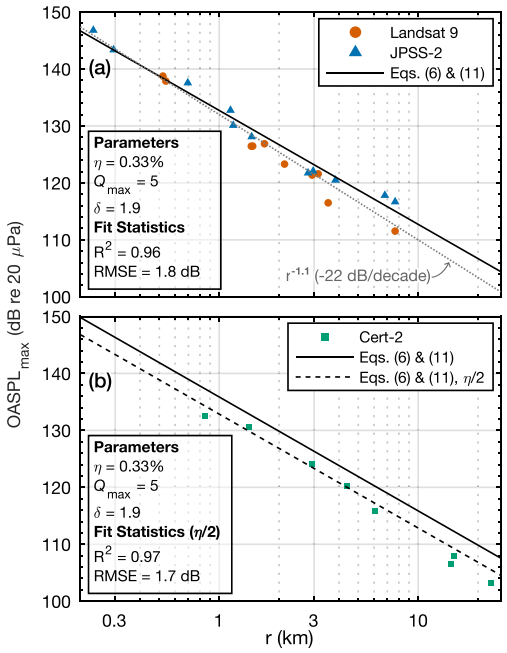

FIG. 2. (a) $OASPL_{max}$ as measured for two different Atlas V launches compared to predictions via Eqs. (6) and (11), and (b) $OASPL_{max}$ for a VC launch compared to predictions via Eqs. (6) and (11) for two different values of acoustic efficiency are shown.

B. Full-scale, afterburner-capable jet engine

To extend the validation regime beyond rockets, the model is applied to the GE F404, a full-scale jet engine capable of afterburning operation. The data are from a 2019 measurement of the T-7A trainer aircraft, details of which can be found in Leete *et al.* (2021). The model is applied at four different operating conditions: 38% thrust, 56% thrust, MIL ("military" power, 100% non-afterburning thrust), and maximum afterburner (AB, 152% thrust). As reported by Christian *et al.* (2023a), the FE Mach numbers at these conditions are 0.94, 1.1, 1.43, and 1.46, hence, the data represent engine conditions ranging from transonic to supersonic.

As more detailed jet parameters are available for this application (see Appendix B), the full, pressure thrust-inclusive model of Eqs. (7) and (11) is used and compared to the approximated, pressure thrust neglecting model, consisting of Eqs. (6) and (11). Additionally, condition-specific model parameters are used, which are shown in Table IV. Values for η are from the results of Christian *et al.* (2023b) and values of δ are determined from the ground reflection correction results at each engine condition's peak directivity angle by Christian *et al.* (2023a). Q_{max} values are determined from a refined methodology of Christian *et al.* (2022). The primary reasons for δ values being lower than the rocket example in Sec. III A are that the peak frequencies are significantly higher (100–500 Hz), and the jet measurements were made 1.5 m off the ground.

The jet parameters are used to compare the model against data measured at elevated microphones. Figure 3(a) shows the measurement locations for each engine condition analyzed here. These locations are chosen to align with the peak directivity angle at each engine condition, as specified by Gee *et al.* (2025). The measured and predicted $OASPL_{max}$ for the four engine conditions at various distances are shown in Fig. 3(b). Markers indicate the average $OASPL_{max}$ values for all six engine runups while bars indicate the measurement $OASPL_{max}$ variability across the runups. Notably, the spread in measured $OASPL_{max}$, particularly at greater propagation distances, is substantial—showing variability of up to ±3 dB from the mean. Streeter *et al.* (2024) investigated this variability and attributed it primarily to changes in meteorological conditions during the measurement period. Engine conditions were reproduced with high accuracy, exhibiting expected thrust variations of less than 0.5%.[3] Because the observed variability increases with propagation distance, meteorological factors are the most likely source of the differences. Comparing to the

TABLE IV. Values of parameters η, Q_{max}, and δ used for the T-7A/F404 engine at the four engine conditions.

Engine condition	η	Q_{max}	δ
38% Thrust	0.014%	7.4 dB	1.68
56% Thrust	0.19%	7.5 dB	1.23
MIL (100% thrust)	0.51%	7.0 dB	1.21
AB (152% thrust)	0.61%	5.9 dB	1.29

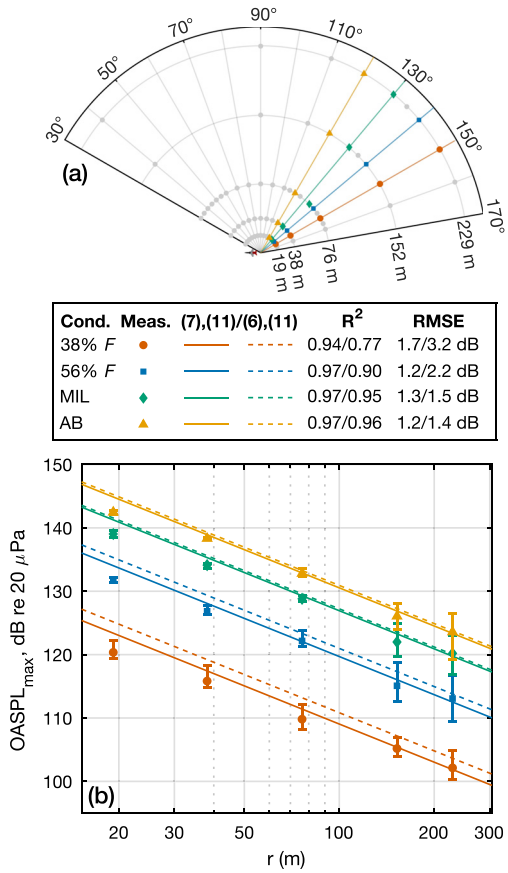

FIG. 3. (a) Measurement locations for peak directivity angles at four T-7A/F404 engine conditions, (b) measured $OASPL_{max}$ compared to predictions at four T-7A/F404 engine conditions with full [Eqs. (7) and (11)] and approximated [Eqs. (6) and (11)] models are shown. Markers indicate the average $OASPL_{max}$ values for all six engine runups while bars indicate the measurement $OASPL_{max}$ variability across the runups.

https://doi.org/10.1121/10.0037192

measurements, the full model for $OASPL_{max}$, consisting of Eqs. (7) and (11), shows excellent agreement across all engine conditions with RMSE < 1.7 dB. When the lowest engine condition is excluded, the RMSE improves to <1.3 dB. For each engine condition, the near-field measurements at 19 m appear to be outliers. The approximated expressions, consisting of Eqs. (6) and (11), are less accurate, particularly for the two lowest engine conditions, with the RMSE growing to 3.2 dB at the lowest condition. However, at MIL and AB, the RMSE for the approximate model is less than 1.5 dB.

IV. CONCLUSION

Models for overall sound power and maximum overall sound pressure levels from supersonic heated supersonic jets, such as jet engines and rockets, have been formulated and demonstrated. A simple method for accounting for near-ground effects is outlined, based on a model spectrum designed to replicate the spectral shapes of supersonic jet noise and rocket noise in the peak radiation direction. The effects of neglecting pressure thrust and those using FE jet parameters instead of exit parameters are quantified for a jet engine at various operating conditions, as well as for several rockets.

The model predicts measured maximum sound levels well for three launched rockets and an installed jet engine at four operating powers, with a RMSE generally less than 2 dB. Different apparent decay rates in maximum overall sound pressure levels are observed between two launches of the same rocket type, indicating possible differences caused by atmospheric conditions. It is noted that to accurately predict the levels for the VC Cert-2 launch, the acoustic efficiency used in the model must be a factor of 2 less than that for the Atlas V 401 vehicle, assuming the maximum overall directivity indices are the same. To improve this and other modeling approaches, further research into the acoustic efficiencies, maximum overall directivity indices, and spatial noise decay rates of jets and rockets are warranted.

ACKNOWLEDGMENTS

The authors thank Mark C. Anderson for his measurements of the VC rocket used in this study. This research was supported in part by the appointment of L.T.M. and Mark C. Anderson to the Department of Defense (DOD) Research Participation Program administered by the Oak Ridge Institute for Science and Education (ORISE) through an interagency agreement between the U.S. Department of Energy (DOE) and the DOD. ORISE is managed by Oak Ridge Associated Universities (ORAU) under DOE Contract No. DE-SC0014664. All opinions expressed in this paper are those of the authors and do not necessarily reflect the policies and views of DOD, DOE, or ORAU/ORISE. The authors acknowledge the Office of Naval Research for funding the T-7A analysis under Grant No. N00014-21-1-2069 with project monitor Steven Martens, Code 351 Jet Noise Reduction. The T-7A measurements were funded through the Advanced Pilot Training System Program Office and Air Force Research Laboratory. The Atlas V measurements were supported in part by Vandenberg Space Force Base through the United States Army Corps of Engineers. Space Launch Delta 30 at Vandenberg Space Force Base is acknowledged for logistical support. Distribution Statement A, approved for public release; distribution unlimited, cleared 28 March 2025.

AUTHOR DECLARATIONS

Conflict of Interest

The authors have no conflicts to disclose.

DATA AVAILABILITY

The data that support the findings of this study are available from the United States Department of Defense (United States Air Force/Space Force/Navy). Restrictions apply to the availability of these data, which were used under license for this study. Data are available from the authors upon reasonable request and with the permission of the United States Department of Defense (United States Air Force/Space Force/Navy).

APPENDIX A: MODEL SPECTRA

To estimate ground effects on measured spectra, a model spectrum was constructed. This was achieved empirically by modifying the large-scale turbulence similarity spectra of Tam *et al.* (1996). Although this similarity spectrum is widely applied in jet noise, Lubert *et al.* (2022) discuss that the spectral shape disagrees with measured spectra at peak radiation angles from supersonic jets and rockets, particularly the high-frequency slope. To this end, the large-scale similarity spectrum equation from Tam *et al.* (1996) is modified here to have a low-frequency slope of $f^{2.5}$ (25 dB/decade) and a high-frequency slope of $f^{-2.2}$ (–22 dB/decade) to approximate the spectral shapes of supersonic jets and rockets. This modified equation is given as

$$S(f,f_{pk}) = \begin{cases} 3.82974 - 22\log_{10}\left(\frac{f}{f_{pk}}\right) & \text{if } \frac{f}{f_{pk}} \geq 2.5, \\ \left[1.06617 - 42.2994\log_{10}\left(\frac{f}{f_{pk}}\right) + 21.40972\log_{10}\left(\frac{f}{f_{pk}}\right)^2\right], & \\ \log_{10}\left(\frac{f}{f_{pk}}\right) & \text{if } 2.5 > \frac{f}{f_{pk}} \geq 1, \\ -50.19338\log_{10}\left(\frac{f}{f_{pk}}\right)^2, & \\ -16.91175\log_{10}\left(\frac{f}{f_{pk}}\right)^3 & \text{if } 1 > \frac{f}{f_{pk}} \geq 0.5, \\ 3.43861 + 25\log_{10}\left(\frac{f}{f_{pk}}\right) & \text{if } \frac{f}{f_{pk}} < 0.5. \end{cases} \tag{A1}$$

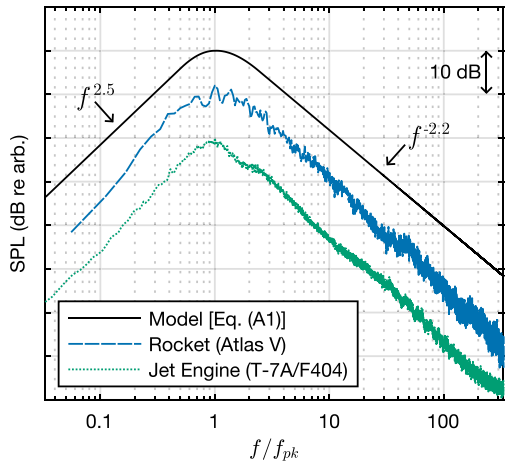

FIG. 4. Model spectrum from Eq. (A1) compared with measured maximum spectra from the Atlas V 401 rocket and the T-7A aircraft at afterburner, normalized relative to the peak frequency, is shown.

This empirical spectral shape is depicted in Fig. 4, alongside representative peak directivity spectra from a launched Atlas V 401 rocket and the T-7A/F404 jet at afterburner. The modified high- and low-frequency slopes closely approximate those of the rocket and supersonic jet engines.

APPENDIX B: JET PARAMETER CALCULATION

Rocket engine parameters are estimated using the NASA CEARUN program (McBride and Gordon, 2004), based on publicly available input parameters for the engines (Katorgin *et al.*, 2004; United Launch Alliance, 2010, 2023). These parameters are summarized in Table V.

Parameters for the GEM 63XL solid rocket motors are based on specifications from Northrop Grumman (2024). The exit velocity for the GEM 63XL motor is estimated from the reported vacuum specific impulse as reported by Northrop Grumman (2024). Given that the exit velocity is expected to differ for a sea-level launch, the exit velocity at launch is estimated by assuming a 10% reduction in specific impulse from vacuum to sea level based on Space Shuttle solid rocket motor performance specifications (Ward, 2010). This gave an approximate sea-level value of $U_e \approx 2.47$ km/s, which is close to that reported for the Space Shuttle solid rocket motor (McInerny, 1992; Ward, 2010).

TABLE V. Input parameters for CEARUN computation of RD-180 and BE-4 engines.

Parameter	RD-180	BE-4
Ambient pressure (kPa)	101.3	101.3
Chamber pressure (MPa)	25.66	13.4
Area ratio	36.87	23.3
Oxidizer/Fuel ratio	2.72	3.5
Fuel	RP-1	CH4(L)
Oxidizer	02(L)	02(L)
Run condition	Frozen, NFZ = 2	Frozen, NFZ = 2

The T-7A/F404 engine parameters were estimated using the Numerical Propulsion System Simulation (NPSS) code (Southwest Research Institute, 2025) using the recorded engine settings from the study and the measured ambient atmospheric conditions.

[1]For a perfectly rigid surface and ground-based observer, $\mathrm{OASPL}_{\max}$ increases by 6 dB and OAPWL increases by 3 dB relative to free-field. Given that $Q_{\max,\mathrm{OA}} = \mathrm{OASPL}_{\max}(r) + 10\log_{10}(4\pi r^2) - \mathrm{OAPWL}$, this means that separately accounting for ground effects results in $Q_{\max,\mathrm{OA}}$ being 3 dB lower than when ground effects are "baked into" the calculation.

[2]Mathews *et al.* (2021) initially found that the maximum directivity angle for the Falcon 9 rocket across three launches was 64°, however, subsequent improvements to their processing code (calculating the true three-dimensional angle to the rocket as opposed to just a two-dimensional approximation) have yielded a more accurate estimation of 71°. The Atlas V 401 and Falcon 9 are propelled by engines using the same fuel/oxidizer mixture, hence, using this result is justified.

[3]In terms of mechanical/acoustic powers, a 0.5% variation in thrust would constitute a 0.02 dB difference, assuming that the exit velocity does not change. Even in a more extreme, worst-case scenario, where the power changes by 5%, this would only result in a difference of 0.2 dB in acoustic output, which is significantly smaller than the variability observed.

ANSI/ASA (**2009**). S1.26-1995, *Calculation of the Absorption of Sound by the Atmosphere* (Acoustical Society of America, New York).
ANSI/ASA (**2011**). S2.20-1983, *Estimating Air Blast Characteristics for Single Point Explosions in Air, with a Guide to Evaluation of Atmospheric Propagation and Effects* (Acoustical Society of America, New York).
Blackstock, D. T., Hamilton, M. F., and Pierce, A. D. (**2024**). "Progressive waves in lossless and lossy fluids," in *Nonlinear Acoustics*, edited by M. F. Hamilton and D. T. Blackstock (Springer, Cham, Switzerland), pp. 63–147.
Bradley, K. A., James, M. M., Salton, A. R., and Boeker, E. R. (**2018**). *Commercial Space Operations Noise and Sonic Boom Modeling and Analysis* (National Academies of Sciences, Engineering, and Medicine Transportation Research Board, Washington, DC).
Christian, M. A., Gee, K. L., Streeter, J. B., Mathews, L. T., Wall, A. T., Johnson, J. P., and Campbell, S. C. (**2022**). "Installed F404 engine noise source characteristics from far-field directivity measurements," in *28th AIAA/CEAS Aeroacoustics Conference*, 14–17 June, Southampton, UK, AIAA Paper 2022–3027.
Christian, M. A., Gee, K. L., Streeter, J. B., Wall, A. T., and Campbell, S. C. (**2023a**). "Implementing a heuristic method to correct ground reflection effects observed in full-scale tactical aircraft noise measurements," Proc. Mtgs. Acoust. **50**(1), 040005.
Christian, M. A., Gee, K. L., Streeter, J. B., Wall, A. T., and Campbell, S. C. (**2023b**). "Sound power and acoustic efficiency of an installed GE F404 jet engine," JASA Express Lett. **3**(7), 073601.
Cunningham, C., Anderson, M. C., Moats, L. T., Gee, K. L., Hart, G. W., and Hall, L. K. (**2023**). "Acoustical measurement and analysis of an Atlas V launch," Proc. Mtgs. Acoust. **46**(1), 045005.
Eldred, K. M. (**1971**). "Acoustic loads generated by the propulsion system," National Aeronautics and Space Administration SP–8072, available at https://ntrs.nasa.gov/citations/20110012036 (Last viewed June 1, 2025).
Embleton, T. F. W., Piercy, J. E., and Daigle, G. A. (**1983**). "Effective flow resistivity of ground surfaces determined by acoustical measurements," J. Acoust. Soc. Am. **74**(4), 1239–1244.
Franken, P. A. (**1958**). "Review of information on jet noise," Noise Control **4**(3), 8–16.
Franken, P. A. (**1960**). "Jet noise," in *Noise Reduction*, edited by L. L. Beranek (McGraw-Hill, New York), pp. 644–666.
Gee, K. L., Olaveson, T. W., and Mathews, L. T. (**2025**). "Convective Mach number and full-scale supersonic jet noise directivity," AIAA J. **63**(4), 1393.
Gee, K. L., Pulsipher, N. L., Kellison, M. S., Mathews, L. T., Anderson, M. C., and Hart, G. W. (**2024**). "Starship super heavy acoustics: Far-field noise measurements during launch and the first-ever booster catch," JASA Express Lett. **4**(11), 113601.

Hart, G. W., and Gee, K. L. (**2023**). "Correcting for ground reflections when measuring overall sound power level and acoustic radiation efficiency of rocket launches," Proc. Mtgs. Acoust. **50**(1), 040004.
Hart, G. W., Gee, K. L., and Cook, M. R. (**2023**). "Corrected frequency-dependent directivity indices for large solid rocket motors," Proc. Mtgs. Acoust. **51**(1), 040007.
James, M. M., Salton, A. R., Gee, K. L., Neilsen, T. B., McInerny, S. A., and Kenny, R. J. (**2014**). "Modification of directivity curves for a rocket noise model," Proc. Mtgs. Acoust. **18**(1), 040008.
Katorgin, B. I., Chvanov, V. K., Chelkis, F. J., Popp, M., Tanner, L. G., van Giessen, R. C., and Connally, S. J. (**2004**). "RD-180 engine production and flight experience," in *40th AIAA/ASME/SAE/ASEE Joint Propulsion Conference and Exhibit*, 11–14 July, Fort Lauderdale, FL, AIAA Paper 2004–3998.
Kellison, M. S., and Gee, K. L. (**2023**). "Sound power of NASA's lunar rockets: Space Launch System versus Saturn V," JASA Express Lett. **3**(11), 113601.
Kellison, M. S., Gee, K. L., Coyle, W. L., Anderson, M. C., Mathews, L. T., and Hart, G. W. (**2024**). "Aeroacoustic analysis of NASA's Space Launch System Artemis-I mission," in *30th AIAA/CEAS Aeroacoustics Conference*, 4–7 June, Rome, Italy, AIAA Paper 2024–3033.
Leete, K. M., Vaughn, A. B., Bassett, M. S., Rasband, R. D., Novakovich, D. J., Gee, K. L., Campbell, S. C., Mobley, F. S., and Wall, A. T. (**2021**). "Jet noise measurements of an installed GE F404 engine," in *AIAA Scitech 2021 Forum*, 11–15 and 19–21 January, virtual event, AIAA Paper 2021–1638.
Lighthill, M. J. (**1952**). "On sound generated aerodynamically I. General theory," Proc. R. Soc. London, Ser. A: Math. Phys. Sci. **211**(1107), 564–587.
Lubert, C. P., Gee, K. L., and Tsutsumi, S. (**2022**). "Supersonic jet noise from launch vehicles: 50 years since NASA SP-8072," J. Acoust. Soc. Am. **151**(2), 752–791.
Mathews, L. T., Anderson, M. C., Gardner, C. D., McLaughlin, B. W., Hinds, B. M., McCullah-Boozer, M. R., Hall, L. K., and Gee, K. L. (**2023**). "An overview of acoustical measurements made of the Atlas V JPSS-2 rocket launch," Proc. Mtgs. Acoust. **51**(1), 040003.
Mathews, L. T., Gee, K. L., and Hart, G. W. (**2021**). "Characterization of Falcon 9 launch vehicle noise from far-field measurements," J. Acoust. Soc. Am. **150**(1), 620–633.
Mattingly, J. D. (**2006**). *Elements of Propulsion: Gas Turbines and Rockets* (American Institute of Aeronautics and Astronautics, Reston, VA).
McBride, B. J., and Gordon, S. (**2004**). "CEARUN," available at https://cearun.grc.nasa.gov/ (Last viewed June 1, 2025).
McInerny, S. A. (**1992**). "Characteristics and predictions of far-field rocket noise," Noise Control Eng. J. **38**(1), 5–16.
McInerny, S. A. (**1996**). "Launch vehicle acoustics. I—Overall levels and spectral characteristics," J. Aircraft **33**(3), 511–517.
NASA Langley Research Center (**2010**). "Aircraft NOise Prediction ProgramExternal," available at https://software.nasa.gov/software/LAR-19861-1 (Last viewed June 1, 2025).
Northrop Grumman (**2024**). "Propulsion products catalog," available at https://www.prd.ngc.agencyq.site/wp-content/uploads/NG-Propulsion-Products-Catalog.pdf (Last viewed June 1, 2025).
Onyeowu, R. O. (**1975**). "Diffraction of sonic boom past the nominal edge of the corridor," J. Acoust. Soc. Am. **58**(2), 326–330.
Page, J. A., Wilmer, C., Schultz, T., Plotkin, K. J., and Czech, J. (**2009**). "Advanced acoustic model technical reference and user manual," Technical Report SERDP Project WP-1304, available at https://apps.dtic.mil/sti/citations/ADA536390 (Last viewed June 1, 2025).
Plotkin, K. J. (**2010**). "A model for the prediction of community noise from launch vehicles," J. Acoust. Soc. Am. **127**(3 Supplement), 1773.
Plotkin, K. J., Sutherland, L. C., and Moudou, M. (**2004**). "Prediction of rocket noise footprints during boost phase," in *3rd AIAA/CEAS Aeroacoustics Conference*, 12–14 May, Atlanta, GA, AIAA Paper 1997–1660.
SAE International (**2021**). "Gas turbine jet exhaust noise prediction," SAE International Standard, available at https://www.sae.org/standards/content/arp876f/ (Last viewed June 1, 2025).
Southwest Research Institute (**2025**). "Numerical Propulsion System Simulation (NPSS)," available at https://software.nasa.gov/software/LAR-19861-1 (Last viewed June 1, 2025).
Streeter, J. B., Olaveson, T. W., Christian, M. A., Gee, K. L., Wall, A. T., and Campbell, S. C. (**2024**). "Assessing impact of near-ground meteorology on spectral variability in static jet aircraft noise measurements," Proc. Mtgs. Acoust. **50**(1), 040010.
Sutherland, L. C. (**1993**). "Progress and problems in rocket noise prediction for ground facilities," in *15th AIAA Aeroacoustics Conference*, 25–27 October, Long Beach, CA, AIAA Paper 1993–4383.
Sutton, G. P., and Biblarz, O. (**2017**). *Rocket Propulsion Elements*, 9th ed. (Wiley, New York).
Tam, C., Golebiowski, M., and Seiner, J. (**1996**). "On the two components of turbulent mixing noise from supersonic jets," in *Aeroacoustics Conference*, 6–8 May, State College, PA, AIAA Paper 1996–1716.
United Launch Alliance (**2023**). "Vulcan Launch Systems User's Guide," available at https://www.ulalaunch.com/docs/default-source/default-document-library/2023_vulcan_user_guide.pdf?sfvrsn=37856b50_1 (Last viewed June 1, 2025).
United Launch Alliance (**2010**). "Atlas V Launch Services User's Guide," available at https://www.ulalaunch.com/docs/default-source/rockets/atlasvusersguide2010a.pdf?fvrsn=f84bb59e_2 (Last viewed June 1, 2025).
Varnier, J. (**2001**). "Experimental study and simulation of rocket engine freejet noise," AIAA J. **39**(10), 1851–1859.
Walter, U. (**2019**). *Astronautics: The Physics of Space Flight* (Springer, New York).
Ward, T. A. (**2010**). *Aerospace Propulsion Systems* (Wiley, New York).

Chapter 6

SATURN: A Modern Empirical Model for Predicting Rocket Launch Noise

Abstract

Rocket launches generate intense, sustained noise with impacts on payloads, infrastructure, environmental assessments, and nearby communities. Accurate launch noise models are essential for predicting acoustic impacts and informing engineering design and environmental assessments. Legacy models like NASA SP-8072 rely on mid-20th-century data and propagation modeling, while other modern tools are closed-source. This paper introduces SATURN (Scientific Acoustic Tool for Understanding Rocket Noise), a modular, open research model that enhances the SP-8072 framework. SATURN integrates high-fidelity parameters derived from recent medium-lift class Atlas V 401 launch measurements and incorporates an empirical approach to model propagation losses in rocket noise spectra. Validation against acoustic data from small-lift Firefly Alpha and super-heavy lift SpaceX Starship rocket launches includes 34 measurement points spanning a wide range of distances. SATURN accurately predicts unweighted and A-weighted sound levels and spectra near peak noise radiation, significantly outperforming SP-8072. Within 20 km, SATURN achieves a root-mean-square error of approximately 1 dB for maximum unweighted levels, a factor of two or more improvement in

acoustic pressure accuracy over the legacy model. These results demonstrate SATURN's potential as a modular, accurate tool for rocket noise prediction based on modern data, providing a foundation for ongoing research and validation across diverse vehicles and launch scenarios.

6.1 Introduction

Rockets are among the most intense, sustained sources of anthropogenic noise. As global launch activity accelerates—with no signs of slowing (see Fig. 1.1)—acoustic concerns remain a central challenge in launch operations. The extreme amplitudes and broadband character of rocket noise can affect payloads, vehicles, infrastructure, nearby communities, and the environment. Accurate modeling and prediction are essential for assessing these impacts and ensuring the safety and sustainability of current and future launch systems.

Computational fluid dynamics and computational aeroacoustics tools such as the NASA Launch Ascent and Vehicle Aerodynamics (Kiris *et al.* 2016) code as well as other rocket-noise related simulations (Kiris *et al.*, 2008; Tsutsumi *et al.*, 2015; Harris *et al.*, 2016, Liever *et al.*, 2017; Tsutsumi *et al.*, 2019, Della Posta *et al.*, 2023, among others) have seen significant advancement in recent years. While these tools provide highly resolved flow and acoustic information, they are computationally expensive and have limited validation against acoustic measurements of full-scale rockets, especially in the far-field. As a result, these tools are presently best suited to nearfield applications such as acoustics from interactions between rocket plumes and launch pad structures, as well as investigating the physics of flow-acoustic coupling and noise generation mechanisms. Thus, empirical rocket noise prediction tools retain merit for

applications involving far-field noise prediction due to their computational efficiency and fidelity in the far field.

For over five decades, NASA SP-8072 (Eldred, 1971) has served as the foundational empirical model for rocket noise prediction. It has informed numerous derivative models and undergone selective refinements (Haynes *et al.*, 2009; James *et al.*, 2012). As reviewed by Lubert *et al.* (2022), SP-8072 is based on empirical data collected in the 1950s and ’60s. While advanced for its time, the underlying instrumentation, analysis methods, and rocket engine technologies have since been surpassed in precision and complexity. Though some modern efforts have refined individual model parameters such as the directivity indices (e.g., Kenny *et al.*, 2009; James *et al.*, 2012), much of the methodology in SP-8072 has not been revisited in the literature, and propagative losses remain unaddressed in the SP-8072 model.

This paper presents SATURN (Scientific Acoustic Tool for Understanding Rocket Noise), a revised predictive framework that modernizes the SP-8072 approach for 21st-century launch systems. SATURN builds upon the SP-8072 methodology in three key ways: it integrates high-fidelity inputs from modern measurements, accounts for propagative losses using empirical modeling, and is designed to be modular and extensible—supporting evolving launch architectures and mission requirements.

Unlike commercial tools such as RUMBLE (Bradley et al., 2018), which is publicly available but closed-source, or RNOISE (Sutherland, 1993; Plotkin et al., 2004; Plotkin, 2010), which is not publicly distributed, SATURN is a research-focused tool. It provides full, time-resolved spectral estimates of rocket noise and is structured for easy modification, allowing researchers to incorporate new inputs and refine model components. Moreover, it is released in a

publicly available format with transparent methodology, enabling the research community to examine, validate, and build upon its approach.

The following sections detail SATURN's methodology, including the derivation of updated source characteristics from modern data, an empirically informed propagation model, and validation against measurements from two modern launch vehicles: Firefly Alpha and SpaceX Starship. Validation results demonstrate SATURN's improved performance with regard to unweighted and A-weighted maximum levels across a range of distances, as well as comparing its predictions for time-resolved sound levels and maximum spectra at several representative sites. Compared to SP-8072, SATURN represents both a significant improvement in terms of absolute metrics, as well as time-resolved and broadband spectral predictions that closely match measured acoustic data—a capability not available in present public-facing tools.

6.2 Model Data Sources

The model is developed using acoustic measurements from the launch of a medium-lift class Atlas V 401 rocket at Vandenberg Space Force Base, California, USA for the JPSS-2 mission. A detailed description of the data collection campaign is provided by Mathews *et al.* (2023). Measurements were acquired at various radial distances (d) and azimuthal angles relative to the launch pad—ranging from 220 m to 7.2 km from the launch site. A map of the measurement locations relative to the launch facility is provided in Fig. 6.1. Weather conditions during the launch, summarized by Mathews and Gee (2025), were cool, clear, and characterized by light, steady winds. These mild and uniform conditions help ensure that variations in measured levels are dominated by source and geometric effects, with minimal influence from atmospheric refraction, turbulence, or other meteorological propagation effects. While SATURN's parameters

are currently developed using this single dataset, its modular formulation and empirical basis are intended to allow for application to a wide range of rocket configurations and scales. Future incorporation of additional launch datasets spanning different vehicle types, scales, and atmospheric conditions could potentially improve the model's predictive robustness and broaden its general applicability.

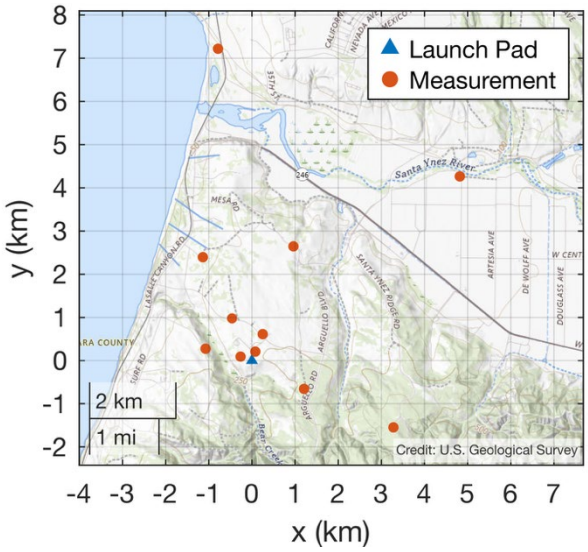

Figure 6.1. Map showing measurement locations and launch pad for the Atlas V JPSS-2 launch.

To minimize the influence of meteorological and other propagation effects, only data collected within 1 km of the launch site are used to construct the source model. This threshold balances two considerations: reducing propagation-related attenuation and maintaining sufficient spatial coverage. A smaller distance could further limit propagation effects but would reduce the number of available measurement sites to less than three, making the results more susceptible to bias from any single station. The 1 km range thus provides a practical compromise, retaining three independent sites for averaging while ensuring the derived source characteristics primarily reflect source-region physics. Previous launch noise studies demonstrate nearly spherical decay

within this range, indicating minimal propagative attenuation (Durrant *et al.*, 2023; Mathews *et al.*, 2023; Gee *et al.*, 2025b).

6.3 Methodology

This section outlines the SATURN methodology. First, the problem geometry and coordinate system are introduced. Then, the procedure for estimating source sound power and its spectral distribution is described. The process for computing sound pressure levels at receiver locations—accounting for directivity, geometric spreading, and propagation losses—is then presented. Finally, the framework for computing relevant noise metrics is discussed.

6.3.1 Layout and Geometry

To compute acoustic quantities at field points relative to a moving rocket source, a consistent frame of reference is required. SATURN adopts a fixed east-north-up (ENU) coordinate system, with the origin at the bottom center of the launch vehicle on the launch pad: $(x, y, z) = (0,0,0)$. The ENU axes are defined such that +x points east, +y points north, and +z points vertically upward. The observer position is represented in this coordinate system as $\boldsymbol{P} = (x, y, z)$ and the rocket trajectory is given as $\boldsymbol{T} = (x', y', z')$. For a rocket trajectory, each component of the state vector is a vector itself and is a function of time.

6.3.2 Sound Power

SATURN begins by estimating the overall sound power of the rocket plume, a key source quantity that describes the total amount acoustic power radiated to the far-field. This is done in two steps: estimating the total (broadband) sound power level and then deriving the sound power spectrum. This allows for the total acoustic power output of the rocket at each frequency to be estimated. From this, spectral sound pressure levels can be estimated through the application of directivity indices and propagation.

6.3.2.1 Overall Sound Power Level

First, the overall sound power level (OAPWL) is estimated from plume parameters. The total mechanical power of a rocket plume is approximately given by the expression

$$W_m \approx \frac{1}{2} F U_e, \tag{6.1}$$

where F is the vehicle thrust in Newtons and U_e is the exit velocity in meters per second (Eldred, 1971; Mathews and Gee, 2025). Note that this expression is a simplification of the full expression for mechanical power; for engines operating in extremely over- or underexpanded regimes (exit pressures ~>50% different than ambient pressure), this approximation may not hold. Mathews and Gee (2025) discuss the derivation of this equation, its simplifications, and the error associated with this approximation for several rocket engines. They show that for several representative rocket engines, this expression is accurate to within 0.3 dB of the full expression for mechanical power.

From the mechanical power, the overall acoustic power, W_{OA}, can then be estimated. This is done by assuming an acoustic efficiency parameter, η, that describes the ratio of acoustic to mechanical powers in the jet plume (Franken, 1958; Eldred, 1971):

$$W_{\mathrm{OA}} = \eta W_m \approx \frac{\eta}{2} F U_e. \tag{6.2}$$

Eldred (1971) suggested that η is likely bounded between 0.1% and 1%, with 0.5% being a conservative average estimate. Based on comparisons between modeled and measured levels for Atlas V, Mathews and Gee (2025) found that an acoustic efficiency of 0.33% yields accurate predictions of peak sound pressure levels. There is still much to be understood about η, especially whether it is a fixed quantity or whether it appears to change based on rocket engine type, parameters, and clustering—basic sound level modeling by Mathews and Gee (2025) indicates that two different rocket configurations need different values of the parameter η in a model to accurately predict maximum levels. Furthermore, Christian *et al.* (2023) demonstrate that η appears to vary for a tactical aircraft engine across engine condition—a phenomenon that could potentially extend to the rocket regime.

The overall sound power level in decibels is then given by:

$$L_{w,\mathrm{OA}} = 10 \log_{10}\left(\frac{W_{\mathrm{OA}}}{W_{\mathrm{ref}}}\right) = 10 \log_{10}\left(\frac{1}{2}\frac{\eta}{W_{\mathrm{ref}}} F U_e\right), \tag{6.3}$$

where W_{ref} is the reference acoustic power equal to 10^{-12} W. In terms of error propagation, Mathews and Gee (2025) discuss that errors of up to 5% in W_m only produce variations of 0.2 dB in $L_{w,\mathrm{OA}}$, so this computation is not particularly sensitive to minor errors.

6.3.2.2 Sound Power Spectrum

With the overall sound power level determined, the sound power spectrum $L_w(\mathrm{Sr})$ can be estimated using a normalized relative spectrum $\bar{L}_w(\mathrm{Sr})$. This normalized spectrum expresses the

spectral levels relative to the overall sound power level and applies Strouhal-number scaling to account for geometric and velocity differences between rockets. This approach enables the construction of a model spectrum that can, in principle, be scaled to any rocket configuration. Although Mathews *et al.* (2021) and Lubert *et al.* (2022) highlight uncertainties with Strouhal scaling for rockets, it remains the most widely used and practical method available. The Strouhal number is a dimensionless frequency defined as $\mathrm{Sr} = fD_{\mathrm{eff}}/U_e$, where f is the frequency in hertz, D_{eff} is the effective nozzle diameter, and U_e is the exhaust velocity. For clustered nozzles, D_{eff} is typically calculated as $D_{\mathrm{eff}} = D_e\sqrt{N}$, where D_e is the single-nozzle exit diameter and N is the number of engines (Eldred, 1971).

SP-8072 (Eldred, 1971) aggregated a wide range of rocket data sources from 1950's and 60's literature to produce the normalized sound power spectrum $\bar{L}_w(\mathrm{Sr})$, shown as the dashed blue curve in Fig. 6.2. This included data from various scales and types of rocket engines, as well as some data from jet engines. Also shown in Fig. 6.2 as the orange dashed-dot line is the power spectrum computed from Atlas V launch measurements taken within 1 km of the launch pad. Notably, the spectral peak occurs at a lower frequency—near a Strouhal number of 0.1—approximately an octave below the peak of the SP-8072 curve (Kellison *et al.,* 2024). This octave difference in spectral predictions is significant and can substantially impact noise metrics, especially those involving frequency weighting. The shaded orange region represents the observed variability in the Atlas V spectra that were averaged to produce the orange curve. Using this average spectrum as a reference, an empirical spectral shape was developed by fitting a function to the measured average, as given in Eq. (6.4) and shown as the solid black line in Fig. 6.2. This fitted curve is used as the $\bar{L}_w(\mathrm{Sr})$ model for SATURN.

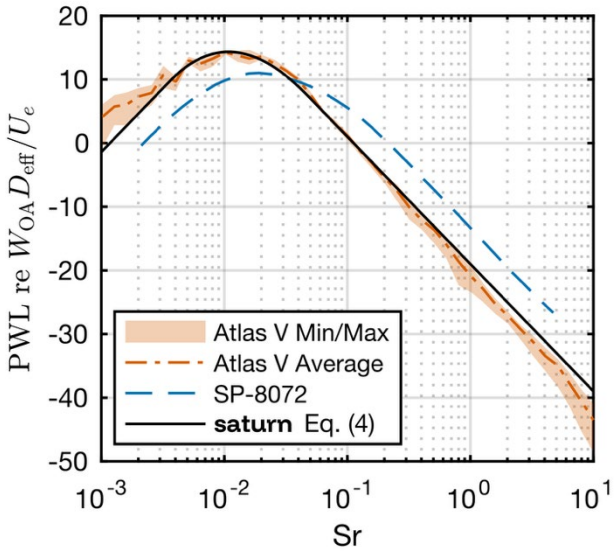

Figure 6.2. Normalized relative sound power spectrum model derived from Atlas V launches compared with SP-8072 model.

$$\bar{L}_w(\mathrm{Sr}) = \begin{cases} 8.686\ \ln(\mathrm{Sr}) + 58.6 & \text{if } \mathrm{Sr} < 3.6 \cdot 10^{-3} \\ 0.26\ \ln(\mathrm{Sr})^3 - 15.98\ \ln(\mathrm{Sr}) - 33.88 & \text{if } 3.6 \cdot 10^{-3} \le \mathrm{Sr} \le 4.8 \cdot 10^{-2} \\ -8.686\ \ln(\mathrm{Sr}) - 19 & \text{if } \mathrm{Sr} > 4.8 \cdot 10^{-2} \end{cases}. \tag{6.4}$$

This model assumes slopes of 20 dB per decade on either side of the spectral peak—matching the slope of the SP-8072 curve, but with a narrower and lower-frequency peak. The absolute sound power spectrum $L_w(\mathrm{Sr})$ is then obtained by de-normalizing the Strouhal-scaled normalized spectrum and accounting for the overall sound power level as follows:

$$\begin{aligned} L_w(\mathrm{Sr}) &= \bar{L}_w(\mathrm{Sr}) - 10\log_{10}\left(W_{\mathrm{OA}}\frac{D_{\mathrm{eff}}}{U_e}\right) \\ &= \bar{L}_w(\mathrm{Sr}) - 10\log_{10}\left(\frac{\eta}{2W_{\mathrm{ref}}}FD_{\mathrm{eff}}\right). \end{aligned} \tag{6.5}$$

6.3.3 Sound Pressure Levels

With the source sound power spectrum determined, sound pressure levels at receiver locations can be estimated. This is done as a four-step process: first, the noise source locations in the plume are estimated. Second, directivity indices are used to establish the directivity of the rocket noise source. Third, a propagation routine is employed, and fourth, ground effects from receiver geometry are taken into account.

6.3.3.1 Source Locations

While the model assumes a compact source at each frequency, the axial source position is allowed to vary with Strouhal number. This is depicted in Fig. 6.3. In the extreme near field, this compact-source assumption is expected to break down. Gee *et al.* (2016) showed that at lower, dominant frequencies, the rocket plume peak source region can extend roughly $l_s \approx 10 - 20\ D_{\text{eff}}$. At distances of $r \approx 100 - 200\ D_{\text{eff}}$ or more, however, the source appears relatively compact as $r \gg l_s$.

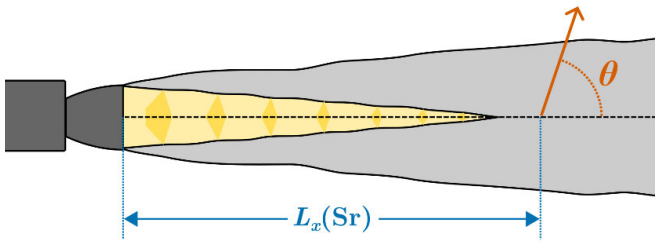

Figure 6.3. Schematic of a rocket plume showing the definition of the angle θ for a given frequency-dependent source location s(Sr).

In the acoustic far field, variations in apparent source location have minimal effect on predicted noise due to small differences in propagation angle. However, in the near field, source location significantly affects computed sound levels. As an observer approaches the launch pad,

the plume angle θ depends increasingly on the axial origin of the source. This demonstrates the importance of using frequency-dependent source positions for near-field predictions. Further quantification of the expected error associated with different fixed source origin assumptions and the frequency-dependent source location of a rocket is given in Appendix B.3.

Since the acoustic source location varies based on frequency, different source locations must be assumed for different frequencies to produce accurate broadband results, as errors in source location will affect the computed directivity angles. Figure 6.4 shows several empirical and modeled axial source location curves as a function of Strouhal number. Two historical curves from SP-8072 are included, based on measurements of single-nozzle, undeflected rocket plumes. Also shown are more recent measurements from vector intensity methods by James *et al.* (2012) of a Space Shuttle solid rocket booster and Gee *et al.* (2016) of a GEM-60 solid rocket motor. Because the James *et al.* (2012) data may reflect plume-ground impingement effects due to a horizontally-fired rocket engine near the ground, the Gee *et al.* (2016) curve is selected as the empirical basis for SATURN—note that this curve is was determined by finding the mean source location as a function of frequency from the Gee *et al.* (2016) data. The James *et al.* (2012) curve, though not used in SATURN, is retained here as it has been proposed as an updated input for SP-8072.

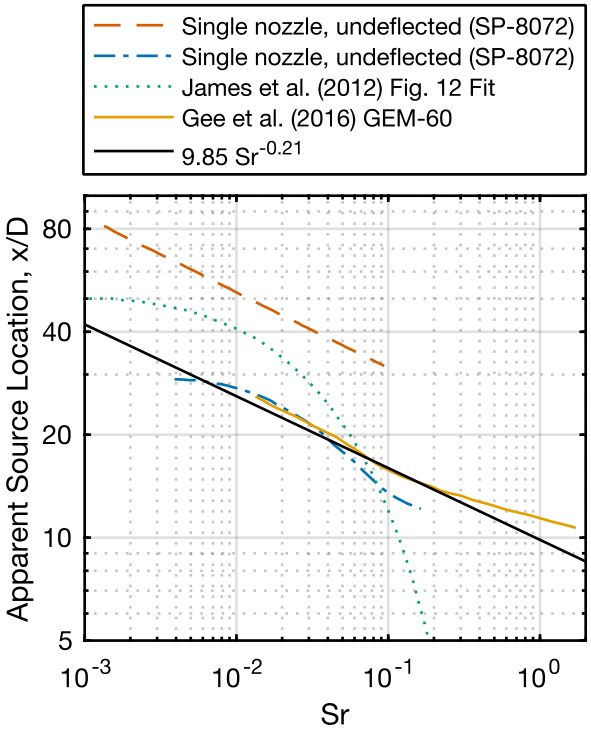

Figure 6.4. Apparent axial source locations from different rocket measurements and models as a function of Strouhal number.

A power-law fit to the Gee *et al.* (2016) data yields the following relation for the axial source location:

$$s(\mathrm{Sr}) = 9.85\ \mathrm{Sr}^{-0.21} D_{\mathrm{eff}}, \tag{6.6}$$

where s is the apparent axial source location in meters as measured from the exit plane of the rocket.

6.3.3.2 Directivity Indices

While the sound power spectrum characterizes the rocket's total acoustic energy output, predicting noise at a specific location requires accounting for directivity. Rocket noise exhibits strong directional dependence, especially at higher frequencies. This directivity primarily stems from the convective nature of turbulent jet sources and varies with frequency. Directivity indices

are used to model this directionality—the definition of directivity index here is given as the decibel quantity of the ratio of the acoustic intensity at a given frequency and angle to the intensity produced by an omnidirectional source of the same equivalent acoustic power and is the same used by Beranek and Mellow (2012). A positive directivity index value indicates more acoustic intensity in a particular direction than an equivalent-power omnidirectional source, while a negative directivity index indicates less.

SP-8072 provides directivity indices at only five frequencies. While interpolation and extrapolation could be used to produce broadband results, this would involve considerable room for error given that there are only five frequency data points. Additionally, the source origin assumptions made in the computation of these directivity indices is not documented in SP-8072, hence error could have been introduced in their computation if the data were collected in the near field and inappropriate source origin assumptions were made. To provide modern, broadband directivity indices SATURN incorporates directivity data derived from the Atlas V measurements within 1 km of the pad. These were computed assuming a source origin of 18 D_{eff}. The closest measurements used to produce these directivity indices were located at a radial distance of 240 m = 119 D_{eff} from the launch pad, hence the results are expected to be accurate to within ±5° at Strouhal numbers greater than 0.004. These are shown in Fig. 6.5(a) as a frequency-angle pseudocolor map. Directivity indices are denoted as $Q(\theta, \mathrm{Sr})$, being dependent both on angle θ and frequency Sr. Note that this formulation for Q assumes azimuthal symmetry—that is, it treats noise as uniform in all directions around the plume axis (the azimuthal angle, measured in the horizontal plane, represents rotation about this axis). This simplification is made because the current approach models clustered nozzles as a single, equivalent plume. Future model developments will incorporate multi-core configurations to

capture azimuthal asymmetry in the noise distribution. The lowest frequencies shown in Fig. 6.5 have very shallow directivity, while the directivity angle trends toward a relatively consistent ~72° peak at Sr > 0.03.

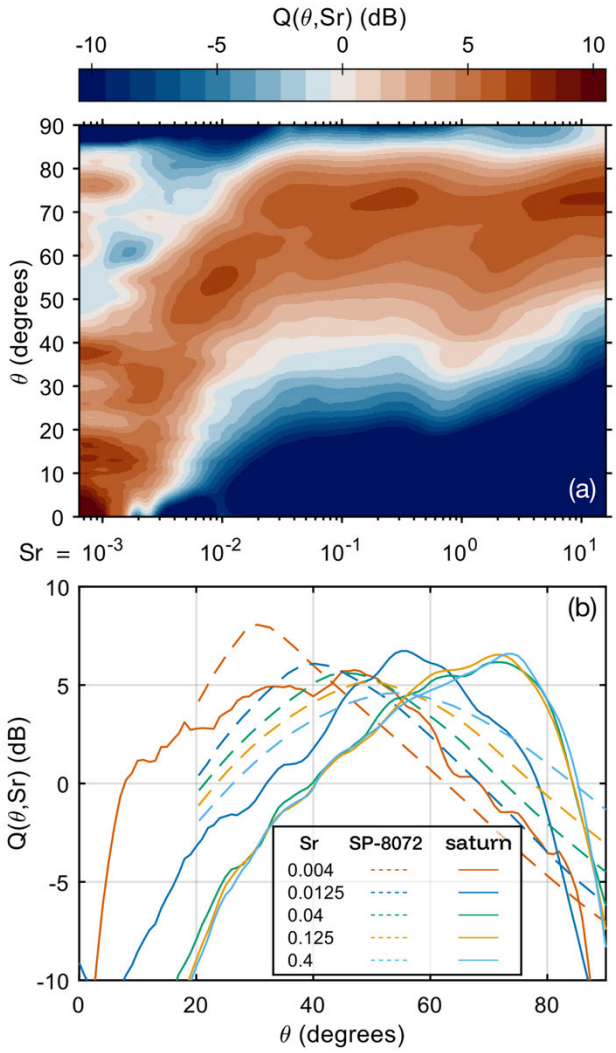

Figure 6.5. Frequency-dependent directivity indices derived from the Atlas V data inside of 1 km radially from the launch site.

Comparatively, Fig. 6.5(b) compares the directivity indices at the five discrete frequencies in SP-8072 to those derived from Atlas V launch measurements. Notably, the directivity angles of SP-8072 trend more aft than the Atlas V, by approximately 15 to 20 degrees—a significant difference. This could potentially be due to poor source origin assumptions in the SP-8072

directivity indices, which has been suggested by Lubert *et al.* (2022). Incorrect directivity indices can produce significant differences in predicted levels: for example, if the directivity angles are too far aft (as is the case for the SP-8072 directivity indices as shown in Fig. 6.5(b)), the peak noise will be predicted to occur later in the launch than it would actually occur.

6.3.3.3 Propagation

Rocket noise is significantly affected by atmospheric propagation, especially in the far field. Two primary propagation effects are presently considered in SATURN: geometric spreading and spectral attenuation of high frequencies due to thermoviscous, relaxation, and nonlinear losses.

6.3.3.3.1 Geometric Spreading

Following SP-8072, SATURN applies spherical spreading by default:

$$S(r) = 10\log_{10}(4\pi r^2). \tag{6.7}$$

Spherical spreading is appropriate for most launch scenarios and has been observed in multiple studies to match measured decay rates for rockets at distances beyond ~10 km (Mathews and Gee, 2025; Gee *et al.*, 2025b). SATURN allows for alternate spreading models by allowing the user to specify the geometric decay rate, but altering the model to other than spherical spreading necessitates recalibration of the model inputs to maintain consistency as the inputs were determined assuming spherical decay.

6.3.3.3.2 Propagative Losses

Propagative effects such as absorption, nonlinear distortion, and curved-ray paths can all alter received rocket noise. These effects grow with distance are dependent both on frequency and launch-time atmospheric conditions. Gee *et al.* (2025b) documented substantial variability in Starship noise metrics under differing weather conditions, especially beyond 20 km. Similar

trends appear across other launch systems (Kellison *et al.*, 2023). It is therefore crucial that propagation effects are modeled accurately when generating predictions and that specific propagation effects are not embedded in the source model when derived from measurements.

One might consider averaging measurements taken at various distances to produce a "mean" source model. However, this approach can be problematic because it combines data with vastly different propagation effects—some with minimal attenuation (close range) and others with significant attenuation (farther away). As a result, the averaged model may be biased if the sampling distances are not representative of the intended application range and can lead to inaccurate noise predictions at distances that differ from the average measurement location.

A more physically grounded approach—used in SATURN—is to derive source parameters from near-field data (typically <1 km), where propagation effects are minimal, and apply an explicit propagation model separately. This provides the best chance at preserving the underlying source physics and allows for incorporation of actual atmospheric conditions when needed.

Future work could combine SATURN with numerical nonlinear propagation algorithms to enhance long-range prediction accuracy (Gee *et al.*, 2008; Gee *et al.*, 2012; Reichman *et al.*, 2016). In the absence of this complexity, SATURN employs an empirical attenuation model derived from the measured decay of sound pressure level spectra at multiple distances. This attempts to model propagation as a function of distance explicitly, rather than just averaging across all distances. Figure 6.6 shows (a) the decay of maximum sound pressure level with distance for the Atlas V, as determined from the measurements. Frequencies below 10 Hz (Sr = 0.0064) are excluded due to low-frequency microphone uncertainty in some of the of the measurement channels. As distance increases, high-frequency energy decays—primarily due to atmospheric absorption. However, losses are less severe than predicted by linear theory, likely

due to the compensating effects of harmonic generation via nonlinear propagation. For example, at 1 kHz, the maximum sound pressure level spectra reveal losses of ~15 dB across 7 km in the maximum sound pressure level spectra. Across this distance, linear absorption theory would predict attenuation of 26 dB, about 11 dB more than observed. Furthermore, at 10 kHz, the recorded attenuation was on the order of 30-40 dB, whereas linear theory predicts attenuation in excess of 1200 dB, a clear gross overestimate of the actual attenuation. This illustrates the inability to use traditional linear absorption models for rocket noise propagation, unless the effects of nonlinear propagation can also be modeled appropriately. The interplay between these two effects for broadband signals should be a subject of further research (Reichman *et al.*, 2016; Miller and Gee, 2018; Gee *et al.*, 2018).

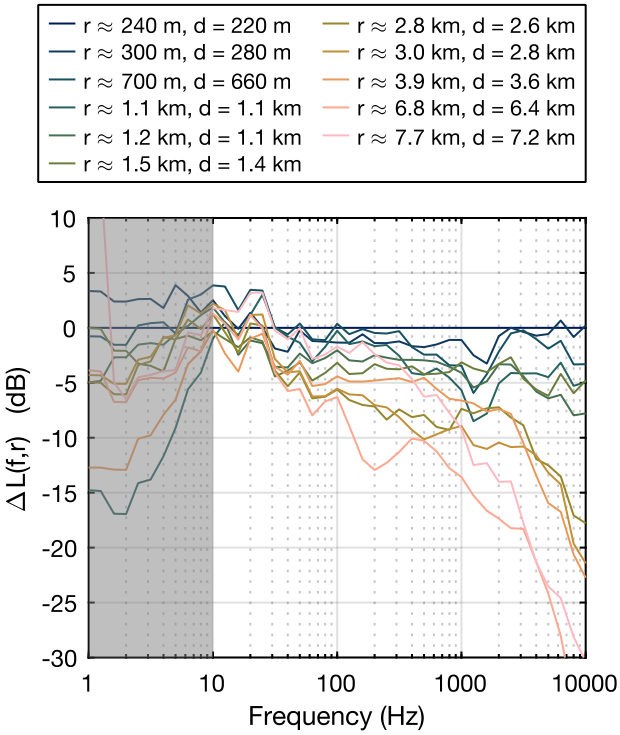

Figure 6.6. Apparent decay as a function of distance from the Atlas V JPSS-2 measurement for the spectra during the period of maximum directivity, defined as the region 3 dB down from the maximum recorded level.

Because long-range rocket noise propagation involves multiple complex mechanisms—such as atmospheric absorption and nonlinear propagation—a simpler, empirical approach was adopted in SATURN to represent propagative losses. This improves on SP-8072, which does not explicitly account for these losses.

Propagation losses vary significantly over the course of a launch because the source moves rapidly relative to the observer, continuously changing the effective propagation distance. To capture these effects, SATURN applies the propagation model directly to the sound pressure level spectra rather than to overall levels alone. This spectral approach allows the model to represent the frequency-dependent nature of atmospheric absorption and other loss mechanisms, which is essential for accurate far-field predictions.

To empirically represent the observed spectral decay, a frequency-dependent loss function was derived from measured maximum sound pressure level spectra at different distances from the Atlas V launch. This function uses a traditional Butterworth filter shape to reproduce the decay characteristics observed in the data, and is expressed mathematically as:

$$B(f,r) = 10\log_{10}\left(\frac{1}{\left[1+\frac{f}{f_c}\right]^{n}}\right), \quad n = \sqrt{\frac{r}{r_c}} \tag{6.8}$$

where f_c is the critical Strouhal number, which controls the rolloff point of the filter, n is the filter order, and r_c is a critical distance to adjust the rolloff of the filter with distance. For Atlas V data, the attenuation behavior is approximated by using two filters: one to model the broad spectral rolloff starting at 10 Hz, and another to model the accelerated rolloff at higher frequencies and is formulated as

$$A(f,r) = B_1(f,r) + B_2(f,r). \tag{6.9}$$

This double-filter model uses the parameters of $f_{c1} = 8$, $r_{c1} = 12\,000$, $f_{c2} = 8\,000$, and $r_{c2} = 3\,000$. To evaluate this model, Fig. 6.7(a) shows the apparent sound pressure level spectral decay across distance relative to the acoustic source. While some of the lower frequencies contain some anomalous details, an overall trend can be seen in the data where the sound pressure level spectra are increasingly attenuated with distance. Figure 6.7(b) shows the application of Eq. (6.9) to the same frequencies and distances. Though the modeled trend is much smoother, similar behavior can be seen with the modeled attenuation, especially when comparing the -6, -12, and -18 dB contour lines, albeit slightly more aggressive. Further work could improve this model by fitting it across several launches and rocket types.

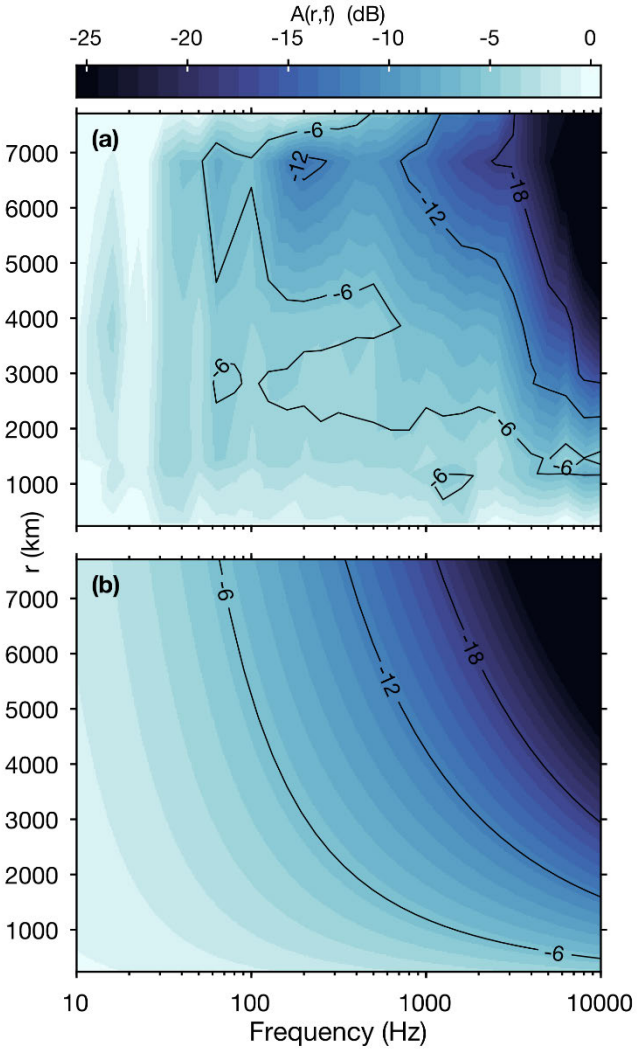

Figure 6.7. (a) Apparent sound pressure level spectral decay from measurements of the Atlas V JPSS-2 mission relative to the closest measurement station as a function of distance to the source and dimensional frequency. (b) Modeled sound pressure level spectral decay using the double-filter model based on Eq. (6.9).

6.3.3.4 Sound Pressure Levels

With directivity and propagation effects modeled, the predicted sound pressure level spectrum at a receiver location becomes:

$$L(r, \theta, \mathrm{Sr}) = L_w(\mathrm{Sr}) + A(r, f) + S(r) + Q(\theta, \mathrm{Sr}) \tag{6.10}$$

where $L(r, \theta, \mathrm{Sr})$ represents the sound pressure level spectrum at a receiver location at a given distance from the source r, plume angle θ, and frequency Sr (or corresponding dimensional frequency f for the propagation loss model).

6.3.4 Metrics

SATURN produces time-resolved spectral outputs, effectively providing high-resolution spectrograms. From these, users can compute any desired noise metrics (e.g., SPL, SEL, LEQ, etc.) using standard procedures. The calculation of specific metrics is left to the end user. This approach preserves flexibility and allows researchers to tailor metrics to application-specific needs.

6.4 Validation

6.4.1 Validation Datasets

To evaluate the model's generalizability, a validation is conducted using data from two different launch vehicles: Firefly Alpha and SpaceX Starship. Relevant vehicle information is summarized in Table 6.1, with the inclusion of the Atlas V 401 rocket used in constructing the model parameters for SATURN for comparison. These two rocket are representative of the extremes of orbital rockets in terms of scale: Alpha is among the smaller orbital rockets in operation, while Starship is the largest and highest-thrust vehicle ever to launch; their thrust classes span two orders of magnitude. These extremes of scale provide an opportunity to validate the model outside of the medium-lift scale Atlas V that SATURN was developed with. Additionally, they represent different engine configurations than the Atlas V used to develop this model: Alpha has a cluster of four engines, while Starship has a cluster of 33 engines. While Alpha uses the same fuel type as Atlas V, Starship uses a different fuel source entirely. These validation data were obtained through measurements of the Firefly Alpha Flight 5 "Noise of Summer" launch and the SpaceX Starship's sixth test flight (Gee *et al.*, 2025b).

Table 6.1. Relevant information for the validation and model-construction rockets.

Vehicle	**Class**	**Configuration**	**Total Thrust (MN)**	$\boldsymbol{U_e}$ **(approx.., m/s)**	$\boldsymbol{D_e/D_{\text{eff}}}$ **(approx., m)**
Firefly Alpha	small	1 core (4 engines)	0.73	2900	0.38/0.76
ULA Atlas V 401	medium	1 core (2 nozzles)	3.83	3160	1.43/2.02
SpaceX Starship	super-heavy	1 core (33 engines)	73.5	3340	1.31/7.53

6.4.2 Alpha Validation

For Alpha Flight 5, measurements were made at distances between 140 m and 7.3 km from the launch site. Sound levels were predicted using both the SP-8072 and SATURN models, based on vehicle parameters from Table 6.1, the flight trajectory, and an assumed acoustic efficiency of 0.34%. Figure 6.8 compares the predicted maximum sound levels during launch with measured data across all measurement sites. Panel (a) shows the unweighted maximum levels ($L_{Z,\max}$), while panel (b) presents the prediction errors relative to measurements ($\Delta L_{Z,\max}$). Panels (c) and (d) follow the same pattern, except for they represent the A-weighted maximum levels ($L_{A,\max}$) and prediction errors ($L_{A,\max}$). A-weighted metrics are included here as they are often used in environmental and community noise contexts; additionally they also help quantify the high-frequency accuracy of the models. The shaded region indicates ±2 dB around the measurements, and log-linear trend fits are included. Accuracy statistics accompany these plots.

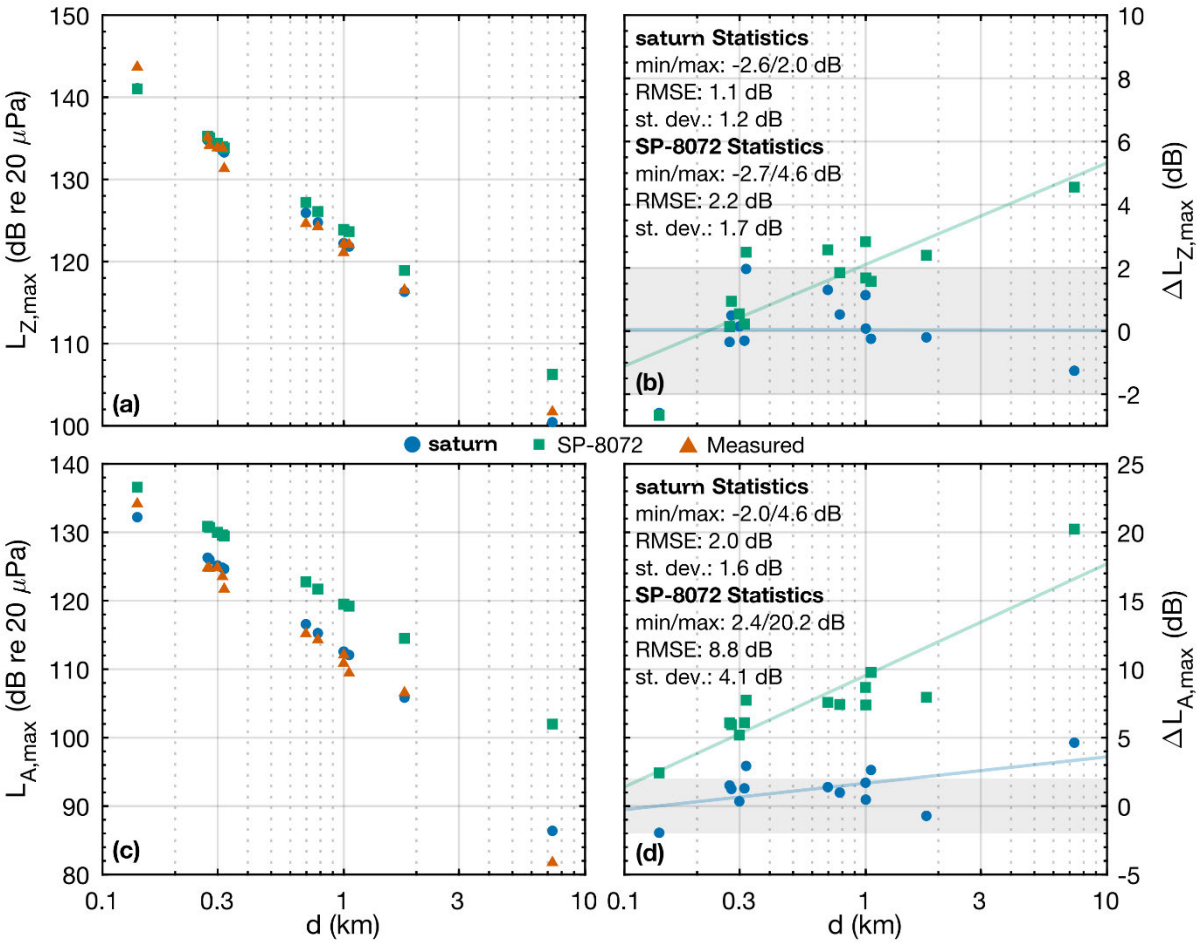

Figure 6.8. Maximum sound pressure levels from Alpha Flight 5 across various distances from measurements compared with predictions from SP-8072 and SATURN for (a) unweighted levels and (c) A-weighted levels. Deviations between measured and modeled levels for (b) unweighted and (d) A-weighted levels; ±2 dB shaded region and logarithmic fits of deviations shown.

Except for the closest site at 140 m, SATURN predicts the absolute unweighted maximum levels ($L_{z,\max}$) within ±2 dB accuracy for all other sites with a root-mean-square error of 1.1 dB. SP-8072, however, exceeds this accuracy tolerance for half the sites, with an RMSE of 2.2 dB. Trend-wise, SATURN appears to follow the decay rate for $L_{z,\max}$ within ±2 dB throughout the measurements, however, SP-8072 appears to slowly diverge with a different slope, as indicated by the linear fits of the $\Delta L_{z,\max}$ values. This indicates that the modeled spectral decay in the SATURN model replicates the actual decay behavior for this measurement well.

In terms of maximum A-weighted sound levels ($L_{A,\max}$), there is slightly more deviation in the models, as seen in Fig. 6.8(d) than in the unweighted levels. However, for all but three sites, SATURN's A-weighted maximum level deviation, ($\Delta L_{A,\max}$) is within ±2 dB, whereas every SP-8072 prediction falls outside of that range. In terms of error, the RMSE in $\Delta L_{A,\max}$ for SATURN is 2.0 dB compared to 8.8 dB for SP-8072—corresponding to a factor of 2.2 reduction in the underlying acoustic pressure error.

Moving on to a closer examination of three characteristic measurement sites, Fig. 6.9 shows the time-resolved unweighted sound levels and maximum spectra at three representative sites: 300 m (393 D_{eff}), 1.0 km (1313 D_{eff}) and 7.3 km (9609 D_{eff})—representing representing close-, mid-, and long-range distances respectively. In terms of the time-resolved unweighted levels [Figs. 6.9(a,c,e)], SATURN's time-resolved unweighted overall levels ($L_{Z,\text{OA}}$) closely match the region of peak directivity. However, the peak is broader in time with the SATURN predictions, and late-launch levels (>60 s) are overpredicted by up to 5 dB in Figs. 6.9(a,c). Even so, the SATURN predictions mirror the measurements much better than the SP-8072 predictions. SP-8072 predicts a peak directivity region delayed in time relative to measurements and overpredicts late-stage launch levels by 10+ dB, indicating inaccuracies in its directivity indices and its lack of propagation loss modeling.

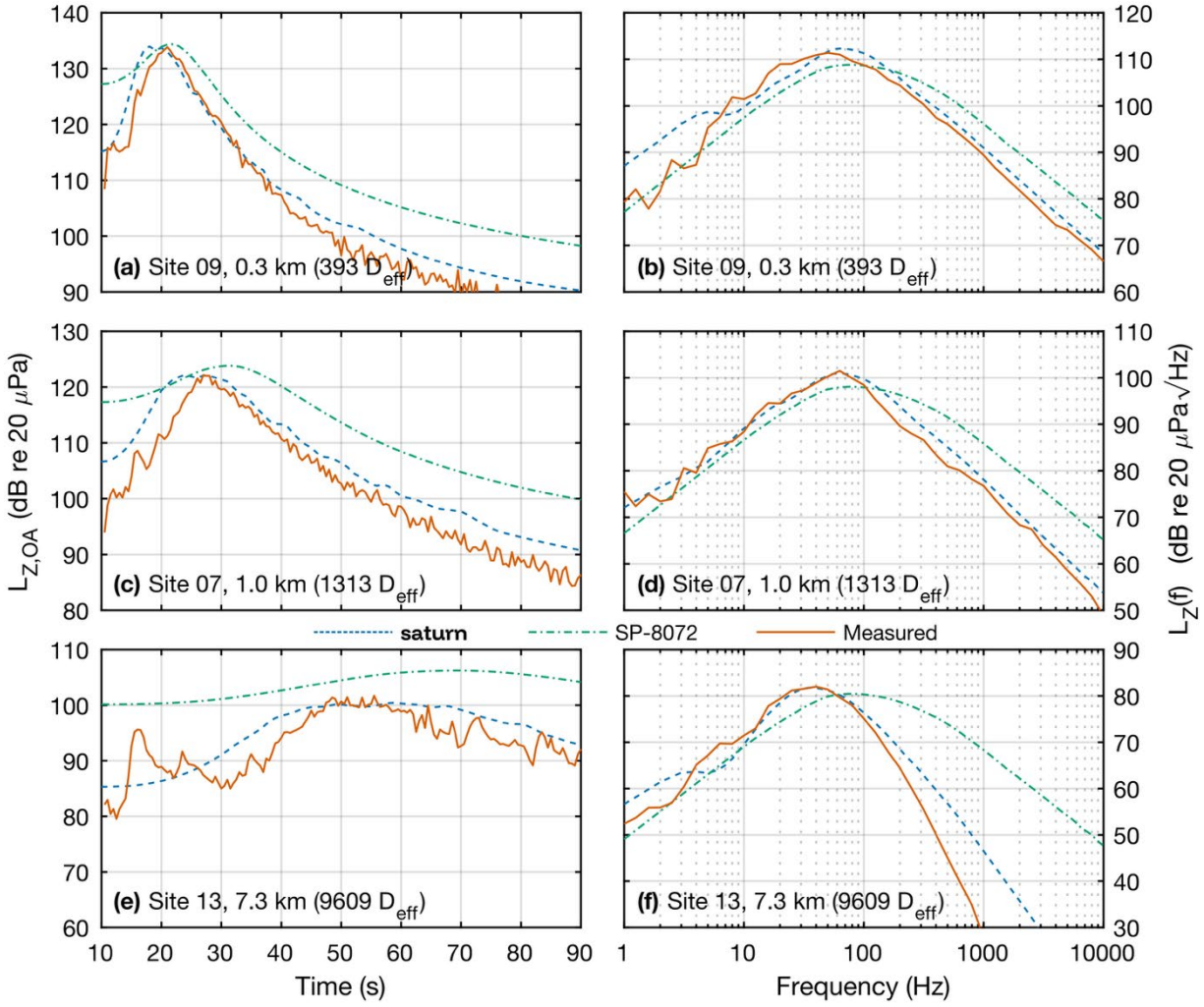

Figure 6.9. Site-specific validation showing unweighted levels as a function of observer time (left column), as well maximum spectra (right column) for Alpha Flight 5 from measurements compared with predictions from SP-8072 and SATURN across three representative distances.

Regarding the maximum spectral predictions in Figs. 6.9(b,d,f), all the SATURN predictions match the peak frequency well, with perhaps a slight overprediction at the closest site. However, SP-8072 predicts a higher peak frequency than measured, which increasingly diverges from the measurements as distance increases, reaching an error of one octave at 7.3 km. Additionally, SATURN predicts the spectral shape well in all three cases, with the largest errors at 7.3 km, where it appears as though more absorption occurred in the measured data compared

to what was modeled by SATURN. This can be observed in Fig. 6.9(e), where SATURN overpredicts the spectral levels at 1 kHz by ~15 dB, whereas SP-8072 overpredicts by nearly 40 dB. This suggests that the predictions could benefit from additional propagation modeling.

6.4.3 Starship Validation

For Starship Flight 6, measurements were taken at distances from 1 km to 35.5 km from the launch site. Sound levels were predicted using both the SP-8072 and SATURN models, based on vehicle parameters from Table 6.1, the flight trajectory, and an assumed acoustic efficiency of 0.4%. Figure 6.10 compares the predicted maximum sound levels during launch with measured data from Gee *et al.* (2025b). Panel (a) shows the absolute unweighted maximum levels ($L_{z,\max}$), while panel (b) presents the prediction errors relative to measurements ($\Delta L_{z,\max}$). The shaded region indicates ±2 dB around the measurements. Exponential trend fits are also shown and were chosen in this case as the measured levels decay roughly exponentially. Accuracy statistics accompany these plots.

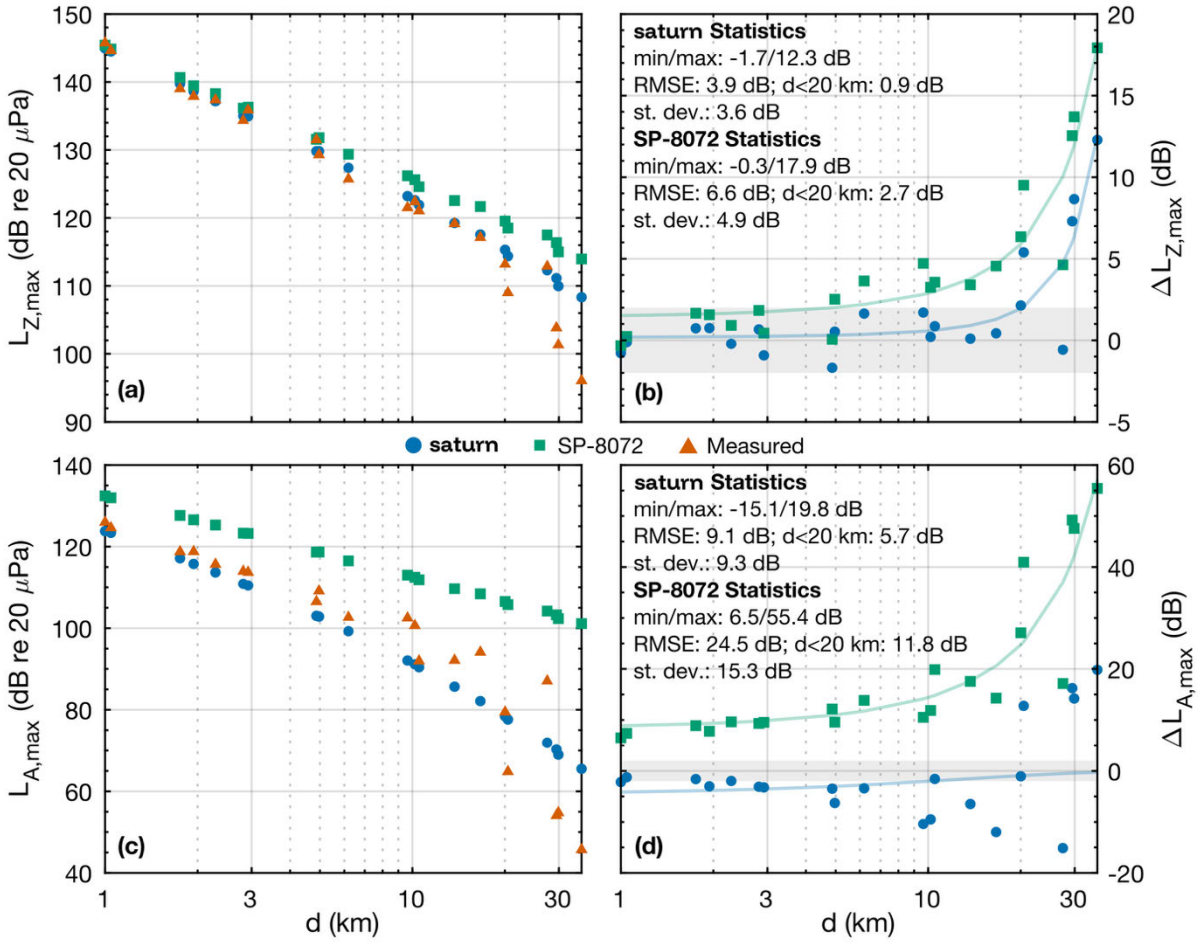

Figure 6.10. Maximum sound pressure levels from Starship Flight 6 across various distances from measurements reported by Gee *et al.* (2025b) compared with predictions from SP-8072 and SATURN for (a) unweighted levels and (c) A-weighted levels. Deviations between measured and modeled levels for (b) unweighted and (d) A-weighted levels; ±2 dB shaded region and logarithmic fits of deviations shown.

SATURN performs well, maintaining errors within ±2 dB up to 20 km (~2660 D_{eff}). Beyond this range, deviations increase, reaching a maximum of 13 dB at 35.5 km. Gee *et al.* (2025b) attributed the observed rapid decay in measured levels between 10 and 20 km to atmospheric conditions during launch, which are not currently modeled in SATURN. Incorporating these effects could improve SATURN's accuracy at greater distances. Limiting the analysis to within 20 km, SATURN's root-mean-square error (RMSE) for $\Delta L_{z,\max}$ is 0.9 dB, compared to 2.7 dB for SP-8072—a significant improvement.

In contrast, SP-8072 predictions exceed ±2 dB error already at 5 km (~660 D_{eff}), four times closer than SATURN, with a maximum deviation of 18 dB at 35.5 km (Fig. 6.10b). Additionally, SP-8072 does not capture the measured decay rate of $L_{z,\max}$ well, whereas SATURN aligns more closely with observations.

Regarding maximum A-weighted sound levels ($L_{A,\max}$), Figs. 6.10(c–d) reveal even larger differences between the models. Measured $L_{A,\max}$ values show greater variability, likely because A-weighting emphasizes higher frequencies (≥1 kHz) and attenuates lower frequencies near the rocket's infrasonic peak. These higher frequencies are more susceptible to variability from long-range propagation and local atmospheric turbulence. Examining prediction errors $\Delta L_{A,\max}$ in Fig. 6.10(d), SP-8072 never achieves better than ±6.5 dB accuracy at any site, while SATURN is within ±2 dB at five locations. SATURN's RMSE for $\Delta L_{A,\max}$ is 2 times lower than SP-8072's across all measurement sites in terms of acoustic pressure; inside 20 km, the RMSE is 5.7 dB for SATURN versus 11.8 dB for SP-8072. This confirms SATURN's improved performance in predicting both $L_{z,\max}$ and $L_{A,\max}$ for Starship Flight 6.

Figure 6.11 provides a detailed comparison of time-resolved unweighted sound levels and maximum spectra at three representative sites: 1 km (133 D_{eff}), 2.9 km (388 D_{eff}) and 10.2 km (1353 D_{eff})—representing close-, mid-, and long-range distances respectively. At the nearest and mid-distance sites [Figs. 6.11(a,c)], SATURN's time-resolved unweighted overall levels ($L_{Z,\text{OA}}$) closely match measurements, except during the first ~8 seconds. This discrepancy likely arises from a deflected plume and ground-level sound propagation effects not yet modeled in SATURN. Beyond this initial period, predicted levels track measurements within 2–3 dB. In contrast, SP-8072 predictions show peak directivity delayed relative to measurements and overpredict late-stage launch levels by 5–10 dB, indicating inaccuracies in its directivity indices.

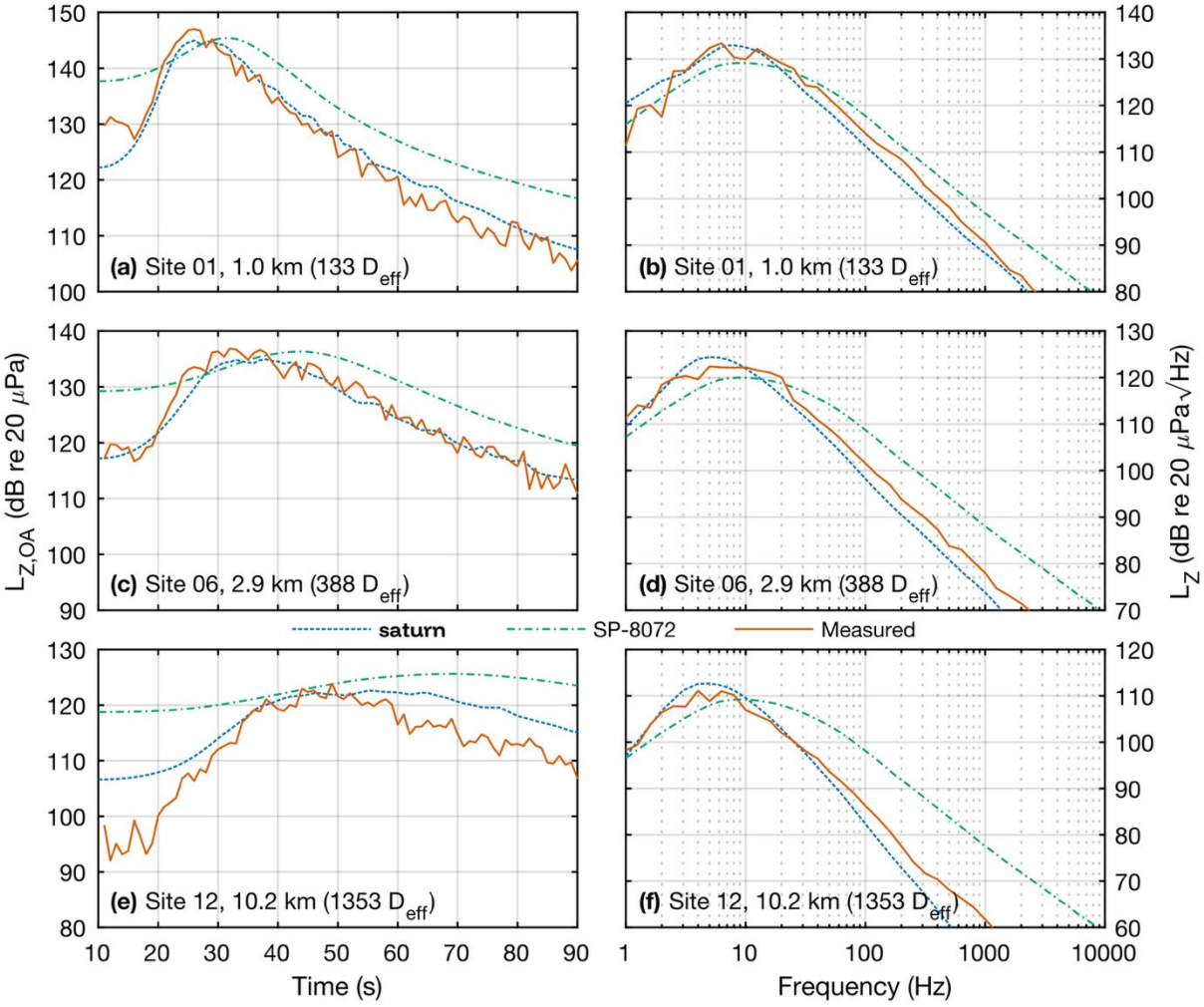

Figure 6.11. Site-specific validation showing unweighted levels as a function of observer time (left column), as well maximum spectra (right column) for Starship Flight 6 from measurements compared with predictions from SP-8072 and SATURN across three representative distances.

At 10.2 km [Fig. 6.11(e)], SATURN's predictions diverge more from measurements. The initial 10–15 seconds are overpredicted, likely for the same reasons as above. Near peak directivity (45–55 s), predictions agree within 0–2 dB, but afterward, measured levels decay more rapidly than predicted. This discrepancy may stem from atmospheric effects such as temperature and wind-induced sound refraction, which are currently absent in the model. Since

predictions are accurate at closer distances, the modeled source characteristics seem appropriate for Starship. Future ray-tracing analyses could clarify these propagation effects.

Examining maximum spectra [Figs. 6.11(d,f)], all sites exhibit similar trends: SATURN matches the general spectral shape but slightly underpredicts high frequencies by 2–3 dB, reflecting a somewhat narrower predicted peak. SP-8072 overpredicts both the spectral peak frequency and high-frequency content, with this effect increasing with distance. At 10.2 km, SP-8072's peak frequency is about one octave too high, and levels at 100 Hz are overpredicted by ~12 dB. Conversely, SATURN accurately predicts peak frequency and only underestimates 100 Hz levels by ~3 dB.

6.5 Conclusion

This work introduces SATURN, an empirical model for predicting rocket launch noise, alongside its preliminary validation. SATURN advances beyond legacy models like SP-8072 by incorporating high-fidelity data from recent measurements, explicitly accounting for propagation losses through empirical modeling, and being implemented as a modular software package designed for research applications and future development.

SATURN was developed using measured acoustic data from an Atlas V 401 rocket launch. These data were used to determine model inputs for the normalized sound power spectrum and directivity indices. Additionally, the launch data were used to formulate an empirical propagation loss model—a deficiency in the original SP-8072 methodology when it was applied to far-field noise prediction.

Validation for the SATURN model compared predictions against launch noise measurements from Firefly Alpha Flight 5 and SpaceX Starship Flight 6. These validation

datasets represent a broad range of vehicle scales and are significantly different in scale than the Atlas V used to derive the SATURN model inputs. For Alpha, SATURN consistently predicts unweighted maximum sound levels within ±2 dB accuracy at all but the closest measurement site, achieving a root-mean-square error (RMSE) of 1.1 dB. This performance notably surpasses that of the SP-8072 model, which exhibits larger deviations and a divergent decay trend. Moreover, SATURN's A-weighted level predictions, important for community noise assessments, show a fourfold reduction in error compared to SP-8072, further emphasizing its enhanced high-frequency fidelity.

For the much larger Starship vehicle, SATURN maintains high accuracy in predicting unweighted sound levels up to 20 km from the launch, with an RMSE of 0.9 dB and errors mostly within ±2 dB. Beyond this range, deviations increase due to atmospheric effects not yet modeled, pointing to opportunities for future refinement. In contrast, SP-8072's accuracy degrades much closer to the launch site and systematically misrepresents the spectral content, particularly at higher frequencies, overestimating the noise spectral peak frequency by an octave. SATURN also better captures the temporal evolution and spectral shape of the noise across sites at close-, mid-, and long-range. These results deomstrate SATURN's capabilities, and also highlight the opportunity to combine the SATURN methodology with more complex propagation models such as ray-tracing to improve its accuracy and incorporate launch-specific meterological effects.

6.6 Chapter Acknowledgments

This research in this chapter was supported in part by the appointment of L.T.M. to the Department of Defense (DOD) Research Participation Program administered by the Oak Ridge

Institute for Science and Education (ORISE) through an interagency agreement between the U.S. Department of Energy (DOE) and the DOD. ORISE is managed by Oak Ridge Associated Universities (ORAU) under DOE Contract No. DE-SC0014664. All opinions expressed in this paper are those of the authors and do not necessarily reflect the policies and views of DOD, DOE, or ORAU/ORISE. The Atlas V measurements were supported in part by Vandenberg Space Force Base through the United States Army Corps of Engineers. Space Launch Delta 30 at Vandenberg Space Force Base is acknowledged for logistical support.

Chapter 7

Conclusions

This dissertation has advanced the understanding, characterization, and modeling of the noise generated by supersonic, afterburning aircraft jet engines and launched rockets. Through a combination of experimental measurements, empirical modeling, and analysis of full-scale systems, several key contributions have been made across six chapters. This chapter synthesizes the primary conclusions and outlines opportunities for future work.

7.1 Primary Contributions

7.1.1 Full-Scale Jet Noise Source Decomposition (Chapter 2)

Coherence-based source decomposition techniques were developed and applied to an installed, afterburning GE F404 engine using acoustical holography. These analyses revealed distinct local maxima (LMs) in the apparent source field along the nozzle lipline, separated by both space and frequency. The results suggest that different physical mechanisms—such as subsonic large-scale turbulence and Mach wave radiation (MWR)—may contribute to the multi-lobed radiation patterns observed in full-scale, heated supersonic jets. The use of phase-unwrapping techniques extended the usable frequency range in acoustic holography and

highlighted the value of coherence-based decompositions for understanding distributed jet noise sources.

7.1.2 Broadband Shock-Associated Noise Characterization (Chapter 3)

Acoustical holography-based reconstructions revealed spatially distinct broadband shock-associated noise (BSN) sources aligned with visible shock cell structures from an overexpanded, afterburning installed GE F404 jet engine. Peak frequency trends showed good agreement with other full-scale engines but diverged from lab-scale and simulated results. While the lab-scale jets available for comparison were unheated and hence disagreement is not entirely unexpected, the full-scale data suggest BSN radiation ~10 degrees further forward of a numerical simulation of an afterburning-like large-eddy simulation from a F404-type nozzle. This suggests that the simulated jet's physics differ slightly from the full-scale, physical jet and reinforces the need to further understand and refine computational models for jet noise. Analytical models failed to accurately predict shock spacing and BSN frequency without empirical correction, indicating that traditional convergent-nozzle-based models need to be adapted for use with convergent-divergent nozzles. Coherence analysis further revealed spatially distributed, partially correlated source structures, reinforcing the view of BSN as a non-local, interconnected phenomenon.

7.1.3 Rocket Launch Acoustics and Source Modeling (Chapter 4)

Launch acoustics from an Atlas V rocket were analyzed from near- to far-field distances. A strong azimuthal asymmetry in ignition overpressure was observed and attributed to the

orientation of the flame trench. A directional source model, incorporating ground reflections and minimal empirical tuning, successfully predicted sound pressure levels across a wide range of receiver locations. Peak frequency differences of maximum spectra observed at different azimuths relative to the nozzle configuration of the rocket highlight the importance of source geometry and visibility in clustered rocket nozzles.

7.1.4 Predictive Models for Supersonic Jet and Rocket Noise (Chapter 5)

An empirical model for predicting maximum overall sound pressure and power levels from supersonic jet and rocket sources was proposed. The model accounts for near-ground effects and was validated across multiple vehicles and engine conditions, typically predicting levels within 2 dB of measured values. Sensitivity studies showed that assumptions about thrust and nozzle parameters can significantly affect predictions, but that for most supersonic jets and rockets that are not operating significantly off-condition, the sensitivity to parameters is small. This model is shown to work for both supersonic jet engines and for launched rockets, spanning large scales in thrust and propulsion type. Apparent acoustic efficiency differences between launches of similar vehicles suggest a need for more study into the source properties of different rocket configurations.

7.1.5 The SATURN Rocket Noise Prediction Model (Chapter 6)

The scientific acoustic tool for understanding rocket noise (SATURN), a new physics-based, full-spectral, semi-empirical model for rocket launch noise fundamentally based on NASA SP-

8072, was developed and validated. The model uses high-fidelity, near-field acoustic measurements and incorporates trajectory and frequency-resolved source features. Despite simplifications, SATURN accurately reproduced measured sound levels from a Falcon 9 launch, showing its robustness and flexibility across different vehicle types. Its emphasis on source fidelity and flexibility makes it a promising foundation for future tools in rocket noise research.

7.2 Recommendations for Future Work

This dissertation has made progress in characterizing military jet and rocket noise and has taken initial steps toward unifying their treatment under a common framework. However, substantial work remains in advancing physical understanding and further bridging the gap between these regimes.

For jet noise, this work has advanced the understanding of unique characteristics in full-scale, installed engines—particularly the spatiospectral lobing behavior. With the emergence of new facilities capable of reproducing afterburning-like jets at lab scale (e.g., Kumar *et al.*, 2025), opportunities exist to assess whether these jets exhibit similar source mechanisms and radiation patterns as their full-scale counterparts. Combined with advances in numerical simulations, these experiments could help unravel the underlying physics of afterburning jet noise.

In the context of BSN, this dissertation highlights the need for improved models of shock spacing in convergent-divergent nozzles. Direct comparisons between lab-scale and simulated afterburning jets may provide insights into full-scale behavior and the role of flow structure in BSN generation.

A key limitation of current full-scale acoustic characterizations is the lack of synchronized flow diagnostics. While purely acoustic methods reveal detailed source structure, they cannot

directly connect radiation to specific flow features. Future work should incorporate techniques such as flow measurements or schlieren imaging alongside synchronized acoustic measurements to establish direct links between flow phenomena and radiated noise. Accomplishing these measurements at both lab-scale and at full-scale could yield important information that can then be used to improve both jet noise theory and models.

While this dissertation has begun to model jet and rocket noise within a single framework, much remains to be understood about their fundamental differences. For instance, BSN appears absent in rocket engines, and it is unclear whether multi-lobe radiation—common in afterburning jets—also occurs in rockets. Additionally, current scaling approaches such as Strouhal number scaling struggle to collapse data across regimes. Temperature, a major unaccounted factor in traditional scaling, likely plays a central role and should be included in future formulations.

With regards to modeling, challenges remain in characterizing multicore rocket sources and their radiation behavior. Further study and characterization of asymmetric rockets is needed to properly model any potential effects. Propagation modeling is also an area where significant progress could be made; the interplay between atmospheric absorption and nonlinear effects complicates propagation predictions, yet understanding this interplay is essential for accurate long-range noise propagation. The SATURN model offers a promising platform for exploring these effects and could be extended to incorporate more explicit, physics-based propagation treatments, which could include atmospheric ray-tracing and nonlinear propagation algorithms. SATURN could also be improved by further refining the model inputs through a larger aggregation of launch acoustic data. Additionally, the SATURN methodology could also be readily applied to aircraft jet noise with the development of modeling inputs for this application.

Appendix A

Summary of Other Notable Contributions

During the course of this dissertation's work, the author has been involved with several other research efforts and publications. Only first-authored publications were inserted as chapters in this dissertation document. This appendix summarizes other publications that the author made significant contributions to.

A.1 Saturn V Acoustics

- Gee, K. L., Mathews, L. T., Anderson, M. C., and Hart, G. W. (**2022**). "Saturn-V sound levels: A letter to the Redditor," *J. Acoust. Soc. Am.* **152**(2), pp. 1068-1073; https://doi.org/10.1121/10.0013216.

This paper reviews the acoustical characteristics of the Saturn V launch vehicle based on historical documents and was prepared for a JASA special issue on Education in Acoustics. The work was conducted in full collaboration with K. L. Gee, M. C. Anderson, and G. W. Hart, with all authors contributing equally to the paper. The author was involved in the historical research, data extraction, writing, and figure/multimedia creation for the paper, as well as the creation of numerous acoustics homework problems as part of the supplementary material.

A.2 Convective Mach Number Study

- Gee, K. L., Olaveson, T. W., and Mathews, L. T., (**2025a**). "Convective mach number and full-scale supersonic jet noise directivity," *AIAA J.* **63**(4), pp. 1393-1404; https://doi.org/10.2514/1.J064208.

This paper presents a comprehensive review on the convective Mach number used to describe the directivity of Mach wave radiation in supersonic jet noise. The work was conducted in full collaboration with K. L. Gee and T. W. Olaveson, with all three authors contributing equally to the literature review, data extraction and analysis, figure creation, and manuscript writing and revision.

A.3 Afterburning Lab-Scale Jet Rig Measurements

- Kumar, A., Meadows, J., Olaveson, T. W., Gee, K. L., Mathews, L. T., and Pratt, H. J. (**2025**). "Far-field noise measurements of a supersonic jet operating near afterburning conditions," *Aerospace Science and Technology* **157**, 109842; https://doi.org/10.1016/j.ast.2024.109842.

This paper details the first acoustical measurements of a laboratory-scale afterburning jet rig hosted at the Virginia Tech Advanced Propulsion and Power Laboratory. The author was heavily involved with the preparation, measurement, and data validation for this project. In particular, the author designed and oversaw the construction and operation of the intensity scanning apparatus and measurement instrumentation associated with this project. More publications from this project are forthcoming.

A.4 Starship-Super Heavy Acoustics

- Gee, K. L, Pulispher, N. L., Kellison, M. S., Mathews, L. T., Anderson, M. C., and Hart, G. W. (**2024**). "Starship super heavy acoustics: Far-field noise measurements during launch and the first-ever booster catch," *JASA Express Lett.* **4**, 113601; https://doi.org/10.1121/10.0034453.
- Gee, K. L., Pulsipher, N. L., Kellison, M. S., Hart, G. W., Mathews, L. T., and Anderson, M. C. (**2025b**). "Starship Super Heavy acoustics: Comparing launch noise from Flights 5 and 6," *JASA Express Lett.* **5**, 023602; https://doi.org/10.1121/10.0035925.

These two letters present the first published far-field acoustic measurements of the Starship–Super Heavy launch vehicle. The author contributed to both projects through participation in measurement planning, field data collection, and manuscript preparation, including the development of several figures.

Appendix B

SATURN Appendices

B.1 SATURN Model Archive

The SATURN model codes presented in Chapter 6 are available in a GitHub repository at https://github.com/logmath/saturn. These codes were developed for MATLAB.

B.2 Computing θ and r

Two important geometry parameters to compute for rocket noise prediction are the angle θ between the vehicle plume axis and the line from the source to the observer and r, the straight-line distance from the source to the observer. This can be calculated using the following method: let the rocket vehicle position (trajectory) at time t be $\boldsymbol{T}(t) = (\boldsymbol{x}'(t), \boldsymbol{y}'(t), \boldsymbol{z}'(t))$ and the observer position be $\boldsymbol{P} = (x, y, z)$. From this the unit velocity vector, $\widehat{\boldsymbol{V}}(t)$, of the rocket can be found as

$$\widehat{\boldsymbol{V}}(t) = \frac{\boldsymbol{V}(t)}{\|\boldsymbol{V}(t)\|} = \frac{\dot{\boldsymbol{T}}(t)}{\|\dot{\boldsymbol{T}}(t)\|}, \tag{B.1}$$

where $\boldsymbol{V}(t)$ is the velocity vector of the rocket, which may either be supplied with the trajectory or can be estimated by taking the time derivative of the rocket position vector, denoted by $\dot{\boldsymbol{T}}$. As the dominant source location changes based on frequency, the effective source location at a given frequency and time can be represented by

$$\boldsymbol{S}(t, \mathrm{Sr}) = \boldsymbol{T}(t) + s(\mathrm{Sr})\widehat{\boldsymbol{V}}(t), \tag{B.2}$$

where $s(Sr)$ is the frequency-dependent axial source location that can be estimated by Eq. (6.6).

From this, the vector between the observer location and the frequency-dependent source location at a given frequency is given by

$$\boldsymbol{R}(t, \mathrm{Sr}) = \boldsymbol{P} - \boldsymbol{S}(t, \mathrm{Sr}). \tag{B.3}$$

The magnitude of this vector, $r = \|\boldsymbol{R}\|$, is the straight-line propagation distance from the source to the observer. Finally, the angle $\theta(t, Sr)$ between the vehicle plume axis and the line from source to observer can be calculated as

$$\theta(t, Sr) = cos^{-1}\left(\frac{\boldsymbol{R}(t, \mathrm{Sr}) \cdot \boldsymbol{V}(t)}{\|\boldsymbol{R}(t, \mathrm{Sr})\|\|\boldsymbol{V}(t)\|}\right). \tag{B.4}$$

B.3 Source Location Angular Errors

As discussed in Section IIIC1, rocket noise is generated by a spatially distributed source region, with the dominant source location varying systematically with frequency. Accurately accounting for this frequency-dependent behavior is important for both source analysis and noise prediction.

To assess the consequences of assuming a fixed source location, the angular error between the true source angle and the angle computed under simplified assumptions was analyzed. The "true" source location in this analysis is taken as the modeled dominant source position from Eq. (6.6), which provides an empirical approximation of where the dominant acoustic energy originates at each frequency. Using this model, the actual elevation angle to the dominant source was computed for each combination of frequency and observer distance. Two fixed source

location assumptions were then tested: (1) that the source is located at the nozzle exit, and (2) that the source is located a constant distance of 18 effective diameters below the nozzle.

Figure A.1 shows the resulting angular error for each assumption, under the condition that the modeled dominant source appears at a 30° elevation angle for each observer distance. This setup represents a typical scenario near the region of peak launch noise. The analysis assumes flat terrain and a vertical launch profile.

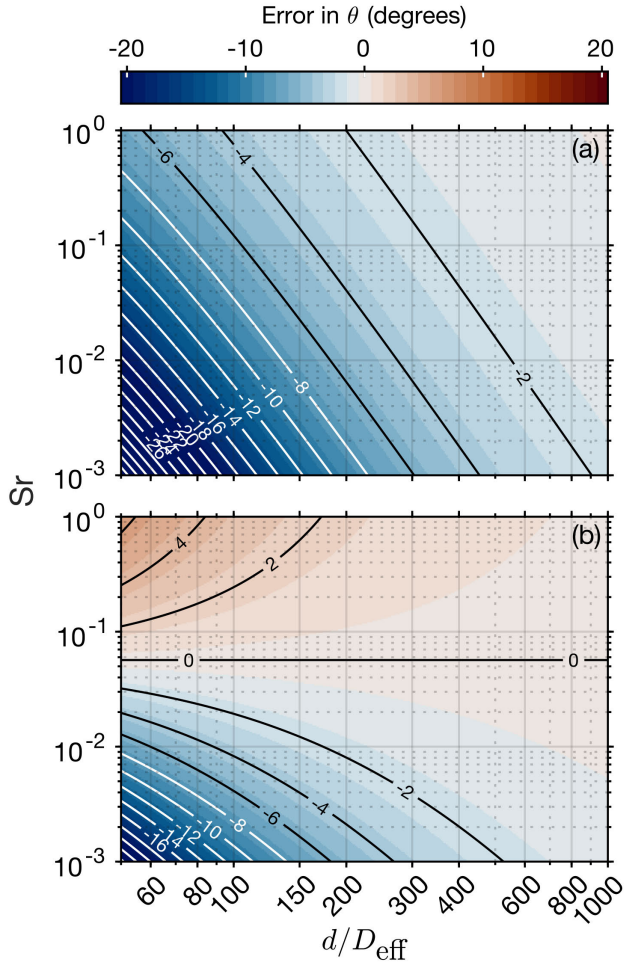

Figure A.1. Error in the computed plume angle when the source location is incorrectly assumed. The true source location varies with frequency, and the dominant, frequency-dependent source location is approximated by Eq. (6.6). (a) Error incurred when the source is assumed to be located at the nozzle exit. (b) Error incurred when the source is assumed to be fixed at 18 effective nozzle diameters downstream of the nozzle exit.

In Fig. A.1(a), assuming the source lies at the nozzle exit leads to substantial underestimation of the source angle, especially at low frequencies. Since rocket noise maximum spectra typically peak near a Strouhal number of ~0.01-0.02, this assumption results in angular errors at the peak frequency exceeding 5° except at distances beyond ~200 D_{eff}.

In Fig. A.1(b), assuming a fixed source location at 18 D_{eff} generally reduces the angular error. At Sr = 0.01-0.02, the error remains below 5° beyond ~70 D_{eff}. However, at large distances, the error associated with both assumptions diminishes and becomes negligible.

Overall, this analysis highlights the importance of accounting for frequency-dependent source location, particularly in the near field and at low frequencies, which can be generated substantially downstream. For observer distances greater than ~1000 D_{eff} effective nozzle diameters, the assumed source location has minimal impact on the estimated source angle.

Bibliography

Beranek, L. L., and Mellow, T. J. (**2012**). *Acoustics: Sound Fields and Transducers*, Academic Press, Amsterdam.

Chobotov, V., and Powell, A. (**1957**). "On the Prediction of Acoustic Environments from Rockets," Ramo-Wooldridge Corporation GM-TR-190.

Christian, M. A., Gee, K. L., Streeter, J. B., Wall, A. T., and Campbell, S. C. (**2023**). "Sound power and acoustic efficiency of an installed GE F404 jet engine," *JASA Express Lett.* **3**, 073601. https://doi.org/10.1121/10.0019866.

Bradley, K. A., James, M. M., Salton, A. R., and Boeker, E. R. (**2018**). "Commercial Space Operations Noise and Sonic Boom Modeling and Analysis," National Academies of Sciences, Engineering, and Medicine Transportation Research Board, Washington, DC.

Della Posta, G., Martelli, E., Stella, F., Barbagallo, D., Neri, A., Salvadore, F., and Bernardini, M. (**2023**). "High-fidelity simulations of the aeroacoustic environment of the VEGA launch vehicle at lift-off," *Computers & Fluids* **263**, 105945. https://doi.org/10.1016/j.compfluid.2023.105945

Durrant, J. T., Anderson, M. C., Bassett, M. S., Gee, K. L., Hart, G. W., Batelaan, R. H., Lawrence, D. C., and Hall, L. C. (**2023**). "Overview and spectral analysis of the Falcon-9 SARah-1 launch and reentry sonic boom," *Proc. Mtgs. Acoust.* **51**, 040006. https://doi.org/10.1121/2.0001767

Eldred, K. M. (**1971**). "Acoustic Loads Generated by the Propulsion System," NASA SP-8072.

Ffowcs-Williams, J. E., and Hawkings, D. L. (**1969**). "Sound Generation by Turbulence and Surfaces in Arbitrary Motion". *Philosophical Transactions of the Royal Society A:*

Mathematical, Physical and Engineering Sciences **264**(1151), 321-342. https://doi.org/10.1098/rsta.1969.0031.

Franken, P. A. (**1958**). "Review of information on jet noise," *Noise Control* **4**(3), 8–16. https://doi.org/10.1121/1.2369320.

Gee, K. L., Sparrow, V. W., James, M. M., Downing, J. M., Hobbs, C. M., Gabrielson, T. B, and Atchley, A. A. (**2008**). "The role of nonlinear effects in the propagation of noise from high-power jet aircraft," *J. Acoust. Soc. Am.* **123**(6), 4082–4093. https://doi.org/10.1121/1.2903871.

Gee, K. L., Downing, M. J., James, M. M., McKinley, R. C., McKinley, R. L., Neilsen, T. B., and Wall, A. T. (**2012**). "Nonlinear Evolution of Noise from a Military Jet Aircraft during Ground Run-up," *18th AIAA/CEAS Aeroacoustics Conference (33rd AIAA Aeroacoustics Conference)*, 4-6 June, Colorado Springs, CO, USA, AIAA Paper 2012-2258. https://doi.org/10.2514/6.2012-2258.

Gee, K. L., Miller, K. G., Reichman, B. O., and Wall, A. T. (**2018**). "Frequency-domain nonlinearity analysis of noise from a high-performance jet aircraft," *Proc. Mtgs. Acoust.* **34**, 045027. https://doi.org/10.1121/2.0000899.

Gee, K. L., Mathews, L. T., Anderson, M. C., and Hart, G. W. (**2022**). "Saturn-V sound levels: A letter to the Redditor," *J. Acoust. Soc. Am.* **152**(2), 1068-1073; https://doi.org/10.1121/10.0013216.

Gee, K. L., Hart, G. W., Cunningham, C. F., Anderson, M. C., Bassett, M. S., Mathews, L. T., Durrant, J. T., Moats, L. T., Coyle, W. L., Kellision, M. S., and Kuffskie, M. J. (**2023**). "Space Launch System acoustics: Far-field noise measurements of the Artemis-I launch," *JASA Express Lett.* **3**, 023601. https://doi.org/10.1121/10.0016878.

Gee, K. L., Pulsipher, N. L., Kellison, M. S., Mathews, L. T., Anderson, M. C., and Hart, G. W. (**2024**). "Starship super heavy acoustics: Far-field noise measurements during launch and the first-ever booster catch," *JASA Express Lett.* **4**, 113601. https://doi.org/10.1121/10.0034453

Gee, K. L., Olaveson, T. O., and Mathews, L. T., (**2025a**). "Convective mach number and full-scale supersonic jet noise directivity," *AIAA J.* **63**(4), 1393-1404; https://doi.org/10.2514/1.J064208.

Gee, K. L., Pulsipher, N. L., Kellison, M. S., Hart, G. W., Mathews, L. T., and Anderson, M. C. (**2025b**). "Starship Super Heavy acoustics: Comparing launch noise from Flights 5 and 6," *JASA Express Lett.* **5**, 023602. https://doi.org/10.1121/10.0035925

Harper-Bourne, M., and Fisher, M. J. (**1974**). "The Noise from Shock Waves in Supersonic Jets," *Proc. AGARD Conf.*, Conference Preprint 131.

Harris, R. E., Collins, E. M., Luke, E. A., and Sescu, A. (**2016**). "Coupled overset unstructured discontinuous Galerkin method for launch environment acoustics prediction," *AIAA J*. **54**, 1932–1952. https://doi.org/10.2514/1.J054563.

Haynes, J., and Kenny, R. J. (**2009**). "Modifications to the NASA SP-8072 Distributed Source Method II for Ares I Lift-off Environment Predictions," *15th AIAA/CEAS Aeroacoustics Conference (30th AIAA Aeroacoustics Conference)*, 11-13 May, Miami, FL, USA, AIAA Paper 2009-3160. https://doi.org/10.2514/6.2009-3160.

Hubbard, H. H., and Lassiter, L. W. (**1953**). "Experimental Studies of Jet Noise," J. Acoust. Soc. Am. **25**(3), pp. 381–384. https://doi.org/10.1121/1.1907051.

James, M. M., Salton, A. R., Gee, K. L., Nielsen, T. B., McInerny, S. A., and Kenny, R. J. (**2012**). "Modification of directivity curves for a rocket noise model," *Proc. Mtgs. Acoust.* **18**, 040008. https://doi.org/10.1121/1.4870986.

Kellison, M. S., Gee, K. L., Cunningham, C. F., Coyle, W. L., Moore, T. R., and Hart, G. W. (**2023**). "Community-based noise measurements of the Artemis-I mission," *Proc. Mtgs. Acoust.* **51**, 040004. https://doi.org/10.1121/2.0001786.

Kellison, M. S., Gee, K. L., Coyle, W. L., Anderson, M. C., Mathews, L. T., and Hart, G. W. (**2024**). "Aeroacoustical Analyses from the SpaceLaunch System Artemis-I Mission," *30th AIAA/CEAS Aeroacoustics Conference*, 4-7 June, Rome, Italy, AIAA Paper 2024-3033. https://doi.org/10.2514/6.2024-3033.

Kiris, C. C., Housman, J. A., Barad, M. F., Brehm, C., Sozer, E., and Moini-Yekta, S. (**2016**). "Computational framework for launch, ascent, and vehicle aerodynamics (LAVA)," *Aerosp. Sci. Technol.* **55**, 189–219. https://doi.org/10.1016/j.ast.2016.05.008.

Kumar, A., Meadows, J., Olaveson, T. W., Gee, K. L., Mathews, L. T., and Pratt, H. J. (**2025**). "Far-field noise measurements of a supersonic jet operating near afterburning conditions," *Aerosp. Sci. Technol.* **157**, 109842; https://doi.org/10.1016/j.ast.2024.109842.

Liever, P. A., West, J. S., and Harris, R. E. (**2017**). "Validation of high-fidelity CFD/CAA framework for launch vehicle acoustic environment simulation against scale model test data," in JANNAF Conference, NASA Report M17-5678, Washington, DC.

Lighthill, M. J. (**1952**). "On sound generated aerodynamically. I. General theory". *Proceedings of the Royal Society A.* **211**(1107), 564–587; https://doi.org/10.1098/rspa.1952.0060.

Lighthill, M. J. (**1954**). "On sound generated aerodynamically. II. Turbulence as a source of sound". *Proceedings of the Royal Society A*. **222**(1148), 1–32; https://doi.org/10.1098/rspa.1954.0049.

Lilley, G. M. (**1974**). "On the Noise from Jets." *Proc. AGARD Conf.,* Conference Preprint 131.

Lubert, C. P., Gee, K. L., and Tsutsumi, S. (**2022**). "Supersonic jet noise from launch vehicles: 50 years since NASA SP-8072," *J. Acoust. Soc. Am.* **151**(2), 752-791. https://doi.org/10.1121/10.0009160

Manhart, J. K., Ailman, C. M., Lane, S. R., and Marsh, A. H. (**1966**). "An Acoustical Study of the Kiwi B Nuclear Rocket," NASA CR-370.

Mathews, L. T., Anderson, M. C., Gardner, C. D., McLaughlin, B. W., Hinds, B. M., McCullah-Boozer, M. R., Hall, L. K., and Gee, K. L. (**2023**). "An overview of acoustical measurements made of the Atlas V JPSS-2 rocket launch," *Proc. Mtgs. Acoust*. **51**, 040003. https://doi.org/10.1121/2.0001768

Mathews, L. T., and Gee, K. L. (**2025**). "Methods for predicting overall sound power and maximum overall sound pressure levels from heated supersonic jets, including rockets," *J. Acoust. Soc. Am.* **158**(1), 371-379. https://doi.org/10.1121/10.0037192.

McDowell, J. (**2025**). "GCAT Orbital Launch Log," retrieved 02 June 2025, https://planet4589.org/space/gcat/data/derived/launchlog.html.

Miller, K. G., and Gee, K. L. (**2018**). "Model-scale jet noise analysis with a single-point,frequency-domain nonlinearity indicator," *J. Acoust. Soc. Am.* **143**(6), 3479–3492. https://doi.org/10.1121/1.5041741.

Nagamatsu, H. T., Sheer, R. E., and Horvay, G. (**1969**). "Supersonic Jet Noise Theory and Experiments," in Basic Aerodynamic Noise Research.

Potter, R. C., and Crocker, M. J. (**1966**). "Acoustic Prediction Methods for Rocket Engines, Including the Effects of Clustered Engines and Deflected Exhaust Flow," NASA CR-566.

Powell, A. (**1953**). "On the Mechanism of Choked Jet Noise," *Proc. Phys. Soc. B* **66**(12), 1039-1057. https://doi.org/10.1088/0370-1301/66/12/306.

Plotkin, K. J. (**2010**). "A model for the prediction of community noise from launch vehicles," *J. Acoust. Soc. Am.* **127**(3 Supplement), 1773.

Plotkin, K. J., Sutherland, L. C., and Moudou, M. (**2004**). "Prediction of rocket noise footprints during boost phase," *3rd AIAA/CEAS Aeroacoustics Conference*, 12–14 May, Atlanta, GA, AIAA Paper 1997–1660.

Reichman, B., Wall, A. T., Gee, K. L., Neilsen, T. B., Downing, M. J., James, M. M., and McKinley, R. L. (**2016**). "Modeling Far-field Acoustical Nonlinearity from F-35 Aircraft during Ground Run-up," *AIAA SciTech Forum*, 4-8 Jan, San Diego, CA, USA, AIAA Paper 2016-1888. https://doi.org/10.2514/6.2016-1888.

Ribner, H. S. (**1954**). "Shock-Turbulence Interaction and the Generation of Noise," NACA TN-3255.

Sutherland, L. C. (**1993**). "Progress and problems in rocket noise prediction for ground facilities," *15th AIAA Aeroacoustics Conference*, 25–27 October, Long Beach, CA, USA, AIAA Paper 1993–4383. https://doi.org/10.2514/6.1993-4383.

Tam, C. K. W. (**1975**). "Supersonic Jet Noise Generated by Large Scale Disturbances," *J. Sound Vib.* **38**(1), 51-79. https://doi.org/10.1016/S0022-460X(75)80020-4.

Tam, C. K. W., and Chen, P. (**1994**). "Turbulent Mixing Noise from Supersonic Jets," *AIAA J.* **32**(9), 1774-1780. https://doi.org/10.2514/3.12173.

Tam, C. K. W. (**1995**). "Supersonic Jet Noise," *Annu. Rev. Fluid Mech.* **27**, 17-43. https://doi.org/10.1146/annurev.fl.27.010195.000313.

Tam, C. K. W., Golebiowski, M., and Seiner, J. M. (**1996**). "On the Two Components of Turbulent Mixing Noise from Supersonic Jets," *2nd AIAA/CEAS Aeroacoustics Conference*, May 6-8, State College, PA, USA, AIAA Paper 1996-1716. https://doi.org/10.2514/6.1996-1716.

Tedrick, R. N. (**1964**). "Acoustical Measurements of Static Tests of Clustered and Single-Nozzled Rocket Engines," *J. Acoust. Soc. Am.* **36**(11), 2027-2032. https://doi.org/10.1121/1.1919318.

Tsutsumi, S., Ishii, T., Ui, K., Tokudome, S., and Wada, K. (**2015**). "Assessing prediction and reduction technique of lift-off acoustics using Epsilon flight data," *AIAA SciTech Fourm/53rd AIAA Aerospace Sciences Meeting*, 6-9 January, Kissimmee, FL, AIAA Paper 2015-1007. https://doi.org/10.2514/6.2015-1007

Tsutsumi, S., Sarae, W., and Terashima, K. (**2019**). "Effect of rocket engine clustering on acoustic level of H3 launch vehicle at lift-off," *32nd International Symposium on Space Technology and Science*, Japan Society for Aeronautical and Space Sciences (JSASS), p. 2019-g-12.

Wall, A. T., Gee, K. L., Morris, P. J., Colonius, T., and Lowe, K. T. (**2021**). "Introduction to the special issue on supersonic jet noise," *J. Acoust. Soc. Am*. **151**(2), 806-816; https://doi.org/10.1121/10.0009321.

Wilhold, G. A., Guest, S. H., and Jones, J. H. (**1963**). "A Technique for Predicting Far-field Acoustic Environments Due to a Moving Rocket Sound Source," NASA TN-D-1832.